Masterarbeit/Master's Thesis

Titel der Materarbeit/ Title of the Master's Thesis

The Quasi-satellite problem - Semi-analytical and numerical approaches

verfasst von/ submitted by

Andreas Felsenstein BSc

Angestrebter akademischer Grad/ in partial fulfilment of the requirement for the degree of

Master of Science (MSc)

Wien 2018/ Vienna 2018

Studienkennzahl lt. Studienblatt/ degree programme code as it appears on the student record sheet:	A 066 861
Studienrichtung lt. Studienblatt / degree programme as it appears on the student record sheet:	Astronomy
Betreut von/ Supervisor:	ao. Univ. -Prof. i.R. tit. Univ.-Prof Dr. Rudolf Dvorak

Abstract

The 1:1-resonance in the mean motion of two celestial bodies is one of the most well-known problems of celestial mechanics. 1:1-resonance occurs when two bodies orbit a central massive body at the same orbital distance. Every 1:1-resonance is characterised by a resonance angle, which is a property composed from the orbital elements of the two bodies. The quasi-satellite problem is a special case of 1:1-resonance in the Elliptical Restricted Three-body problem (ER3BP). Its resonance angle $\Delta\lambda$ oscillates around a value of $0°$. The most important goal of this thesis is a precise description of the phase space structure for quasi-satellites in the ER3BP and an analysis of their stability in this configuration.

A semi-analytical model was developed from Hamiltonian formalism, which allowed a derivation of the basic phase space structure. This framework confirmed a fixed point in a configuration with anti-aligned longitudes of perihelion ($\Delta\varpi = 180°$). Contrary to the Trojan fixed points ($\Delta\lambda = 60, 300°$), the region around this fixed point became more stable with increasing planetary eccentricity and occupied a large area of the phase space. This was confirmed with numerical integration, which demonstrated that quasi-satellites are stable for extended periods of time, with secular periods lasting 2500-5000 years for Jupiter-sized planets. It was also shown that the configuration remained stable when the initial semi-major axis of the asteroid was perturbed. It was demonstrated that the semi-analytical and numerical results agreed with each other in the coplanar case. The non-coplanar case was also numerically investigated. It was shown that chaotic effects began to play a more significant role, and that the resonance still held for inclinations up to $100°$. A stable retrograde resonance with a different resonance angle also was produced for other initial conditions. General relativistic effects were also applied to the results, which only created a significant difference for bodies with the highest eccentricities. The problem was also described using Lyapunov Characteristic Exponents (LCE). The LCEs were determined with a method that allows computation independent of the integration algorithm.

There are currently 13 quasi-satellites discovered in the solar system, that are stable for limited periods of time. There are some extrasolar planet systems which could contain quasi-satellites. This is especially interesting for multi-planet systems with high eccentricities. The two-planet systems HD 183263 and HD 73526 were chosen to numerically test the stability of quasi-satellites. In both cases, objects that were in 1:1-resonance with the inner planet had longer resonance lifetimes than those in 1:1-resonance with the outer planet. In the case of HD 183263, the resonance lifetimes often exceeded 100 kyr.

Contents

1 Introduction

In 1667 Sir Isaac Newton published his theory of gravity in the "Principia Mathematica", which completely solves the problem of two massive bodies interacting only with gravitation. It is referred as the two-body-problem. The resulting orbits are ellipses that can, for example, be described with the aid of the Keplerian orbital elements. How to describe the motion of more than two bodies is a question that has been heavily investigated by scientists. The equations of motion for three bodies are:

$$\ddot{x}_i = -G \sum_{j=1, i\neq j}^{3} m_j \frac{x_i - x_j}{|x_i - x_j|^3} \tag{1}$$

where x_i are the spatial coordinates of the bodies, m_i are their masses, and G is the gravitational constant.

More sophisticated methods of describing dynamic systems were developed by Joseph Louis Lagrange in 1788 and William Rowan Hamilton in 1833. This thesis works with the Hamiltonian function, which consists of one part representing the system's kinetic energy, and one part representing the system's potential energy. For the three-body problem, it is defined as:

$$H = \frac{1}{2}\sum_{i=1}^{3} m_i|\dot{x}|^2 - G\sum_{i=1}^{3}\sum_{j=1,i\neq j}^{3}\frac{m_i m_j}{|x_i - x_j|} \qquad (2)$$

It has been known for centuries that this general problem has no analytical solution. For this reason, a reduced version was introduced by Leonhard Euler as early as 1767. This version consists of a massive body in the center, a less massive (typically less than 5% of the mass of the primary) body in orbit around it and a massless body, also in orbit around the primary. Massless bodies do not exist in real systems, but the mass of most asteroids is so small relative to the mass of a planet, that it can be neglected. The approximation is applied to simplify the equations of motion.

This reduced version is known as the Restricted Three-Body Problem (R3BP). In terms of real world applications, this problem can be applied to the interactions between a central star, a massive planet and an asteroid. The planar circular version of the problem sets all eccentricities to 0, and places all orbits in the same orbital plane. This causes the distance between primary and secondary body, as well as the orbital velocity, to remain constant over time. The positions of the primary and secondary body are fixed when a co-rotating coordinate system is used.

In this coordinate system, it is possible to formulate an effective potential, that can be used to describe the orbital behavior of the third massless body. The geometry of the potential is illustrated in Figure 1. Equilibrium points with non-changing orbits can be identified by locating extreme points in this potential. These points are known as the Lagrangian points. Point L_1 lies slightly inside of the location of the planet in the rotating frame, whereas L_2 lies slightly outside of this location. The point L_3 lies exactly at the opposite side of the planet as seen from the star. Finally, points L_4 and L_5 lie exactly 60° ahead and behind the planet with respect to the star. An object exactly at one of the Lagrangian points will not be perturbed by the planet and is able to move on its orbit around the star with the same orbital period as the planet. An object with this behavior is called a *coorbital* object.

It should be noted that the Lagrangian points L_1 - L_3 are hyperbolic points, where even a small derivation can perturb the point from the equilibrium and lead to an unstable orbit, whereas L_4 and L_5 are true extreme points where orbits around the equilibrium point are still stable. These are called *Trojan* points, and asteroids close to them are *Trojan* asteroids. Other forms of coorbital motion associated with the Lagrangian points L_4 and L_5 include *tadpole* orbits and *horseshoe* orbits. Bodies on tadpole orbits move in a widely elongated trajectory around one of the points. Bodies on horseshoe orbits have a trajectory around both L_4 and L_5.

Coorbital objects are in a 1:1 mean-motion resonance. Mean-motion resonances generally occur when orbital periods of different objects are in a ratio that can be written with two integer numbers. Every mean motion resonance is characterised by a

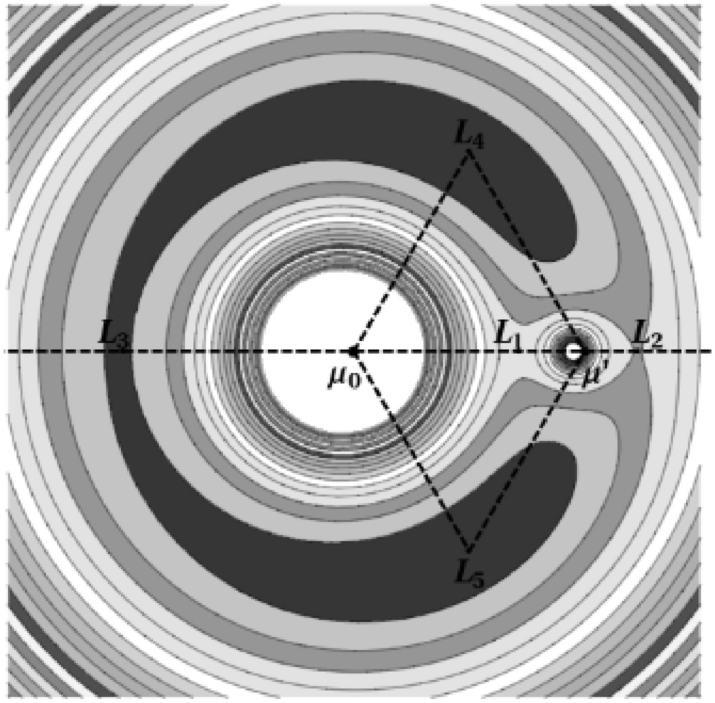

Figure 1: Spatial geometry of the Circular R3BP in the co-rotating coordinate system. The primary body is at position μ_0, the secondary is at position μ'. Lines of constant effective potential are outlined as contours. Figure is taken from Dvorak, Lhotka, and Zhou (2012).

resonance angle, which is composed of orbital elements of the two participating bodies. In the case of coorbital dynamics, the period ratio is 1. It is the most simple of the mean motion resonances. The resonance angle of the prograde coorbital resonance is:

$$\Delta\lambda = \lambda_2 - \lambda_1 \tag{3}$$

where λ_i are the mean longitudes of the bodies defined as:

$$\lambda_i = \Omega_i + \omega_i + M_i \tag{4}$$

with the longitudes of the ascending nodes Ω_i, the arguments of perihelion ω_i and the mean anomalies M_i.

For objects in the coorbital mean-motion resonance, the resonance angle oscillates over time around a fixed value. This value is 60° and 300° for objects around the Lagrangian points L_4 and L_5, respectively. For horseshoe orbits, where the asteroid oscillates around both Lagrangian points, $\Delta\lambda$ oscillates with high amplitude centered around 180°, but never reaches 0°.

The model with the rotating coordinate system becomes inapplicable for an elliptic planetary orbit, as the distance between the planet and the star is no longer constant. An analytical description is difficult, because it is not easy to express the Hamiltonian function in terms of the classical orbital elements or their modified canonical variants. Nonetheless, several approximations have been made. In (Laskar and Robutel, 1995), the Hamiltonian function is expressed in terms of high orders of the semi-major axis ratio. This property is 1 for coorbital objects. For this reason, there is no convergence and the model can not be applied. A version for coorbital resonance was introduced by Lhotka and Celletti (2015), but this version only works for low values of eccentricity. For a detailed derivation of the mentioned formulas and a discussion of related problems, see Dvorak and Freistetter (2005).

This thesis deals with a special configuration of coorbital dynamics that is called the *quasi-satellite* or *retrograde satellite* configuration. Quasi-satellites have a resonance angle $\Delta\lambda$ of $0°$, which is a value that is not possible when only circular planet and asteroid orbits are considered. The configuration was first theoretically discussed by Jackson (1913). Henon (1969) had the first computational results on the topic. The term "quasi-satellite" was introduced by Mikkola and Innanen (1997) when describing the behavior of a solar system object. This name has its root in the apparent motion that a small body like this exhibits from the perspective of a massive planet. It seems to travel around the planet like a satellite with retrograde inclination but it is not actually gravitationally bound to it.

Theoretical studies on the stability of quasi-satellites were conducted in subsequent years by Namouni, Christou, and Murray (1999)), Wiegert, Innanen, and Mikkola (2000), and Morais and Namouni (2016). Several objects on temporary quasi-satellite orbits have been found in the solar system. The possibility of two extrasolar planets with this configuration was also discussed by Giuppone et al. (2010), Funk et al. (2011), and Funk, Dvorak, and Schwarz (2017). In this case, the two participating bodies exhibit a periodic exchange in eccentricity. In the R3BP, this is not possible, since the orbital elements of the massive secondary are constant.

The main goal of this work is to link the various applications of the problem and put them into context with each other. The focus lies on quasi-satellites in the R3BP, massless bodies in resonance with a massive planet around a single star. Most stability studies for this configuration have focused on either circular planetary orbits or two-planet configurations. Here, planetary eccentricities up to 0.99 are considered as well as non-coplanar configurations. The structure of the resulting phase space is discussed in as much detail and as comprehensively as possible.

This thesis has the following structure: In Section 2, the analytic and numerical solutions of the quasi-satellite problem are described and discussed. Section 2.1 builds a semi-analytical model for coorbital resonance from a Hamiltonian framework and discusses the structure of the resulting phase space. In Section 2.2, the same problem is approached via numerical integration, where the structure of the phase space is again explored. Section 2.2.1 deals with the coplanar case of quasi-satellite motion, and Section 2.2.2 compares the results with the semi-analytical values. Section 2.2.3 explores non-coplanar configurations, Section 2.2.4 discusses the influence of relativistic effects, and Section 2.2.5 describes the objects' behavior with the help of Lyapunov

Characteristic Exponents. Section 3 applies the results of the preceding chapters to existing planetary systems. Section 3.1. gives an overview of quasi-satellites and other coorbital objects in our own solar system, and section 3.2 briefly discusses the capture of coorbital asteroids. Sections 3.3 and 3.4 deal with the possibility of quasi-satellite asteroids in extrasolar planet systems. Section 3.3 introduces the currently known sample of systems, and Section 3.4 performs a stability analysis for quasi-satellites in the two multi-planet systems HD 183263 and HD73526. The results of Sections 2 and 3 are summarized in Section 4, and areas of future research are discussed. The appendix contains a description of the code that was developed for Section 2.2.5

2 Quasi-satellites in the Elliptical Restricted Three-Body Problem

2.1 Description of a semi-analytical model for coorbital resonance

The coorbital problem is considered in a framework of a three-body problem, as outlined by Giuppone et al. (2010) and Laskar and Robutel (1995). The Hamiltonian function (Equation 2) can be split up into a so-called direct part, which is responsible for the interaction between the central body and the less massive bodies, and an indirect part, which is responsible for the interaction between the less massive bodies. This approach dates back to the mid-19th Century with Delaunay (1861) and was first successfully implemented for the coorbital problem by Schubart (1964) for circular planetary orbits.

$$H = H_0 + H_1 \tag{5}$$

The direct part H_0 is the sum of the two-body Hamiltonians of the two participating small bodies. They result in Kepler ellipses. It can be written very compactly in terms of the orbital elements. In the case examined here, the two bodies are one planet and one asteroid. Henceforth, orbital elements and other properties of the planet will be denoted with a p-subscript, properties of the asteroid with an a-subscript. The gravitation constant is designated κ to avoid confusion with the later introduced canonical element G_i. The two-body Hamiltonian of the system is dependent on the masses m_i and the semi-major axis a_i:

$$H_0 = -\frac{\kappa m_p m_{star}}{2a_p} - \frac{\kappa m_a m_{star}}{2a_a} \tag{6}$$

The indirect part of the Hamiltonian represents the planet-asteroid interaction, which can be written in terms of the cartesian barycentric coordinates of the planet and the asteroid. Whether heliocentric or barycentric coordinates are taken for the position is unimportant, since only their difference factors into the equation.

$$H_1 = -\frac{\kappa m_p m_a}{\|\vec{x}_p - \vec{x}_a\|} + \frac{m_p m_a \vec{v}_{p,bar} \cdot \vec{v}_{a,bar}}{m_{star}} \tag{7}$$

H_0 is constant and only H_1 changes over time for a solution of the coorbital resonance with constant orbital elements. A solution like this is also called a *zero-amplitude solution* or a *fixed point* in the phase space.

To simplify the problem, first only the two-dimensional case was calculated. The z_i-coordinates of position and velocity are 0. If the orbital elements are considered, the values of i_i and Ω_i are 0°. This reduces the number of dimensions by four. Assuming a stellar mass of 1 it permits the use of a set of resonant canonical variables of the general three-body problem, defined in the following way (first introduced by Poincaré (1902), see also Giuppone et al. (2010)):

$$\Delta\lambda = \lambda_a - \lambda_p \tag{8}$$

$$\Delta\varpi = \varpi_a - \varpi_p \tag{9}$$

$$q = \varpi_p + \varpi_a \tag{10}$$

$$Q = \lambda_p + \lambda_a - q \tag{11}$$

$$I_1 = 0.5 \cdot (L_a - L_p) \tag{12}$$

$$I_2 = \frac{1}{2} \cdot (G_a - G_p - L_a + L_p) \tag{13}$$

$$J_1 = \frac{1}{2} \cdot ((G_a + G_p) \tag{14}$$

$$J_2 = \frac{1}{2} \cdot ((L_a + L_p) \tag{15}$$

with L_i and G_i respectively defined as:

$$L_i = m_i \sqrt{\kappa a_i} \tag{16}$$

$$G_i = L_i \sqrt{1 - e_i^2} \tag{17}$$

$\Delta\lambda$ is the resonance angle of the 1:1-resonance introduced earlier. The usual orbital elements can be easily transformed into these variables. The Hamiltonian equations of motion associated with them are:

$$\frac{dI_1}{dt} = \frac{\partial H_1}{\partial \Delta\lambda} \tag{18}$$

$$\frac{dI_2}{dt} = \frac{\partial H_1}{\partial \Delta\varpi} \tag{19}$$

$$\frac{dJ_1}{dt} = \frac{\partial H_1}{\partial \Delta q} \tag{20}$$

$$\frac{dJ_2}{dt} = \frac{\partial H_1}{\partial Q} \tag{21}$$

$$\frac{d\Delta\lambda}{dt} = -\frac{\partial H_1}{\partial I_1} \tag{22}$$

$$\frac{d\Delta\varpi}{dt} = -\frac{\partial H_1}{\partial I_2} \tag{23}$$

$$\frac{dq}{dt} = -\frac{\partial H_1}{\partial J_1} \tag{24}$$

$$\frac{dQ}{dt} = -\frac{\partial H_1}{\partial J_2} \tag{25}$$

A numerical value for the gravitational constant κ is required to correctly represent the relation between the potential and the kinetic energy. The preferred units are Astronomical Units (AU) for space, solar masses ($M_\odot$) for mass and days (d) for time. The gravitation constant in SI units is

$$G = 6.6741 \cdot 10^{-11} \frac{m^3}{kg \cdot s^2} \tag{26}$$

There are $1.496 \cdot 10^{11}$ meters in 1 Astronomical Unit, $1.989 \cdot 10^{30}$ kilograms in 1 solar mass and 86400 seconds in 1 day. Evaluating the gravitational constant with these values gives:

$$\kappa = 6.6741 \cdot 10^{-11} \frac{AU^3 \cdot m^3 \cdot 1.989 \cdot 10^{30} kg \cdot (86400\, s)^2}{(1.496 \cdot 10^{11}\, m)^3\, kg \cdot M_\odot \cdot s^2 \cdot d^2} = 0.0002959122 \frac{AU^3}{M_\odot \cdot d^2} \tag{27}$$

The Hamiltonians H_0 and H_1 can be calculated for a given set of initial conditions written in terms of orbital elements (a,e, ω, M for both bodies). The transformation from the orbital elements to the cartesian coordinates required in equation 7 is done via the usual way (e.g. Murray and Dermott, 1999).

An approximation of first order averaging is made to investigate the topology of H_1 in the phase space. The Mean Anomaly values are varied for both bodies between 0 and 360°, and the resonance angle $\Delta\lambda$ is kept constant. Other orbital elements are not changed. All values for H_1 calculated for one set of initial conditions can be integrated numerically over all values of M. An average value for H_1, that does not depend on

M, is found. This value can be used to describe the structure of the phase space and to find resonant initial conditions.

$$H_{Avg} = \int_0^{2\pi} H_1 \left(a_p, e_p, i_p, \Omega_p, \omega_p, a_a, e_a, i_a, \Omega_a, \omega_a\right) dM \tag{28}$$

The integration over the anomalies corresponds to an integration over Q from the resonant canonical variables. This technique was used in slightly different variations by Nesvorný et al. (2002), Giuppone et al. (2010), Sidorenko et al. (2014) and Batygin and Morbidelli (2017). In this work, the integration is done numerically via a simple Simpson integration with a sufficiently small step size. Between two anomalies A and B, the formula is:

$$\int_A^B H_1 dM = \frac{B-A}{6} \cdot \left(H_1(A) + H_1\left(\frac{A+B}{2}\right) + H_1(B)\right) \tag{29}$$

Without loss of generality, the value of a_p can be set to 1 and ω_p can be set to 0°. This reduces the number of variables to 5: e_p, a_a e_a, ω_a, and $\Delta\lambda$ in the orbital elements, or I_1, I_2, J_1, $\Delta\varpi$, and $\Delta\lambda$ in the canonical variables. The Hamiltonian function is evaluated with respect to the orbital elements in the next sections. $\Delta\varpi$ can generally be interchanged with ω_a, since $\omega_p = 0°$. The five variables lead to a computationally manageable phase space.

The elimination of the planets' orbital elements is formally done via canonical transformations as shown by Sidorenko et al. (2014), that reduce the system from a general 3BP to the R3BP. The mass of the asteroid is eliminated in the variables and the Hamiltonian equations are:

$$\frac{dL_a}{dt} = \frac{\partial H_1}{\partial \Delta\lambda} \tag{30}$$

$$\frac{d\Gamma_a}{dt} = \frac{\partial H_1}{\partial \omega_a} \tag{31}$$

$$\frac{d\Delta\lambda}{dt} = -\frac{\partial H_1}{\partial L_a} \tag{32}$$

$$\frac{d\omega_a}{dt} = -\frac{\partial H_1}{\partial \Gamma_a} \tag{33}$$

where:

$$\Gamma_i = G_i - L_i + 1 \tag{34}$$

At this point it should be stressed that the configuration is in principal symmetric with respect to both eccentricities. If the values of e_p and e_a are exchanged, the same value for the Hamiltonian emerges. However, it still makes sense to treat both parameters differently from one another, as e_p does by definition not change with time in the R3BP, and the phase space is studied at a fixed value of it. e_a can have a complex evolution, and the phase space structure with respect to the variables a_a, $\Delta\varpi$, and $\Delta\lambda$ becomes more important. Orbital paths of the asteroid can be taken along paths of equal H_{avg} in the phase space of the four variables.

The canonical variable $\Delta\lambda$ is the resonance angle of the coorbital resonance, oscillating around $0°$ for quasi-satellites. It needs to be investigated for which parameter combinations H_{avg} has an extreme point at $\Delta\lambda = 0°$ to find out where orbits with this resonance angle are possible. The corresponding canonical variable I_1 was set to 0, so that a_a is 1, which corresponds to the center of the 1-to-1-resonance. The planetary mass was set to 0.001, which is a value that corresponds to a Jupiter-sized planet.

Figure 2 depicts the profile of H_{avg} for $e_p = e_a = 0$, depending on $\Delta\lambda$. ω_a becomes undefined in this configuration. H_{avg} corresponds to the effective potential in the circular R3BP. The familiar Trojan Lagrangian points L_4 and L_5 at $\Delta\lambda = 60°, 300°$ appear, as well as the hyperbolic point L_3 at $\Delta\lambda = 180°$. The potential energy approaches infinity at $\Delta\lambda = 0°$, as the planet and asteroid orbit are equal . As already stated in the introduction, quasi-satellites are not possible in this configuration. In reality, a collision would occur at such a point.

Collision can generally occur for all intersecting orbits. In two dimensions, non-identical orbits with the same semi-major axis always have two points where they intersect. Each of these points corresponds to a certain value of $\Delta\lambda$, where the two objects will be at the intersection point at the same time.

The location of the collision can be calculated using the Kepler equations: The heliocentric distances of the two bodies need to be equal for a collision. The position angle as seen from the sun also needs to be equal. The angle is expressed with the true longitude, in this case written with the sum of the perihelion longitude ϖ and the true anomaly ν. With $\varpi_p = 0°$, these two conditions can be written as:

$$\frac{1-e_p^2}{1+e_p\cos\nu_p} = \frac{1-e_a^2}{1+e_a\cos\nu_a} \tag{35}$$

$$\nu_p = \varpi_a + \nu_a \tag{36}$$

These conditions yield an equation for ν_a:

$$e_a^2 - e_p^2 = \left(\left(1-e_a^2\right)e_p\cos\varpi_a - \left(1-e_p^2\right)e_a\right)\cos\nu_a - \left(1-e_a^2\right)e_p\sin\varpi_a\sin\nu_a \tag{37}$$

This can be transformed into a quadratic equation for $\cos\nu_a$ that can be easily solved. The two solutions for the True Anomalies can be transformed into Eccentric and Mean Anomalies with the following well-known formulas:

$$\cos E = \frac{\cos\nu + e}{1+e\cos\nu} \tag{38}$$

$$M = E - e\sin E \tag{39}$$

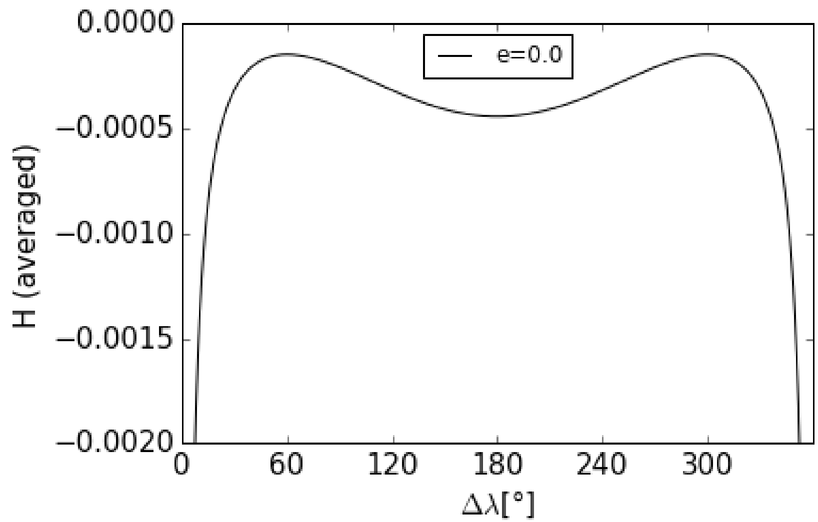

Figure 2: Averaged Hamiltonian function H_{avg} for $e_p = e_a = 0$, dependent on $\Delta\lambda$

Two values of M_p and M_a are found, which can be used to calculate the value of $\Delta\lambda$ where a collision occurs.

When the asteroid assumes eccentricity values different from 0, the position of the maxima and minima of H_{avg} changes. In Figure 3, the change of the Hamiltonian is shown for different e_a. There is a maximum at $\Delta\lambda = 0°$. The maxima of the Trojan points move towards 180° and almost vanish at higher eccentricities. The sharp collision minima also move inward. The minima do not stretch to infinity as the do for $e_a = 0$, because the collision orbit (represented by the dashed lines in Figures 3-6) is not fully reached, and the potential energy is finite. This is due to the finite step size in the numerical integration and the imperfect resolution in $\Delta\lambda$. The numerical value depends on the angle under which the two orbits intersect. The bodies spend more time in close proximity and the potential energy has a higher impact, if this angle is small. The interaction time is shorter, and the potential does not reach as deep, if the angle is close to 90°. The orbital speed during the close encounter also plays a role. It increases at perihelion, which results in a shorter interaction time. At aphelion, the objects are slower and have more time to interact.

For higher planetary eccentricities ($e_p > 0$) the principal profile of H_{avg}, depending on $\Delta\lambda$, remains the same. One additional variable ($\Delta\varpi$) needs to be taken into consideration. Orbits with identical elements can occur for the aligned case ($\Delta\varpi = 0°$, Figure 4), if the eccentricities are equal. If the sequence of the minima is compared with Figure 3, it can be observed that when the asteroid's eccentricity and the planet's eccentricity are close to one another, the collisional minimum nears $\Delta\lambda = 0°$, and its numerical value decreases.

The maximum at $\Delta\lambda = 0°$ is always present for the anti-aligned case ($\Delta\varpi = 180°$,

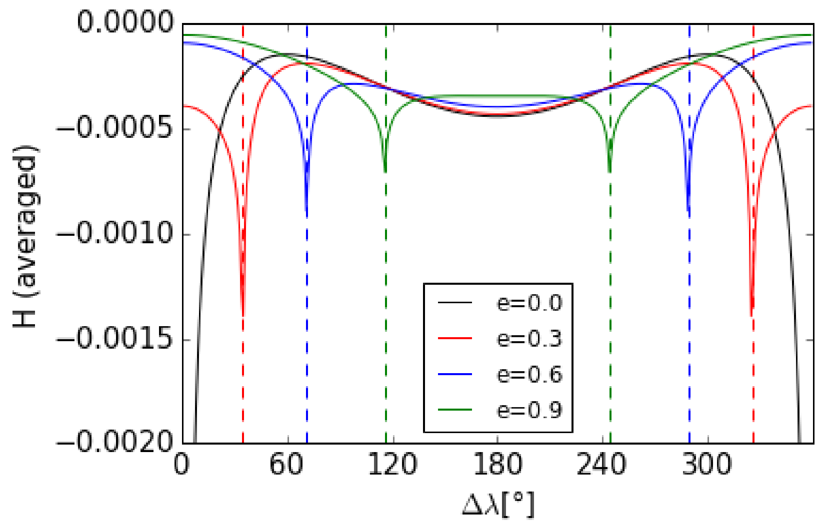

Figure 3: Averaged Hamiltonian function H_{avg} for $e_p = 0$ and different e_a, dependent on $\Delta\lambda$. Dashed lines represent the collision orbits for the respective eccentricity.

Figure	e_p	a_a[AU]	e_a	$\Delta\varpi[°]$	$\Delta\lambda[°]$
2	0	1	0	-	0,1,...,360
3	0	1	0,0.3,0.6 0.9	-	0,1,...,360
4	0.6	1	0,0.3,0.6,0.9	0	0,1,...,360
5	0.6	1	0,0.3,0.6,0.9	90	0,1,...,360
6	0.6	1	0,0.3,0.6,0.9	180	0,1,...,360

Table 1: Orbital parameters for the H_{avg} graphs in Figures 2-6

Figure 6), as there can be no extremely close approaches in this scenario. The angle for collisional orbits is high for other $\Delta\lambda$, and the approach is close to perihelion, so the absolute numerical value of the minimum is small. The distance of the minimum from $\Delta\lambda = 0°$ increases when the eccentricity of the asteroid increases.

The curve becomes asymmetrical for other values pf $\Delta\varpi$, and the maximum moves away from $\Delta\lambda = 0°$. The Trojan points generally become less pronounced with higher planetary eccentricity and become unstable when the collision minimum approaches $\Delta\lambda = 60°$ around $e_p = 0.6$. The different orbits for which H_{avg} was evaluated in Figures 2-6 are summarized in Table 1.

One example of an orbit with a deep minimum of $H_{avg}$is shown in Figure 7. One orbit with a shallow minimum is shown in Figure 8. Figure 7 shows the $e_p = 0.6$, $e_a = 0.9$, and $\Delta\varpi = 0°$ case (green line in Figure 4). Here the orbits cross in a relatively small angle close to aphelion where the orbital velocity is small. The portion of the orbits where the bodies are closer than 0.1 AU is marked in red. It accounts for approximately 8% of their orbital period. This is a comparatively long interaction time that results in a very deep minimum of H_{avg}.

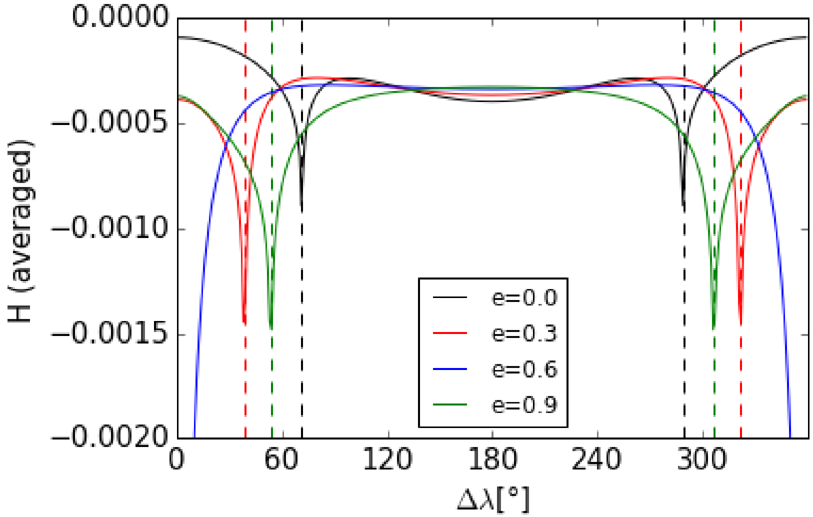

Figure 4: Averaged Hamiltonian function H_{avg} for $e_p = 0.6$ and different e_a with $\Delta\varpi = 0°$, dependent on $\Delta\lambda$. Dashed lines represent the collision orbits for the respective eccentricity.

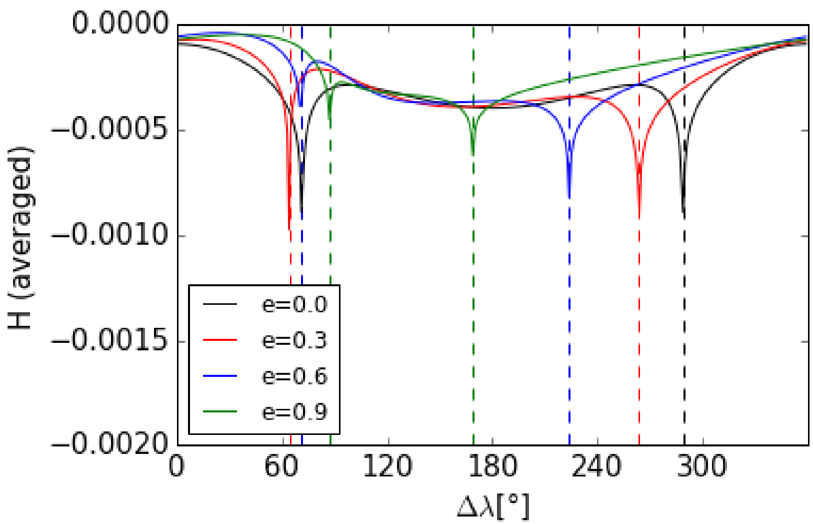

Figure 5: Averaged Hamiltonian function H_{avg} for $e_p = 0.6$ and different e_a with $\Delta\varpi = 90°$, dependent on $\Delta\lambda$. Dashed lines represent the collision orbits for the respective eccentricity.

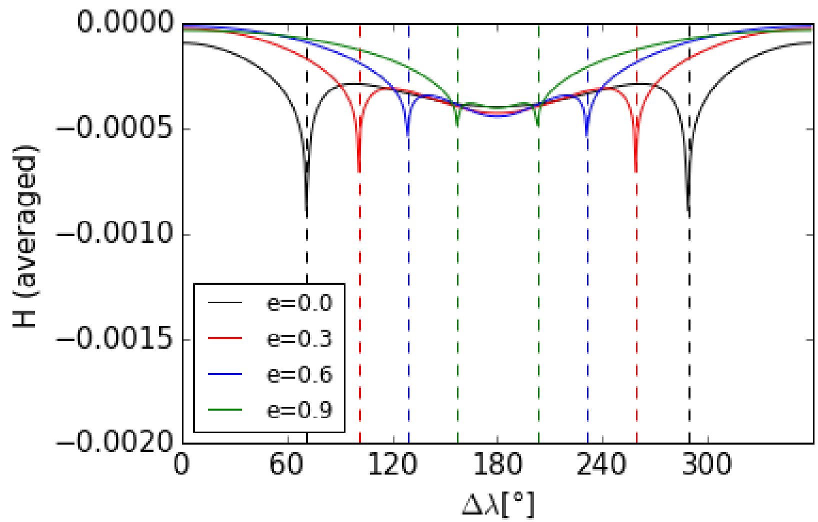

Figure 6: Averaged Hamiltonian function H_{avg} for $e_p = 0.6$ and different e_a with $\Delta\varpi = 180°$, dependent on $\Delta\lambda$. Dashed lines represent the collision orbits for the respective eccentricity.

In contrast, the case $e_p = 0.6$, $e_a = 0.9$, and $\Delta\varpi = 180°$ (green line in Figure 6) has a very short interaction time, as seen in Figure 8. The approach is close to perihelion, and the angle under which the orbits intersect is large. The objects spend a little over 1% of their orbital period closer than 0.1 AU. This short interaction time results in a comparatively shallow collision minimum of H_{avg}.

The contours of the averaged Hamiltonian for $e_p = 0.6$ and $a_a = 1\,\mathrm{AU}$ are shown in Figures 9-11. They display the phase space of the 1:1-resonance. One of variables e_a, $\Delta\lambda$, or $\Delta\varpi$ was fixed at a certain value, while the other two were varied over a grid in steps of 0.01 for the eccentricity, and 1° for the two angles, respectively. Lines in the plot show contours of constant H_{avg}, which represent potential orbital paths of an object under the approximations that were made. There is a clear maximum at $\Delta\varpi = 180°$ and $\Delta\lambda = 0°$, which is present for all asteroid eccentricities. In the case of $e_p = 0.6$, the global maximum of the averaged function lies at approximately $e_a = 0.55$. This represents an anti-aligned quasi-satellite orbit.

Figure 9 shows the contours of $\Delta\lambda$ and $\Delta\varpi$ for $e_a = 0.0; 0.3; 0.6; 0.9$. The upper left panel represents circular asteroid orbits. Horizontal cuts through the plot correspond to the black lines in Figures 4-6:

- The profile of H_{avg} is independent of $\Delta\varpi$, therefore there is no vertical structure in the depicted phase space.
- The maximum in the quasi-satellite region, the two maximum Trojan points and the minimum at $\Delta\lambda = 180°$ are visible.

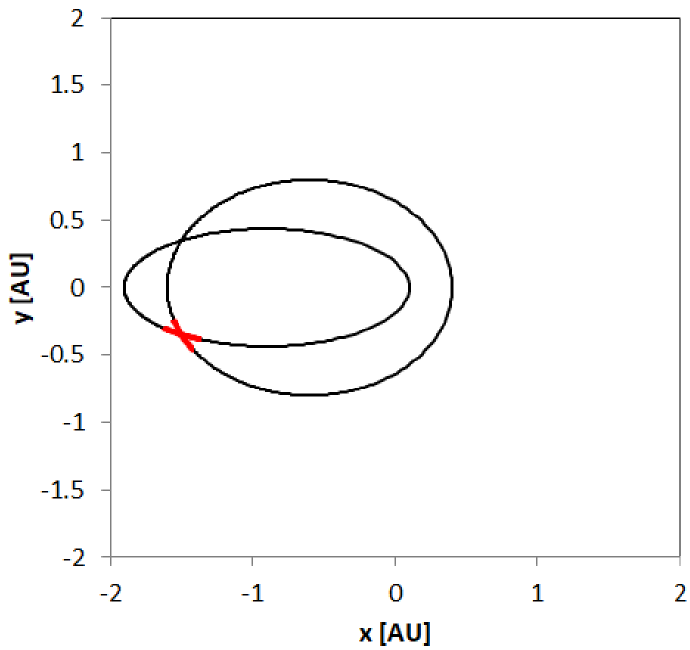

Figure 7: View from above on orbits with, $e_p = 0.6$, $e_a = 0.9$, and $\Delta\varpi = 0°$. The section where bodies are closer than 0.1 AU during one of the two collision orbits is marked in red.

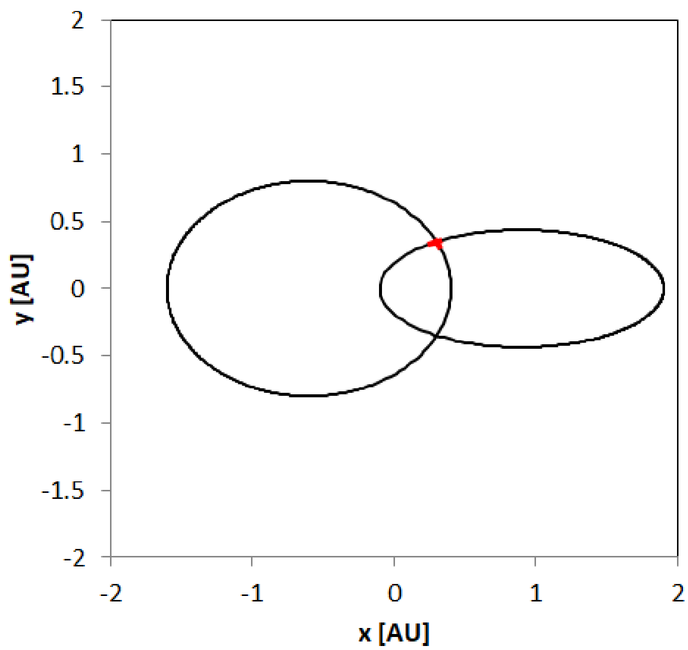

Figure 8: View from above on orbits with, $e_p = 0.6$, $e_a = 0.9$, and $\Delta\varpi = 180°$. The section where bodies are closer than 0.1 AU during one of the two collision orbits is marked in red.

- The clear divide between the Trojan regions and the quasi-satellite region corresponds to the averaged Hamiltonians' collision minimum around $\Delta\lambda = 70°$ (compare again Figures 4-6).

The difference in the longitude of perihelion $\Delta\varpi$ becomes important for e_a different from 0, and the phase space gains a vertical structure. The upper right panel of Figure 9 depicts the case of $e_a = 0.3$. Horizontal cuts at $\Delta\varpi = 0; 90; 180°$ correspond to the red lines in Figures 4-6:

- The topology of the phase space is rotationally symmetric around $\Delta\lambda = 180°$ and $\Delta\varpi = 180°$.
- The quasi-satellite island is centered around $\Delta\lambda = 0°$ and $\Delta\varpi = 180°$. The island takes all of the phase space until the collision minimum. Its center is slightly tilted counterclockwise.
- The collision minimum reaches lower values of $\Delta\lambda$, for $\Delta\varpi$ around 0°. It is also broader at this location.
- The closed curves of the quasi-satellite region primarily revolve around the maximum. Some closed curves in the outer part of this region circle through all values of $\Delta\varpi$.
- The two Trojan maxima also form islands centered around $\Delta\lambda = 60, 300°$ and $\Delta\varpi = 70, 290°$, respectively. They are elongated in the direction of $\Delta\varpi$.
- The Trojan island is tilted clockwise and follows the curve of the collisional minima.
- The central local minimum at $\Delta\lambda, \Delta\varpi = 180°$ has a valley reaching to all values of $\Delta\varpi$. Orbits following curves around this maximum can be associated with horseshoe configurations.

The case $e_a = 0.6$ is depicted in the lower left panel of Figure 9,corresponding to the blue curves of Figure 4-6:

- The quasi-satellite region encompasses a larger part of the phase space than for lower e_p.
- The region around $\Delta\varpi = \Delta\lambda = 0°$ is excluded from the island, since it coincides with orbits lying directly above one another.
- Around $\Delta\varpi = 180°$, the quasi-satellite region extends much further than $\Delta\lambda = 60°$, which is the center of the Trojan region for circular orbits. It reaches $\Delta\lambda = 120°$.

Figure	e_p	a_a[AU]	e_a	$\Delta\varpi[°]$	$\Delta\lambda[°]$
9	0.6	1	0,0.3,0.6,0.9	0,1,...,360	0,1,...,360
10	0.6	1	0,0.01,...,0.99	0,1,...,360	0
11	0.6	1	0,0.01,...,0.99	0,1,...,360	90
12	0,0.01,...,0.99	1	0,0.3,0.6,0.9	180	0

Table 2: Orbital parameters for the H_{avg} contour plots in Figures 9-12

- The counterclockwise tilt of the center of the quasi-satellite region is still visible at $e_a = 0.6$, where the collision border tilts in the opposite direction along with the islands around the Trojan maxima. This results in the Hamiltonian being much steeper around $\Delta\lambda = 90°$, $\Delta\varpi = 50°$, as compared to most other parts of the quasi-satellite region.

- The position of the Trojan maxima and its central fixed point do not change, but the stability island becomes narrower and its maximum moves closer to the collision line. As a consequence, Trojan orbits are only possible for certain values of $\Delta\varpi$ and they are very sensitive to small perturbations.

These tendencies continue for $e_a = 0.9$ (lower right panel of Figure 9, green lines in Figures 4-6):

- The quasi-satellite region again occupies a larger part of the phase space than at $e_p = 0.6$. The island extends almost tol $\Delta\lambda = 180°$ for some values of $\Delta\varpi$, making the Trojan region almost disappear.

- The Trojan maxima are still visible, but they are very close to collision orbits. From $\Delta\varpi = 0°$-$180°$, the collision line close to L_4 is tilted almost in a $45°$ angle. It becomes much steeper after its rightmost point at approximately $\Delta\varpi = 270°$.

Figures 10 and 11 cut the phase space at $\Delta\lambda = 0°; 60°$, respectively. The orbits in the quasi-satellite region can revolve around the maximum or around the collision orbit minimum. The Trojan region is only visible for $\Delta\varpi$ around $60°$ for $\Delta\lambda = 60°$. The Trojan region occupies a larger part of the phase space at $\Delta\lambda = 90°$ (not depicted) where the maximum has shifts to a perihelion longitude of $100°$.

The phase space position of the maximum of the quasi-satellite island for a fixed planetary eccentricity determines the location of the corresponding fixed point. The relevant phase space is e_p-e_a, since the maximum always lies at $\Delta\lambda = 0°$ and $\Delta\varpi = 180°$. Figure 12 displays this phase space. It is symmetric with respect to both eccentricities because the calculation is also symmetric, aside from the barely noticeable barycentric correction of the velocities. The absolute maximum of the phase space lies at $e_a = 0.565$. It is encompassed by triangular-shaped contours. H_{avg} becomes very small for low eccentricities due to the collision minimum. The contours are almost perfectly straight lines with $e_p + e_a = const.$.

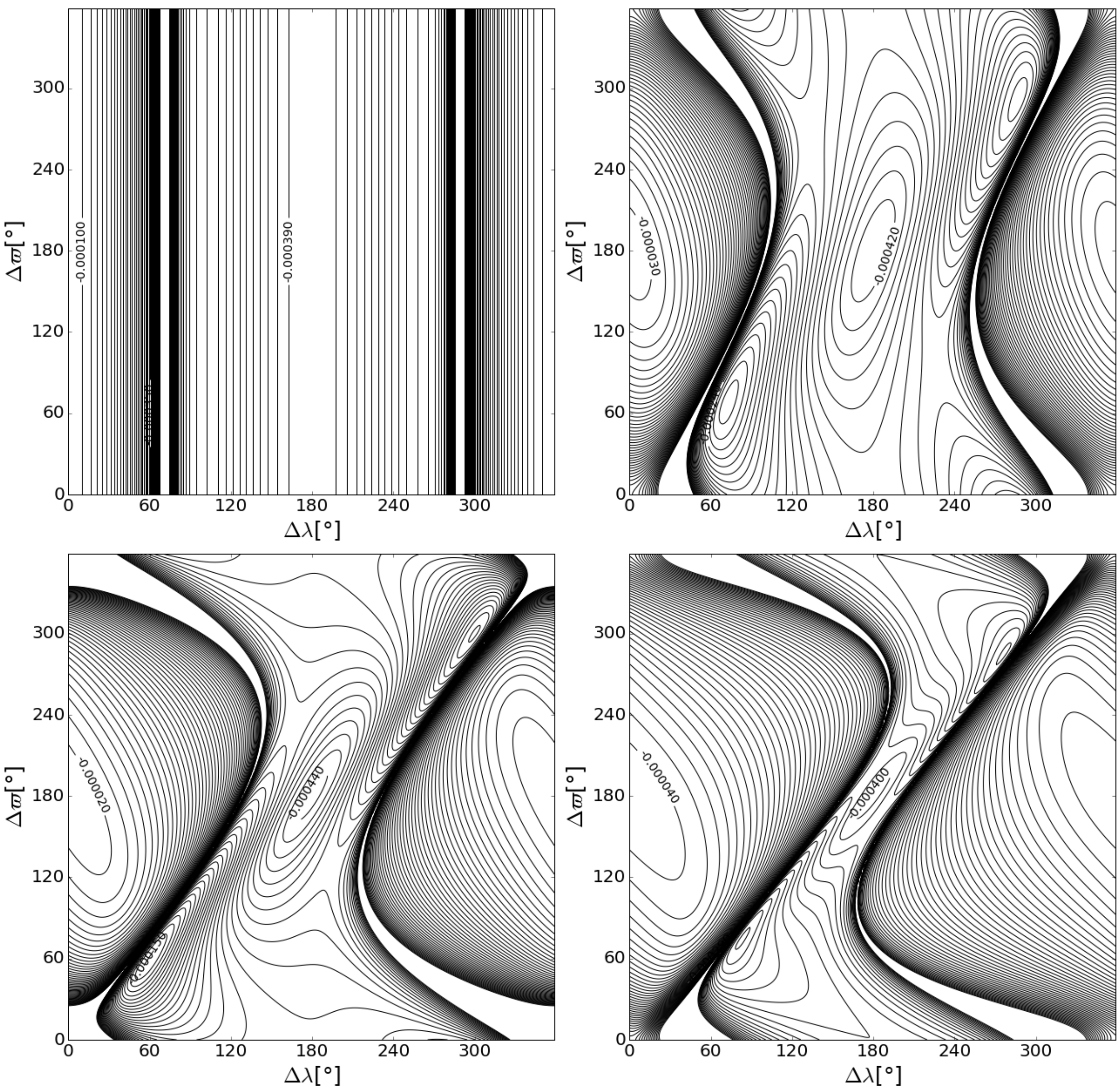

Figure 9: Contours of the averaged Hamiltonian at $e_p = 0.6$, $a_a = 1$, and $e_a = 0$ (upper left), $e_a = 0.3$ (upper right), $e_a = 0.6$ (lower left), and $e_a = 0.9$

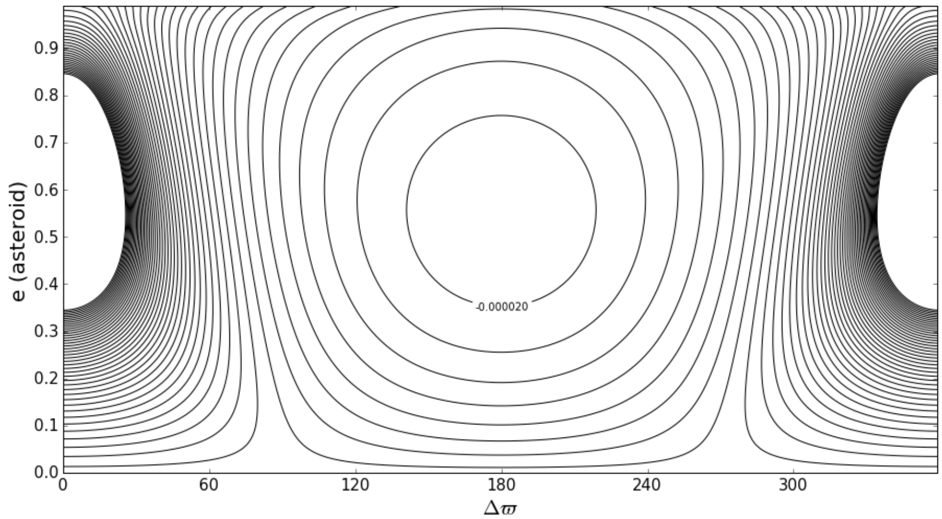

Figure 10: Contours of the averaged Hamiltonian at $e_p = 0.6$, $a_a = 1$, and $\Delta\lambda = 0°$

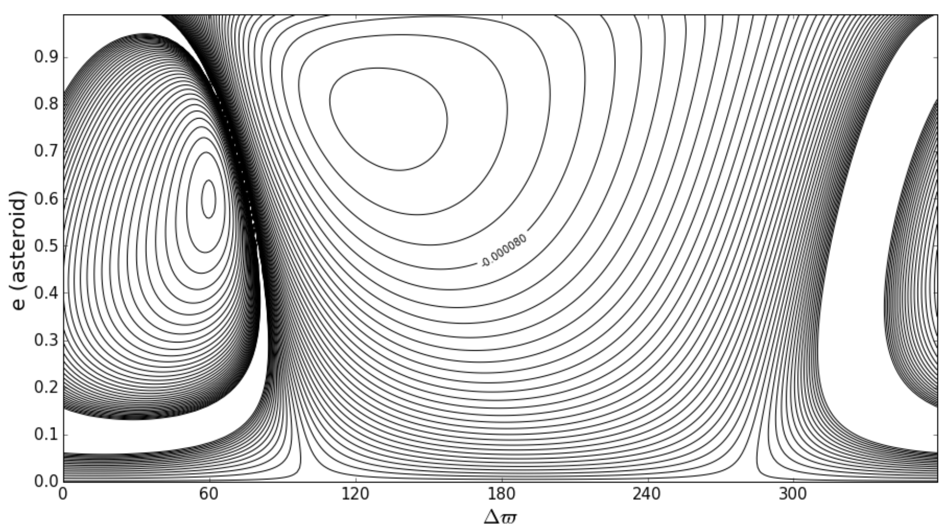

Figure 11: Contours of the averaged Hamiltonian at $e_p = 0.6$, $a_a = 1$ and $\Delta\lambda = 60°$

e_p was fixed to find the equilibrium points. H_{avg} was calculated for the different values of e_a, and its maximal value was identified. $\Delta\lambda = 0°$ and $\Delta\varpi = 180°$ were kept constant. The maxima were determined up to the fifth decimal digit, using a simple grid refining technique: At first, the approximate location was calculated by testing all values of e_a from 0 to 1, and a maximal value was identified. The region around this first estimate was searched with a finer grid. This procedure is generally unproblematic because of the smoothness of H_{avg}.

Figure 13 shows the location of the maxima for all eccentricity values from 0-0.99. Note that for $e_p > 0.92$ the number of points in one orbit was increased, until the result in the Simpson integration of H_1 converged. The results show that the equilibrium point lies at high eccentricity for circular planet orbits, starting at $e_a = 0.835$ and then steadily moves to lower eccentricities. It reaches its lowest point at $e_{planet} = 0.82$ with a value of 0.474, and then increases again for the highest eccentricities, where it exceeds 0.7 for the most elliptic planet orbits.

It may seem counterintuitive that the maxima of the Hamiltonian, which is symmetric with respect to the two involved eccentricities, do not lie on a symmetrical curve. This is because the maxima were not taken absolutely, but along a very clearly defined line in the phase space of Figure 12 ($e_p = const.$). If the problem was extended to a scenario where all three bodies have a non-negligible mass, the maxima would be searched with respect to mass-weighted eccentricities. This was conducted by Giuppone et al. (2010), whose results for high mass ratios approach the one in Figure 13. They also found the global maximum around $e = 0.565$, which is the point where the equilibrium lines of the different mass ratios cross.

2.2 Numerical exploration of quasi-satellite configurations

2.2.1 Coplanar case

The actual trajectories of quasi-satellite objects were investigated via numerical integration, after the phase space structure of the coorbital resonance was analyzed with the semi-analytical model. Integrations were run with a Lie Series integrator (introduced in Hanslmeier and Dvorak (1984)) with adaptive time step. All calculations were performed using 12 terms of the Lie series, an accuracy of 10^{-11} and a minimal time step of 10^{-11} days.

The basic quasi-satellite case is considered in a R3BP framework with one central star, one massive planet and a massless body. Since massless bodies do not interact with one another during an integration, it is possible to simultaneously integrate many of them with one planet without changing the result.

To be able to compare the results with the semi-analytical calculation, the study was begun with the coplanar case under following initial conditions: The central body was assumed to have one solar mass. The planetary body was set to have 1/1000 of that mass (approximately the mass of Jupiter) and to be an orbit at $a_p = 1\,\mathrm{AU}$. The parameters i_p, Ω_p, ω_p were all set to 0°, $M_{p,t=0}$ was set to 90°. e_p was varied in steps of

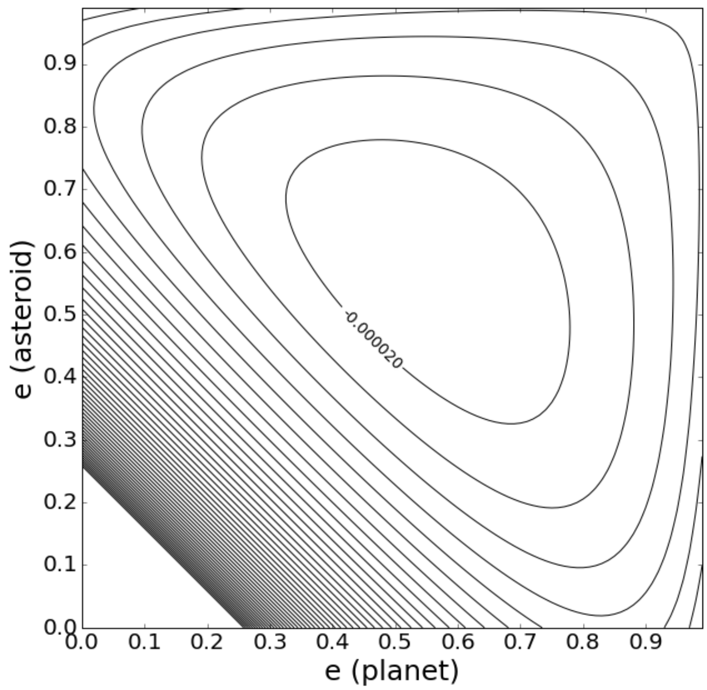

Figure 12: Contours of the averaged Hamiltonian at $a_a = 1$, $\Delta\lambda = 0°$, and $\Delta\varpi = 180°$

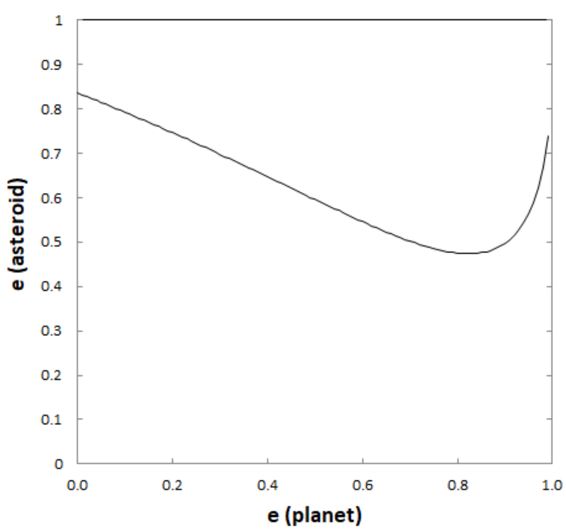

Figure 13: Maxima of the averaged Hamiltonian for $\Delta\lambda = 0°$, and $\Delta\varpi = 180°$, with a fixed e_p, taken with respect to e_a

	a[AU]	e	$i[°]$	$\Omega[°]$	$\omega[°]$	$M[°]$	$m[M_\odot]$
Planet	1	0, 0.01,..., 0.99	0	0	0	90	0.001
Asteroid	1	0, 0.01,..., 0.99	0	0	0,180	$90-\omega$	0

Table 3: Initial conditions for the coplanar numerical simulations

0.01 from 0 to 0.99. This resulted a total of 100 integrations, each with a planet on a slightly different orbit.

Each of the resulting 100 systems was integrated with massless bodies, using the following initial conditions: For the initially anti-aligned population, the bodies were put at $a_{a,t=0} = 1\,\mathrm{AU}$ with $i_{a,t=0} = \Omega_{a,t=0} = 0°$, $\omega_{a,t=0} = 180°$ (since the configuration is coplanar $\Delta\omega$ is equivalent to $\Delta\varpi$), and $M_{a,t=0}$ was set to 270°. This guarantees that the initial resonance angle $\Delta\lambda$ was at 0° for those objects. In principal any combination of M_p and M_a can be used as long as their difference is 180°. The 90°/270°-combination was chosen because the barycentric transformation performed by the integrator can introduce artifacts in the output, that are maximal when the heliocentric distances of the objects are small. This effect is minimized when both objects are started far from perihelion. This configuration was also used in all following integrations when applicable.

The eccentricity of the asteroids was again varied in steps of 0.01 from 0 to 0.99, yielding 100 anti-aligned asteroids for each planet. Additional objects were put at $\omega_{a,t=0} = 0°$ and $M_{a,t=0} = 90°$ to account for the co-aligned part of the phase space. This resulted again in a resonance angle of $\Delta\lambda = 0°$, which is suitable for a quasi-satellite orbit. Eccentricities with $|e_p - e_a| < 0.1$ were not considered to avoid close encounters with the planetary body. Objects with initial conditions in this vicinity can be assumed to be chaotic. This procedure yielded 80 to 90 co-aligned asteroids for each planet. The total was 180 to 190 massless bodies for each initial condition of the planet. The integration time was set to 10000 years. Objects with an eccentricity greater than 0.995 were removed from the system and categorized as having collided with the star. The initial conditions described in this section are displayed in Table 3.

Figure 14 shows e_p-e_a values for which the asteroid remains within the coorbital resonance. As a stability criterion, the maximum deviation of the semi-major axis over the entire integration time was used:

$$\epsilon = max(|\log a_{a,min}|, |\log a_{a,max}|) \tag{40}$$

This criterion is not a general indicator, as it is specific to the 1-to-1-resonance at 1 Astronomical Unit. Objects colliding with the sun sometimes temporarily assume negative values of a. In this case, ϵ was artificially set to an arbitrarily high value outside of the stability domain. $\epsilon = 0.1$ was empirically determined to be a reliable value for distinguishing resonant and non-resonant orbits. $\epsilon < 0.1$ corresponds to a 0.9-1.1 AU semi-major axis range. A slight variation of the distinguishing ϵ-value does not affect the result. The point in time where ϵ first assumes a value larger than 0.1 is used as the color code in the stability maps. It is defined as the *resonance lifetime*.

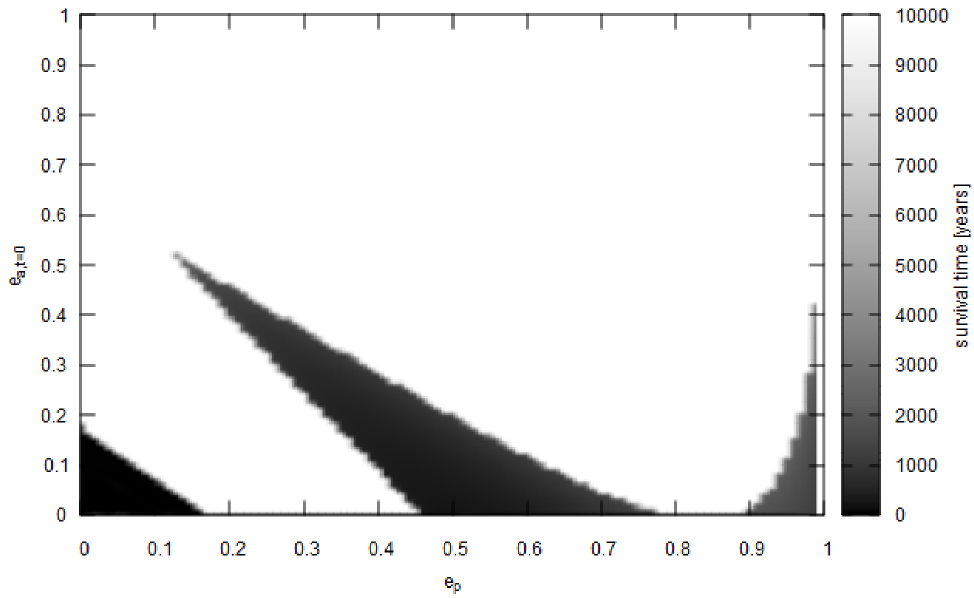

Figure 14: Resonance lifetimes of the $\Delta\varpi = 180°$ asteroids with the initial conditions of Table 3

Different criteria, such as the amplitude of $\Delta\lambda$ or $\Delta\varpi$ can be used, depending on the orbit, to distinguish stable orbits from each other.

Figure 14 shows that most e_p-e_a combinations of anti-aligned orbits in the quasi-satellite region lead to resonant orbits. There are two regions where resonant orbits are not possible: If both eccentricities are low, the orbits are chaotic because of close encounters. Low-eccentricity quasi-satellites are also unstable for mid-range planetary eccentricities. This region continues in a triangular structure, extending to higher values of e_a. The reason for instability in this region can be understood when analyzing the trajectories of objects in the region: Their orbital evolution takes them to orbits with e_a approaching 1, which leads to a collision with the star. The same is true for many objects at very high e_p. In the rest of the diagram the objects have stable trajectories. $\Delta\varpi$ librates around 180° or 0° for some of them. Objects with this behavior will be referred to as *librating* objects for the rest of this work. Other objects undergo a precession through all values of $\Delta\varpi$ from 0° to 360°. Those objects will be referred as *precessing* objects. The phase space is analyzed for a more detailed description.

Figures 15 and 16 show the evolution in the e_a-$\Delta\varpi$-phase space for ten different planetary eccentricities. The different regions already determined in the semi-analytical framework (compare e.g. Figure 10 to upper left panel of Figure 16) quickly become apparent. For $e_p = 0$ (upper left panel in Figure 15), the phase space has the following characteristics:

- The orbital evolution takes place primarily in $\Delta\varpi$, and the eccentricities do not change much.
- If an objects' eccentricity is close to the fixed point at $e_p = 0.835$ (compare Figure 13), its evolution in phase space is slow.
- $\Delta\varpi$ evolves towards lower values for objects with e_a lower than the value at the fixed point. It moves to higher values for objects with higher e_a. Evolution towards lower values corresponds to clockwise precession of the orbit, whereas evolution towards higher values corresponds to counterclockwise precession.
- The integration time is not long enough to complete a full precession for the objects closest to the fixed point. For this reason, lines showing their paths do not reach around all values of $\Delta\varpi$.
- The variation in e_a becomes larger for the lowest values of asteroid eccentricity, and individual orbits change in a more chaotic manner. This aspect is not represented in the semi-analytical framework of the last section. Close encounters, that become more common at low e_a, cause the variations. The close encounters lead to orbital instability and an ejection from the resonance for eccentricities lower than 0.18.

As already discussed in Section 2.1, when the planetary eccentricity differs from 0, a massless object also experiences an orbital evolution in e_a:

- Orbits whose perihelion undergoes a precession through all values are common for low-to mid planetary eccentricities (Figure 15).
- Most of these precessing orbits pass $\Delta\varpi = 180°$ with a lower eccentricity than that of the anti-aligned fixed point. The eccentricity of the objects increases and the objects pass $\Delta\varpi = 0°$ with an eccentricity higher than both their initial value and that of the identical orbit (where $e_p = e_a$).
- In the upper right panel of Figure 15 it can be seen that it is also possible for precession orbits to pass $\Delta\varpi = 180°$ with a higher eccentricity than the anti-aligned fixed point.
- The closer the orbit of one object is in phase space to the planetary orbit, the higher is its short-term variance in the orbital elements.
- The part of the phase space where objects are carried to eccentricities close to unity is located between the librating and the precessing objects. In this part, long-time stability is not possible. The orbital evolution corresponds to a collision with the star.

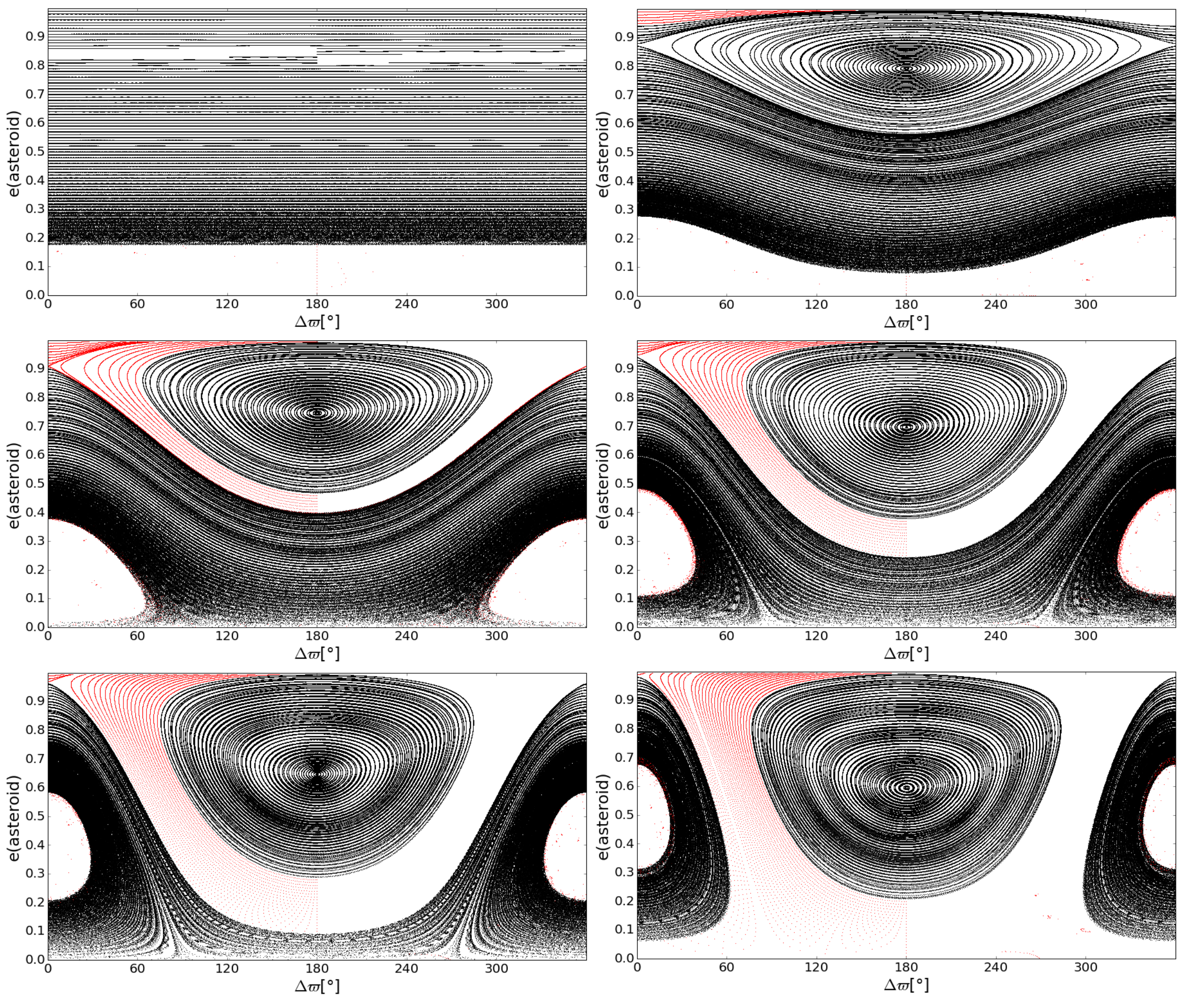

Figure 15: $e_a - \Delta\varpi$-phase space for initial conditions of Table 3. Stable orbits are in black, unstable objects in red. Objects are only followed until ejection from the resonance. Individual panels represent $e_p = 0$ (upper left), $e_p = 0.1$ (upper right), $e_p = 0.2$ (middle left), $e_p = 0.3$ (middle right), $e_p = 0.4$ (lower left), and $e_p = 0.5$ (lower right).

- The star-colliding region becomes broader for higher planetary eccentricities and makes the precession orbits disappear between $e_p = 0.4$ and $e_p = 0.5$. In Figure 14, the star-colliding objects are responsible for the zipper-like structure, visible between the two large stable regions.

- Objects can librate around the fixed points at $\Delta\varpi = 0, 180°$. They cannot closely approach the fixed point at $\Delta\varpi = 0°$.

- Libration around $\Delta\varpi = 0°$ is only possible between planetary eccentricities of 0.2 and 0.7. These orbits directly border the precession region if it exists. Due to their proximity to the orbit of the planet, asteroids in this region experience a large variation in their orbital elements and close encounters. Some of the orbits become unstable after a number of librations around the fixed point. This is best observed in the upper right panel of Figure 16 ($e_p = 0.7$). This panel also shows that the orbits which become unstable do not necessarily have to be the innermost ones. Chaotic effects play a more significant role in the region around $\Delta\varpi = 0°$, compared to other parts of the phase space.

- The anti-aligned quasi-satellite fixed point ($\Delta\varpi = 180°$) is stable for all planetary eccentricities. The e_a value at the fixed point corresponds to the values in Figure 13. For a more detailed comparison, see section 2.2.2.

- The libration zone extends to values of ω_a under $50°$ for the lowest planetary eccentricities (upper right panel of Figure15), and to approximately $90°$ for most other values. The region extends as low as $e_a = 0.05$ for $e_p = 0.8$ and $e_p = 0.9$. The upper border is constrained by the precession orbits for low planetary eccentricities, and by the star-colliding orbits for most other values.

- There is a noticeable bump in the $e_a{-}\Delta\varpi_a$-evolution at high asteroid eccentricities for planetary eccentricities larger than 0.7. This makes the otherwise convex phase space curve bend inward. This behavior is not seen in the semi-analytical results of Section 2.1, but it should be noted that the $\Delta\lambda = 0°$ condition enforced there is not necessarily present in the numerical result. Instead, we see a projection of $e_a - \Delta\varpi$ at other $\Delta\lambda$-values.

Figure 17 provides insight into the evolution of $\Delta\lambda$ with respect to $\Delta\varpi$ for the cases $e_p = 0$, $e_p = 0.3$ $e_p = 0.6$ and $e_p = 0.9$. Only ten of the 100 initially anti-aligned objects and eight of the 80 initially co-aligned orbits are depicted for visibility reasons. The lower left panel of Figure 17 can be compared to all the panels of Figure 9 (which has $e_p = 0.6$ in all of them), that cut the phase space at different eccentricities. The lines in Figure 9 are not followed exactly, since the eccentricity of the objects is not constant. Some features such as the tilt of the quasi-satellite island are nonetheless noticeable. The individual panels of Figure 9 can also be compared with their counterparts in Figure 17, since the Hamiltonian calculations are symmetric with respect to e_p and e_a. They can be seen as cuts at $e_a = 0.6$ in the numerical plots.

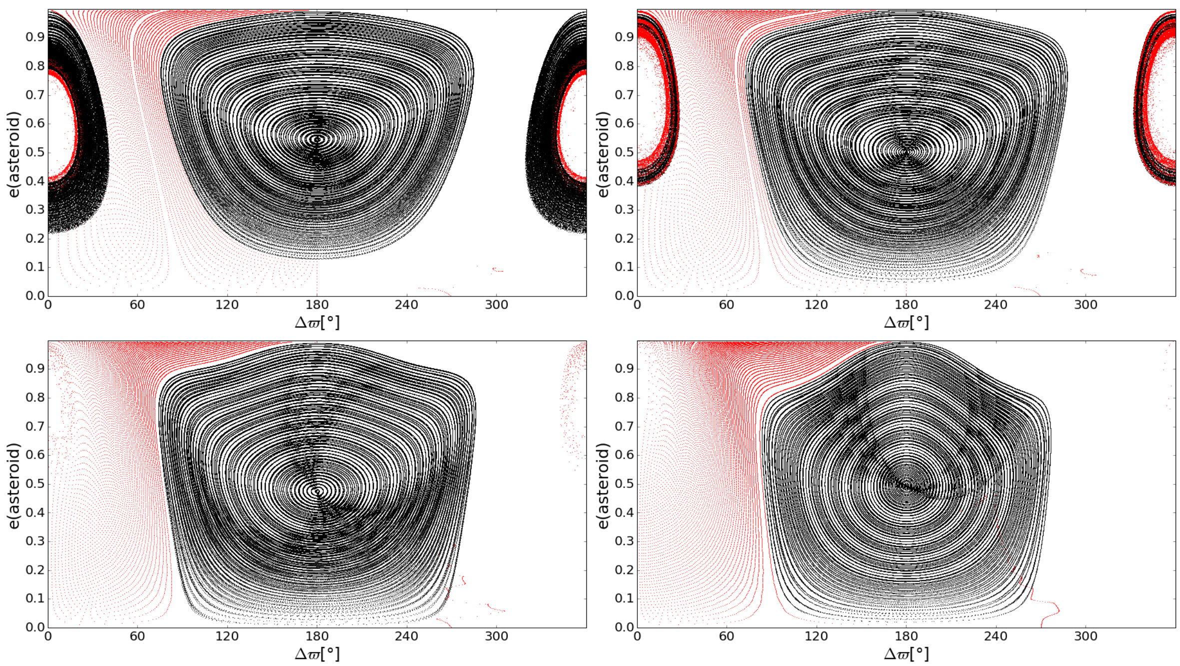

Figure 16: $e_a - \Delta\varpi$-phase space for initial conditions of Table 3. Stable orbits are in black, unstable orbits in red. Objects are only followed until ejection from the resonance. Individual panels represent $e_p = 0.6$ (upper left), $e_p = 0.7$ (upper right), $e_p = 0.8$ (lower left), and $e_p = 0.9$ (lower right).

The $e_p = 0$ case is depicted in the upper left of Figure 17:

- The initial $\Delta\lambda$ stays mostly constant. As seen in the top left panel of Figure 15, there is only an evolution in $\Delta\varpi$.
- $\Delta\varpi$ passes through all possible values between $0°$ and $360°$.
- The variation in $\Delta\lambda$ is generally less than $10°$ and mainly due to perturbations from close encounters.

There are some structures dependent on $\Delta\lambda$ when e_p differs from 0:

- At $e_p = 0.3$ (upper right panel of Figure 17), the stability island is tilted counter-clockwise, as seen in the semi-analytical plots.
- Precession and libration orbits likewise assume values of $\Delta\lambda$ different from $0°$. The star-colliding orbits between them follow the same trend.
- The maximum deviation of $\Delta\lambda$ occurs around $\Delta\varpi = 90, 270°$, it takes a value of approximately $15°$ for the outermost precession orbits.
- The deviations become larger with $e_p = 0.6$ (lower left panel of Figure 17)
- The libration orbits follow a two-sided loop in the phase space and reach their maximum deviation in $\Delta\lambda$ and $\Delta\varpi$ in quick succession.
- The maximum deviation curve traced by these orbits resembles a sine. The amplitude is around $45°$ in the $e_p = 0.6$ case.
- The stable co-aligned libration orbits (compare upper left panel in Figure 16) are visible around $\Delta\varpi = 0°$. Their maximal amplitude in $\Delta\lambda$ is smaller than that of the anti-aligned orbits, but their short-term variation is larger.
- The loop-like behavior is more prominent for the case $e_p = 0.9$ (lower right panel of Figure 17). The loops extend over $\Delta\lambda = 60°$ for some ejection orbits and around $\Delta\lambda = 50°$ for libration orbits.

The time duration of the librations is another interesting aspect of the phase space evolution of quasi-satellites. For this, the secular periods must be determined. It is not necessary to implement complex methods of frequency analysis since the orbits are all closed. One secular period has elapsed when a phase space point close to the initial conditions is reached again. This was measured with the parameter:

$$\delta = \left(e_a - e_{a,t=0}^2\right) + \left(\Delta\varpi - \Delta\varpi_{t=0}^2\right) \tag{41}$$

A point in time was noted if δ had a minimum and fell below a certain value (which needed to be fine-tuned between 0.0001 and 0.01 to catch rapidly evolving objects and

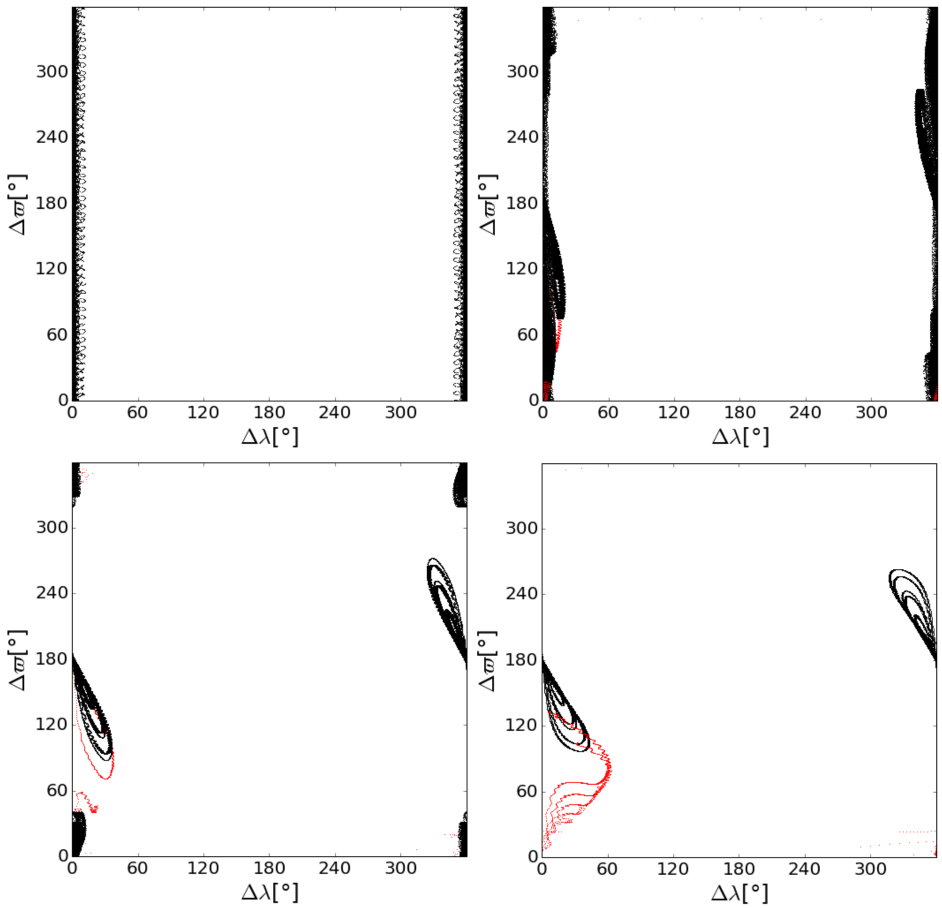

Figure 17: $\Delta\lambda$-$\Delta\varpi$-phase space for initial conditions of Table 3. Stable orbits are in black, unstable orbits are in red. They are only followed until ejection from the resonance. Individual panels represent $e_p = 0$ (upper left), $e_p = 0.3$ (upper right), $e_p = 0.6$ (lower left), and $e_p = 0.9$ (lower right).

to avoid local minima, according to the type of orbit). The average time span between two such points during the total integration time of 10000 years was defined as the *secular period* or *oscillation period*. Its inverse is the secular frequency g.

The method described above gave consistent results for all resonant objects except for those close to the fixed point. In this case, the orbit always stayed very close to its initial conditions. It was impossible to find periodic minima of δ in their orbital evolution with this method. The period values close to the fixed point were linearly interpolated between the values neighboring it for optical reasons. The period was longer than the integration time for some objects. The maximum value of 10000 years was used in the diagrams for these objects. Objects leaving the resonance were assigned the period 0.

The results for all calculations of Table 3 are shown in the top panel of Figure 18. Secular periods at six e_p values characteristic for the evolution are plotted in the bottom

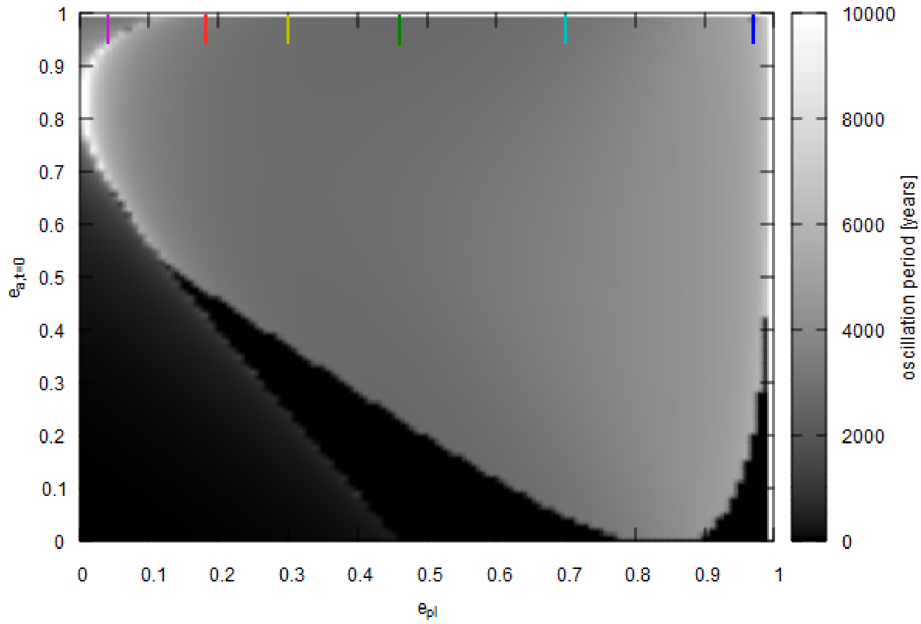

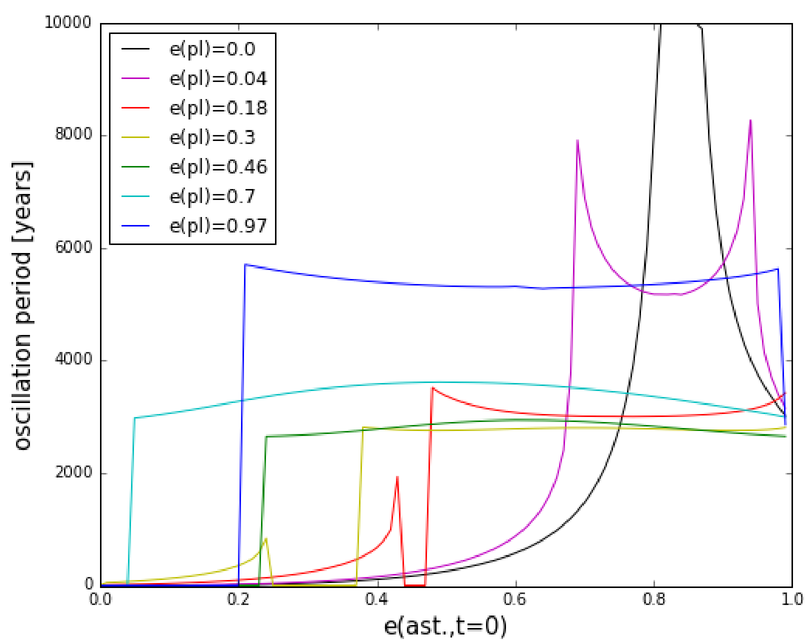

Figure 18: Oscillation periods for coplanar initially anti-aligned quasi-satellites (initial conditions in Table3). The top panel shows a heat map of all objects, the bottom panel shows the periods of objects with selected e_p values (marked in the top diagram with the respective colour).

panel.

- In general, the oscillation period for the precessing objects are shorter, typically ranging between 10 years and a few hundred years. The librating objects usually have oscillation periods between 2500 and 5000 years.

- Objects with smaller initial eccentricity have a more rapid orbital evolution. The only precessing objects with oscillation periods comparable to the librating objects are found in cases with very low e_p.

- At $e_p = 0$ (black curve in the bottom panel of Figure 18), it can be clearly seen that the objects close to the fixed point ($e_a = 0.835$) have the slowest oscillation periods, which exceed 10000 years. The periods quickly become shorter and do not exceed 100 years for asteroid eccentricities smaller than 0.4. The innermost stable object at $e_{a,t=0} = 0.19$ has an oscillation period of just over 6 years.

- The general pattern changes slightly for $e_p = 0.04$ (purple curve in Figure 18), where the objects with librating $\Delta\varpi$ occupy a significant part of the phase space. The precessing orbits still have short oscillation periods, that increase with increasing eccentricity. In the libration region, the longest periods are reached at the edges of the region, and there was a minimum close to the fixed point. The curve in the libration region is approximately symmetric, since objects that are started at the lower border pass $\Delta\varpi = 180°$ again at high eccentricity, and vice versa. The periods are in the range of 5000-8000 years.

- The periods decrease when e_p increases. At $e_p = 0.18$ (red curve in Figure 18), they last around 3000 years while the minimum is still at the fixed point. The sun-colliding gap, which exists between the precessing and the librating objects, starts to appear.

- An interesting phenomenon begins to occur around $e_p = 0.3$ (yellow curve in Figure 18). The $e_{a,t=0}$ for which the secular period in the librating region is minimal begins to deviate from the fixed point and moves towards the border. At this point all librating objects have an almost constant secular period between 2750 and 2820 years.

- As this evolution continues, the shortest secular periods are found at the border of the libration region. The shortest oscillation period of any librating object is found at $e_p = 0.46$ (green curve in Figure 18) with $e_a = 0.24$ and 0.99. This period is about 2650 years. The secular periods around the fixed point are around 2940 years at this planetary eccentricity. Precessing objects no longer exist.

- The general structure stays the same as the oscillation period increases with higher planetary eccentricities. The periods at $e_p = 0.7$ (cyan curve in Figure 18) are between 2970 years at the border and 3620 years close to the fixed point.

	a[AU]	e	$i[^\circ]$	$\Omega[^\circ]$	$\omega[^\circ]$	$M[^\circ]$	$m[M_\odot]$
Planet	1	0, 0.03,..., 0.99	0	0	0	90	0.001
Asteroid	1.01, 1.02, 1.03, 1.04	0, 0.03,..., 0.99	0	0	180	270	0

Table 4: Initial conditions for the coplanar numerical simulations with perturbed semi-major axis

- A change takes place at around $e_p = 0.89$ when the secular period at the border becomes longer than the one at the fixed point. The periods at $e_p = 0.97$ (blue curve in Figure 18) increase again to almost 8000 years.

More sophisticated methods would need to be applied to explain the observed behavior in detail. Nonetheless, the distinct difference between secular periods of librating and precessing objects demonstrates that the orbital evolution is faster when the small objects spend more time close to the planet. The orbital evolution in $\Delta\varpi$ is slowest when the eccentricity is high, as it requires more energy to alter the perihelion of an orbit in this case. The exact numerical value of the period is determined by the exact fraction of the evolution spent at high and low eccentricity. Librating objects far from the fixed point spend time in both low and high eccentricity regions, whereas objects close to the fixed point remain at mid-eccentricity. This makes it difficult to determine which object has the shorter secular period.

As for the phase space structure, the principal relations of the oscillation periods hold true for all planetary masses and semi-major axis. Their numerical values change for different values of m_p and a_p.

The calculations of the previous section were conducted in the center of the resonance with $a_{a,t=0} = 1\,\mathrm{AU}$. Additional calculations with an initially perturbed asteroid were performed with $a_{a,t=0} = 1.01; 1.02; 1.03; 1.04\,\mathrm{AU}$ to measure the width of the resonance. Only anti-aligned orbits were tested and the size of the eccentricity grid was set to 0.03 for both e_p and e_a to save computation time. This resulted in 34 integrations with 34 massless quasi-satellites in each integration. The initial conditions are summarized in Table 4.

The stability map (again measured with the point in time where ϵ first exceeds 0.1) in Figure 19 shows how stable regions shift if the initial orbit is perturbed:

- The difference to the unperturbed case (Figure 14) is minor for $a_{a,t=0} = 1.01\,\mathrm{AU}$.

- The lower eccentricity limit of the librating region increases at $a_{a,t=0} = 1.02\,\mathrm{AU}$. The region becomes smaller, and the region of objects colliding with the central body becomes larger. There is little change in the stability region of objects with a precessing perihelion.

- These effects are amplified at $a_{a,t=0} = 1.03\,\mathrm{AU}$. There are no stable orbits for the highest planetary eccentricities and no librating orbits below $e_{a,t=0} = 0.4$. The

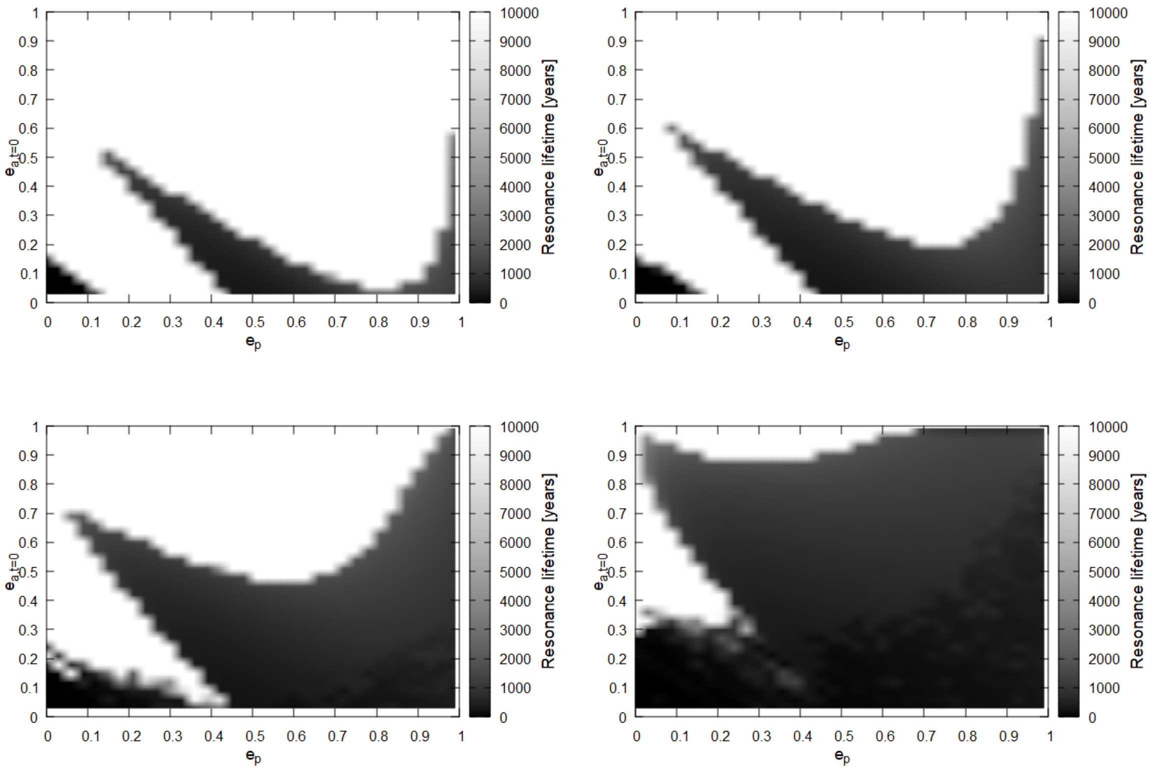

Figure 19: Survival times ($\epsilon < 0.1$) for objects with the initial conditions of Table 4. Individual panels represent $a_{a,t=0} = 1.01\,\mathrm{AU}$ (upper left), $a_{a,t=0} = 1.02\,\mathrm{AU}$ (upper right), $a_{a,t=0} = 1.03\,\mathrm{AU}$ (lower left), and $a_{a,t=0} = 1.04\,\mathrm{AU}$ (lower right).

position of the precession region remains the same, but some objects at the lowest $e_{a,t=0}$ also become unstable.

- The librating region almost completely vanishes for $e_{a,t=0} = 1.04\,\mathrm{AU}$. Only initial conditions of $e_{a,t=0} = 0.9$ or higher can still lead to stable orbits. The precession region also becomes smaller and only begins at eccentricities higher than 0.3.

Some of these effects can be explained by looking at the phase space in Figure 20. At $e_p = 0.6$, mostly the librating region is depicted (compare upper left panel of Figure 16):

- The $e - \Delta\varpi$ curves begin to overlap indicating that the approximation of a constant $\Delta\lambda$ is less valid for the perturbed objects.

- Generally, objects with high $e_{a,t=0}$ have an eccentricity minimum higher than the stable objects with the lowest $e_{a,t=0}$.

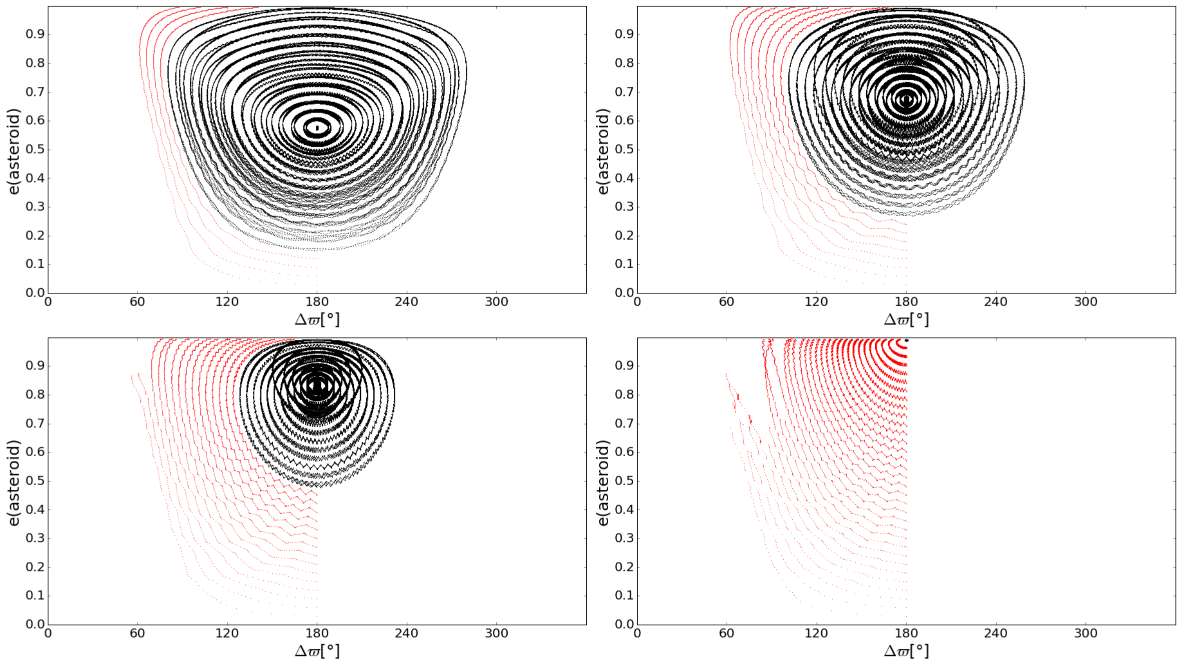

Figure 20: $e_a - \Delta\varpi$ phase space at $e_p = 0.6$ with the initial conditions of Table 4. Individual panels represent $a_{a,t=0} = 1.01\,\text{AU}$ (upper left), $a_{a,t=0} = 1.02\,\text{AU}$ (upper right), $a_{a,t=0} = 1.03\,\text{AU}$ (lower left), and $a_{a,t=0} = 1.04\,\text{AU}$ (lower right).

- The equilibrium point shifts to a higher eccentricity, when $a_{a,t=0}$ increases. It is close to $e_a = 1$ in the most extreme case of $a_{a,t=0} = 1.04\,\text{AU}$.
- The phase space curves also show a very clear zigzag pattern for high perturbation, which suggests that there are short term variations overlaid with the long-term behavior.

Figure 21 depicts the evolution in $\Delta\lambda$ and $\Delta\varpi$:

- Higher perturbations in a_a are associated with higher short-term oscillations in $\Delta\lambda$.
- The horizontal structures in $\Delta\lambda - \Delta\varpi$ correspond to the zig-zag structures in the $e_a - \Delta\varpi$ phase space (Figure 20).
- In the most extreme case, $\Delta\lambda$ can exhibit oscillation between 210° and 150°, which is 85% of the entire range.
- The tilt of the stability island (compare lower left panel of Figure 17) is still visible until $a_{a,t=0} = 1.02\,\text{AU}$.

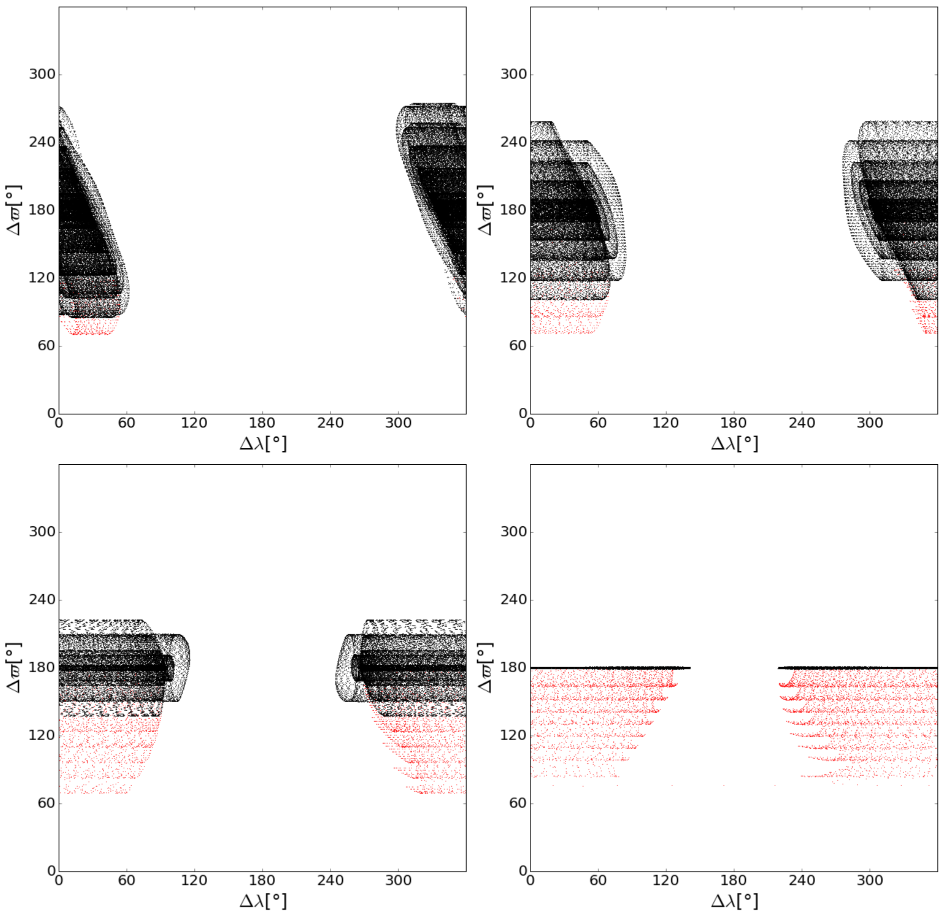

Figure 21: $\Delta\lambda - \Delta\varpi$ phase space at $e_p = 0.6$ with the initial conditions of Table 4. Individual panels represent $a_{a,t=0} = 1.01\,\mathrm{AU}$ (upper left), $a_{a,t=0} = 1.02\,\mathrm{AU}$ (upper right), $a_{a,t=0} = 1.03\,\mathrm{AU}$ (lower left), and $a_{a,t=0} = 1.04\,\mathrm{AU}$ (lower right).

2.2.2 Comparison with the semi-analytical results

The results obtained with the semi-analytical model and the results obtained with numerical integration are compared in this section. The equilibrium points of the anti-aligned quasi-satellite orbit are clearly visible in both $e_a - \varpi$-phase space portraits (Figures 10 and 16). Their exact location with the semi-analytical model was determined in Section 2.1 and is depicted in Figure 13. The locations of the fixed points in the numerical results were identified by finding an orbit, whose maximal deviation from its initial condition was minimal over an extended period of time. Two different criteria were used:

$$\Delta e_a = max(|e_a - e_{a,t=0}|) \tag{42}$$

$$\Delta \omega_a = max(|\omega_a - \omega_{a,t=0}|) \tag{43}$$

Only the first 1000 orbits were taken into account to avoid high-order effects coming from the non-averaged part of the Hamiltonian. The output interval was adjusted to 300 days to avoid artifacts that can arise when it is a multiple of the orbital period. Initial conditions with minimal Δe_a and $\Delta\omega_a$ were searched with a bisection algorithm for all 100 planetary eccentricities. The fixed point determined from the semi-analytical results was used as a first estimate. Aside from the varying e_a, the same initial conditions as in Table 3 were used. Figure 22 shows the difference between the locations of the fixed points determined using the two different methods for all values of e_p:

- The e_a values from both methods show very similar results for all e_p.
- Generally, $\Delta\omega_a$ emerges as the more robust criterion. The numerical equilibrium value for e_a never deviates further than 0.006 from the analytical result. The maximum deviation is only slightly above 0.003, if the three highest planetary eccentricities are excluded.
- Δe_a as a criterion underestimates the eccentricity of the location of the equilibrium point. The exception is the case $e_p = 0$, where it increases the point to the highest possible eccentricities that the integrator allows. This is not surprising, because in this case, the eccentricity does not change significantly for all orbits (compare upper left panel of Figure 15).
- Underestimation in the remaining cases may be due to the fact that the osculating heliocentric orbital elements tend to vary less for lower eccentricities. This introduces a bias for orbits close to the fixed point.
- There is also a sudden increase of the difference function at $e_p = 0.92$, which may be an artifact coming from high-order effects. Such phenomena occur more frequently if a longer part of the integration time is taken into account.

The numerical and the semi-analytical results were also compared in the regions far from the fixed points. The result of a single numerical integration was taken and the averaged Hamiltonian was evaluated for every data point based on the orbital elements at that point. The values of H_{avg} remain constant, if the semi-analytical approximation is valid. A distinct difference is expected, especially for objects with a low minimum distance to the planet, since the integrator incorporates higher-order effects such as close encounters. The deviations are expected to be periodic for orbits on closed curves.

Figures 23-26 show four examples that confirm these predictions:

- Figure 23 shows an orbit librating around $\omega_a = 180°$ at $e_p = 0.9$, an its trajectory is located close to the edge of the region ($e_{a,t=0} = 0.04$). The deviation is always under $4 \cdot 10^{-7}$, which is two orders of magnitude lower than the absolute value of H_{avg} at his location. The general behavior of the function is periodic with respect to the libration period of around 4500 years, but there are slight differences, especially in the height of the two maxima, that occur when the eccentricity is

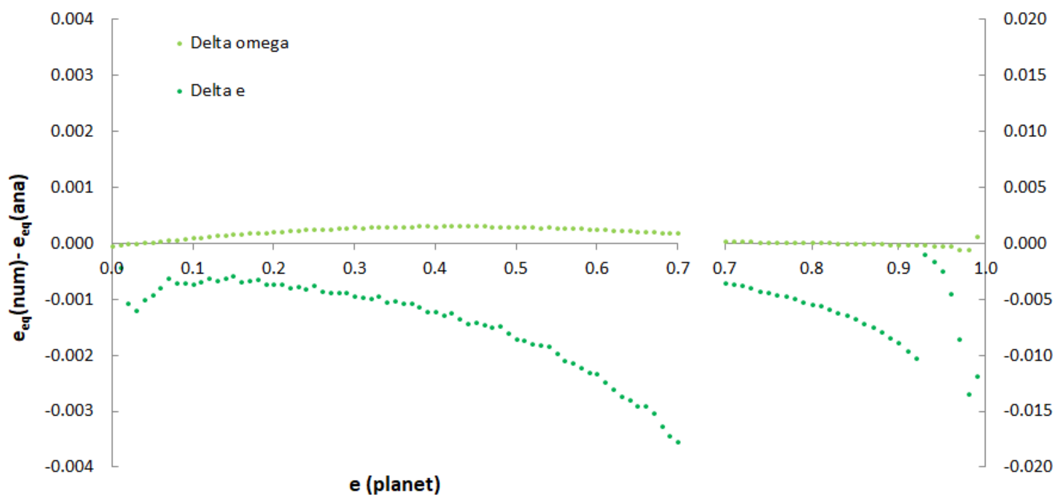

Figure 22: Difference between the analytical and the numerical position for different planetary eccentricities. Note that the scale of the y-axis changes after $e_p = 0.7$.

around 0.95 and the argument of perihelion is 150° and 210°. Comparing the deviation curve to the lower right panel of Figure 16, the maxima correspond to the bump at the highest eccentricities, shortly after the concave portion of the projected phase space. There are also smaller interfering oscillations, that extend over the entire period.

- The variations are smaller for most of the orbit for the second case (Figure 24), which also depicts a librating object at $e_p = 0.9$ and $e_{a,t=0} = 0.3$. They never extend beyond $2 \cdot 10^{-7}$ and the high-frequency oscillations have a low amplitude. The periodicity of the points with maximum deviation stays constant, but their height and direction varies significantly. The entire difference function is mirrored around 8800 years. The reason for this is unclear. The mirroring happens to a lesser extent in Figure 23 around 6800 years.

- Figure 25 is an example of a precession orbit with $e_p = 0.2$ and $e_{a,t=0} = 0.1$. It is one of the precession curves in the middle left panel of Figure 15. The variation of H_{avg} from its initial value is much larger due to greater variance of the orbital elements. The variation is approximately $2 \cdot 10^{-4}$, which is slightly more than one order of magnitude from the absolute value of H_{avg}. The amplitudes of the short-term oscillations are dominant, but there is also long-term behavior with an oscillation period just over 2000 years.

- The last case in Figure 26 depicts an orbit librating around $\Delta\varpi = 0°$ with $e_p = 0.6$ and $e_{a,t=0} = 0.35$ (compare upper left panel of 16). This object's orbit is very close to the planetary orbit. This causes the variation of the orbital elements to be very high. H_{avg} varies by $7 \cdot 10^4$, less than an order of magnitude smaller than

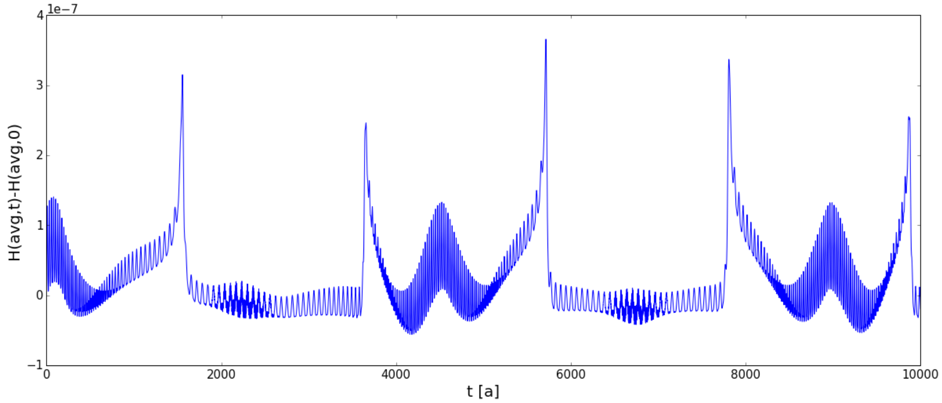

Figure 23: Change of the averaged Hamiltonian from its initial value for the initial conditions $e_p = 0.9$, $e_{a,t=0} = 0.04$, $\Delta\varpi = 180°$, and $\Delta\lambda = 0°$

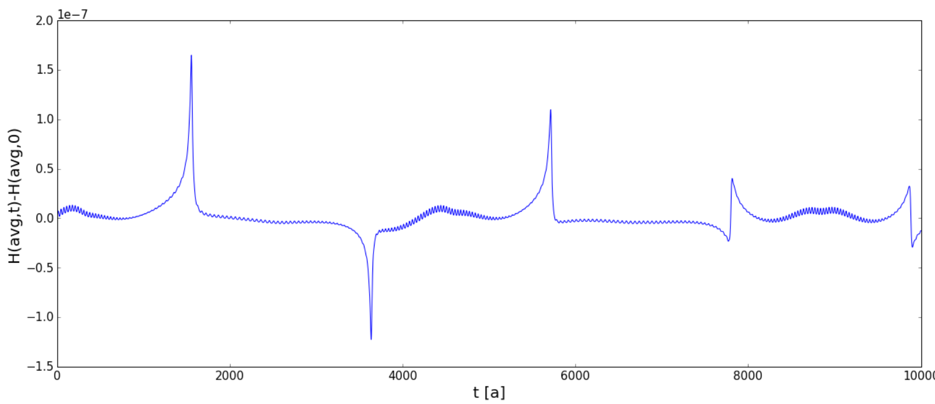

Figure 24: Change of the averaged Hamiltonian from its initial value for the initial conditions $e_p = 0.9$, $e_{a,t=0} = 0.3$, $\Delta\varpi = 180°$, and $\Delta\lambda = 0°$

its absolute value. The secular period is around 2500 years, and the long-term behavior is very consistent.

2.2.3 Non-coplanar configurations

Thus far, only coplanar quasi-satellite configurations ($i_p = i_a = 0°$) were investigated. The goal of this chapter is to analyze quasi-satellite stability when the orbital plane of the planet and the asteroid differ from each other. This general three-dimensional case adds two additional variables with i and Ω, which creates a more complex phase space that is difficult to depict. i_p and Ω_p can be set to $0°$ without loss of generality, by defining the plane of the planet as the ecliptic. There is a general symmetry in the orbital evolution between initial conditions with Ω_a and $\Omega_a + \pi$ under these conditions. $\Delta\varpi$ and $\Delta\lambda$ need to be kept constant for this symmetry to be upheld.

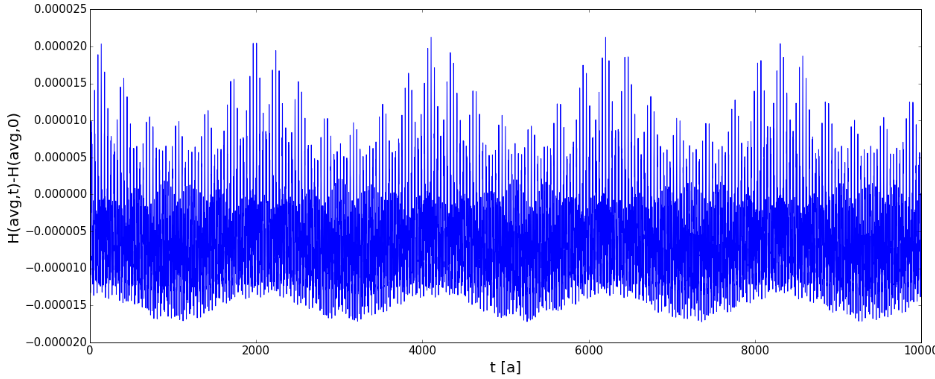

Figure 25: Change of the averaged Hamiltonian from its initial value for the initial conditions $e_p = 0.2$, $e_{a,t=0} = 0.1$, $\Delta\varpi = 180°$, and $\Delta\lambda = 0°$

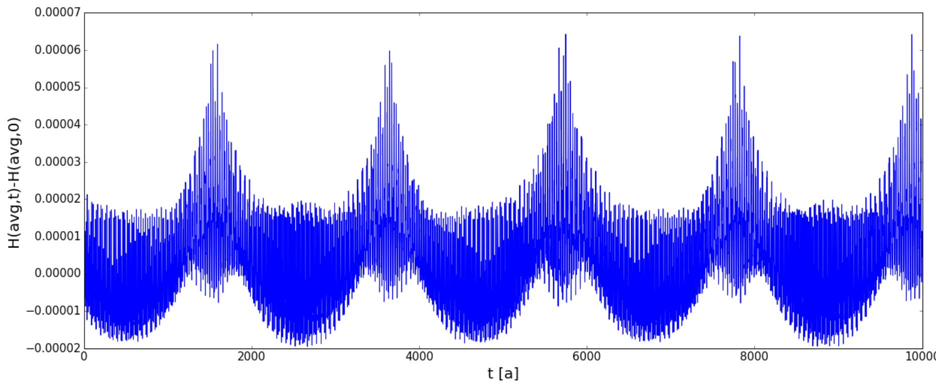

Figure 26: Change of the averaged Hamiltonian from its initial value for the initial conditions $e_p = 0.6$, $e_{a,t=0} = 0.35$, $\Delta\varpi = 0°$, and $\Delta\lambda = 0°$

The calculations were constrained to the case $e_p = 0.5$ for computational reasons. The initial conditions for the non-coplanar calculations are detailed in Table 5. All parameters of the planet were kept constant. The eccentricity of the asteroid was varied in steps of 0.03, and the inclination was varied in steps of 3°. The calculations were performed for four different values of $\Omega_{a,t=0}$, with $\Delta\varpi_{t=0}$ kept at 180° and $\Delta\lambda_{t=0}$ at 0°. This resulted in a total of 7920 massless objects.

The phase space trajectories of massless objects are more complex than in the coplanar simulations, since the phase space has more dimensions. As a result, the objects often require more time to reach unstable regions. The integration time was extended to 30000 years to account for this.

The stability results are shown in Figure 27. The results look similar to the coplanar case for low inclinations. A vertical cut at $e_p = 0.5$ in Figure 14 (coplanar case) can be compared with vertical cuts in Figure 27 at different inclinations.:

- The coplanar case allowed stability for $e_{a,t=0} > 0.2$.

	a[AU]	e	$i[°]$	$\Omega[°]$	$\omega[°]$	$M[°]$	$m[M_\odot]$
Planet	1	0.5	0	0	0	90	0.001
Asteroid	1	0.03,0.06..., 0.99	3,6,...180	45, 90, 135, 180	$180-\Omega$	270	0

Table 5: Initial conditions for the non-coplanar numerical simulations

- The lower stability boundary decreases for some highly inclined orbits. Initial inclinations around $i = 50°$ occasionally lead to resonant orbits below $e_{a,t=0} = 0.1$ for $\Delta\Omega_{t=0} = 180°$.

- The stability regions become significantly smaller for all values of $\Delta\Omega_{t=0}$ at approximately $i_{a,t=0} = 60°$. Arc-like structures at different positions mark trajectories with rapid ejection. These arcs define boundaries of stable regions.

- Objects with $\Delta\Omega_{t=0} = 90°$ become unstable at the lowest inclination, objects with $\Delta\Omega_{t=0} = 180°$ at the highest inclination. There are some retrograde stable objects in this configuration. The large quasi-satellite island extends up to $i_{a,t=0} = 135°$ at high eccentricities.

- Another disconnected island of stability is located around this inclination at lower initial eccentricities. It does only exist for $\Delta\Omega_{t=0} = 180°$.

- There are no connected islands of resonant orbits above inclinations of 140°, although some objects remain in a resonant orbit for a large part if the integration time.

The phase space is complex and it is very challenging to depict the multidimensional orbital evolution of individual objects. Figures 28, 29 and 30 depict the phase spaces $\Delta\lambda - \Delta\varpi$, $\Delta\varpi - e_a$ and $\Delta\Omega - i_a$ for four different values of $i_{a,t=0}$ and $\Delta\Omega_{a,t=0} = 180°$, with different initial eccentricities summarized in each panel. The upper left panels with a moderately high initial inclination of 30° show a principal structure similar to the coplanar case (compare lower right panel of Figure 15 and lower left panel of Figure 17):

- The quasi-satellite stability island centered around $\Delta\lambda = 0°$ and $\Delta\varpi = 180°$ is still tilted counterclockwise in the $\Delta\lambda - \Delta\varpi$ phase space.

- The center is not as well defined as in the coplanar case, and there is no equilibrium point with a non-changing orbit.

- Some of the unstable objects enter trajectories which result in their expulsion from the stability island. They pass through all possible values of $\Delta\lambda$ before leaving the resonance. This usually occurs at high eccentricity.

- The trajectories that different orbits evolve on frequently intersect in the $\Delta\varpi - e_a$-phase space, whereas they are clearly separated in the coplanar case.

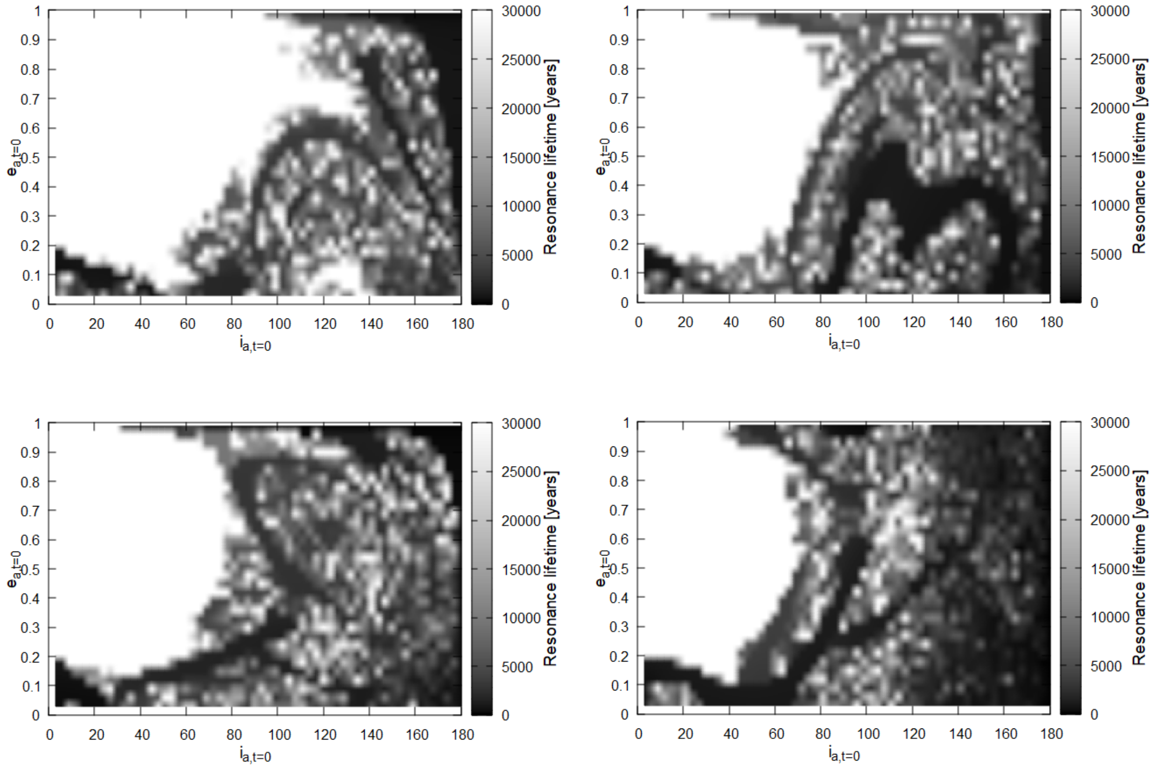

Figure 27: Survival times ($\epsilon < 0.1$) for objects with the initial conditions of Table 5. Individual panels represent $\Delta\Omega_{t=0} = 180°$ (upper left), $\Delta\Omega_{t=0} = 135°$ (upper right), $\Delta\Omega_{t=0} = 90°$ (lower right), and $\Delta\Omega_{t=0} = 45°$ (lower left).

- Some objects reach their highest point in eccentricity not at $\Delta\varpi = 180°$, but at two different values right and left from this point, resulting in a symmetric, heart-shaped trajectory that sometimes has a loop-like structure around $\Delta\varpi = 180°$.

- The quasi-satellites pass through all possible values of $\Delta\Omega$ during their orbit, with their inclination oscillating in a sine-like pattern.

- The maximum inclination is usually reached at $\Delta\Omega = 0, 180°$ and the minimum is at $\Delta\Omega = 90, 270°$. This behavior causes objects started at $\Delta\Omega = 180°$ to remain on resonant trajectories at higher initial inclination than objects started at $\Delta\Omega = 90°$, as seen in the stability maps of Figure 27.

- Some orbits (mostly those with high amplitude in e_a) reach inclinations much higher than their initial values. Stable orbits are possible with maxima up to $100°$ and minima up to $70°$. Objects exceeding those values often have a loop-like evolution at highly retrograde inclinations over $150°$. This behavior is associated with high eccentricity and a $\Delta\lambda$ that precesses through all values.

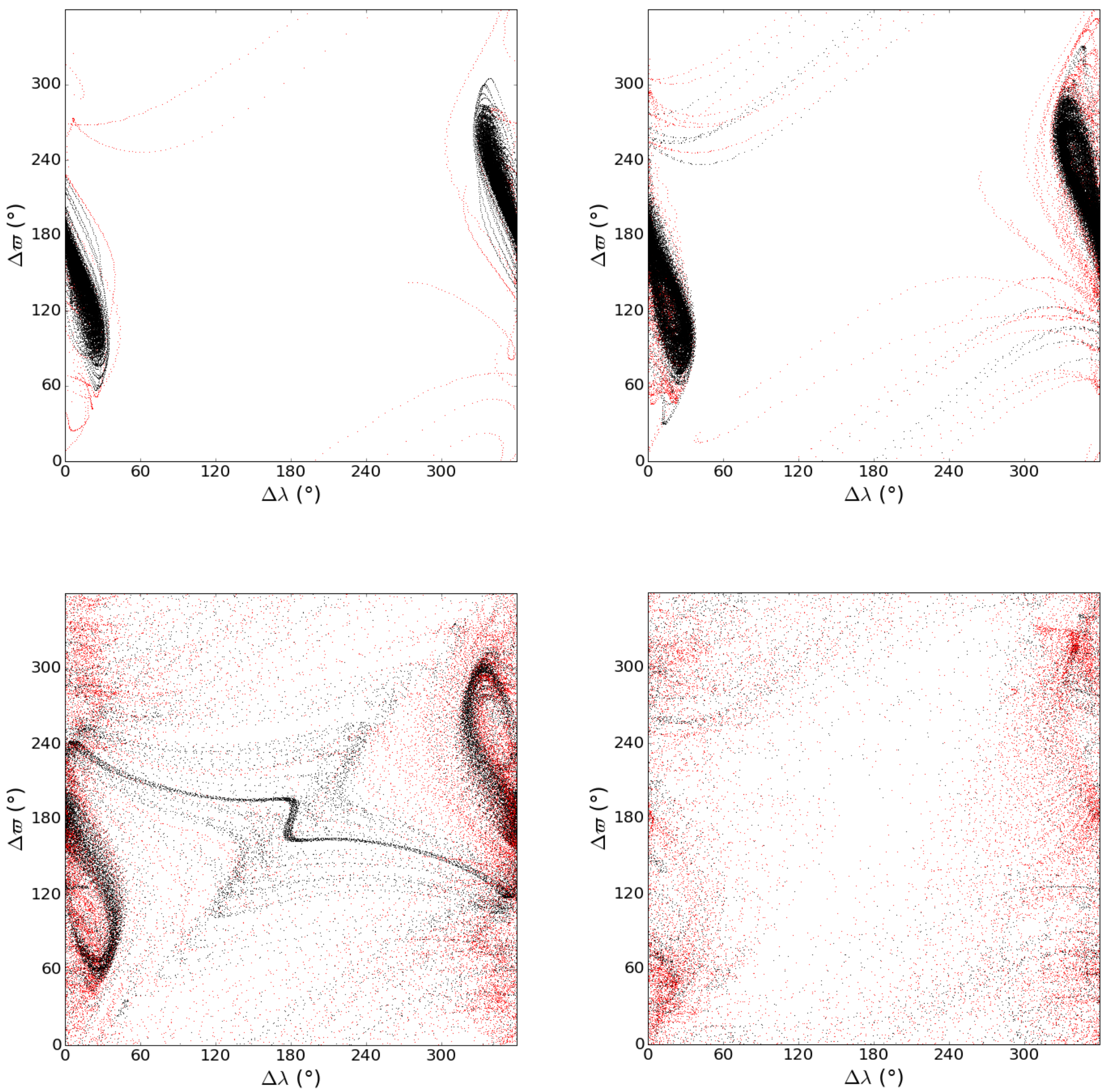

Figure 28: $\Delta\lambda - \Delta\varpi$ phase space of the initial conditions of Table 5. Individual panels represent $\Delta\Omega = 180°$ $i_{a,t=0} = 30°$ (upper left), $i_{a,t=0} = 81°$ (upper right), $i_{a,t=0} = 126°$ (lower left), and $i_{a,t=0} = 168°$ (lower right)

The aforementioned effects are enhanced for objects started in almost perpendicular orbits ($i_{a,t=0} = 81°$, upper right panels of Figures 28-30):

- The quasi-satellite stability island retains same shape, and objects librating around its center have the heart-shaped orbital evolution in the $\Delta\varpi - e_a$-space.

- The center of the stability island is almost empty, with some objects having loop-like structures around $\Delta\varpi = 180°$. This can be interpreted as an overlay of different frequencies, with some governing the evolution in $\Delta\varpi$, and some in $\Delta\Omega$.

- The orbits in this region have their maximum in i_a at $\Delta\Omega = 180°$ around $i_a = 100°$. Interestingly, some of the orbits have a minimum at $\Delta\Omega = 0°$ which is contrary to the symmetric structure observed at low-to-moderate inclination. The opposite behavior, with a maximum at $\Delta\Omega = 0°$ and a minimum at $\Delta\Omega = 180°$, is observed at inclinations around $36° - 63°$ (not depicted in the plots). Since the orbital evolution is symmetric with respect to $(\Delta\Omega, \Delta\Omega + 180°)$, this indicates that these two phenomena depict the same family of orbits, started at a different part of their orbital evolution.

- Another difference between the low-inclination and the almost perpendicular orbits is that in the perpendicular case, leaving the quasi-satellite stability island can lead to a stable orbit. The objects reach all possible values of $\Delta\lambda$ and have a loop-shaped orbital evolution at retrograde inclination and eccentricity. However, the evolution is chaotic, and no closed paths can be observed under these initial conditions. It is not clear if a longer integration time would keep those objects in the resonance.

A very interesting phenomenon emerges at $i_{a,t=0} = 126°$ (lower left panels of Figures 28-30):

- A distinct closed orbit passes through $\Delta\varpi = 180°$ and $\Delta\lambda = 180°$. It marks the center of a family of orbits associated with the separated stability island at low eccentricity in the upper left panel of Figure 27. In this case, the initial eccentricity was 0.12.

- Objects around this point librate around $\Delta\varpi = 180°$, and their $\Delta\lambda$ circles from 0 to 360°. Their highest eccentricity values are reached around $\Delta\lambda = 180°$. This results in a narrow, drop-shaped structure around the fixed point in the $\Delta\varpi - e_a$ phase space.

- The inclination stays in the narrow range between 120° and 140°, with the maxima occurring at $\Delta\Omega = 90, 270°$.

This type of orbit is not a 1-to-1 resonance with the classical resonance angle $\Delta\lambda$, as $\Delta\lambda$ is not bound. Instead, the resonance angle characteristic for this resonance is:

$$\phi_{res} = \Delta\lambda - 2\Delta\varpi + 2\Delta\Omega \tag{44}$$

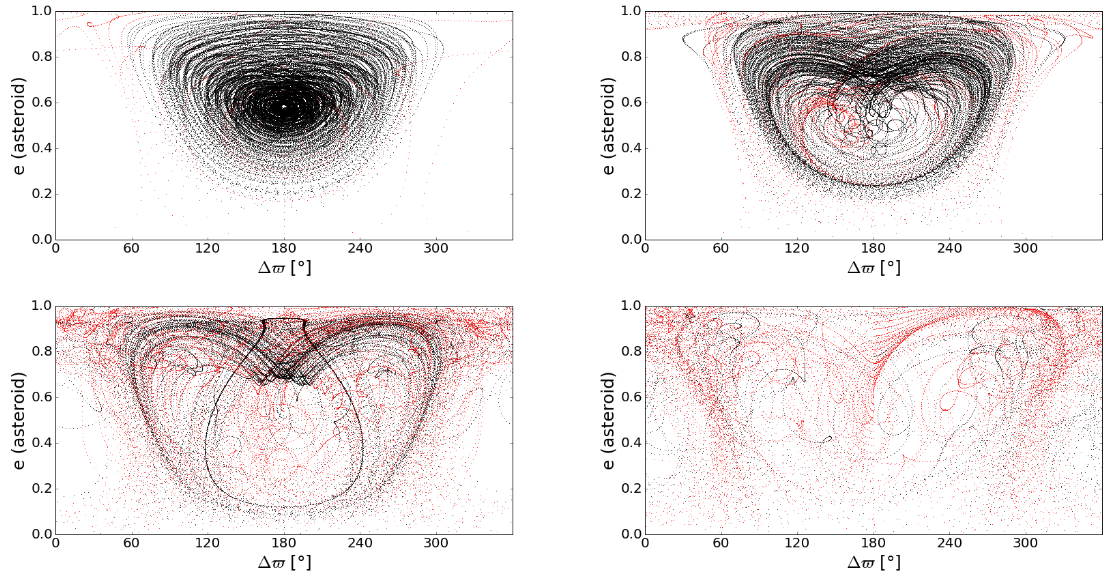

Figure 29: $e_a - \Delta\varpi$ phase space of the initial conditions of Table 5. Individual panels represent $\Delta\Omega = 180°$ $i_{a,t=0} = 30°$ (upper left), $i_{a,t=0} = 81°$ (upper right), $i_{a,t=0} = 126°$ (lower left), and $i_{a,t=0} = 168°$ (lower right),

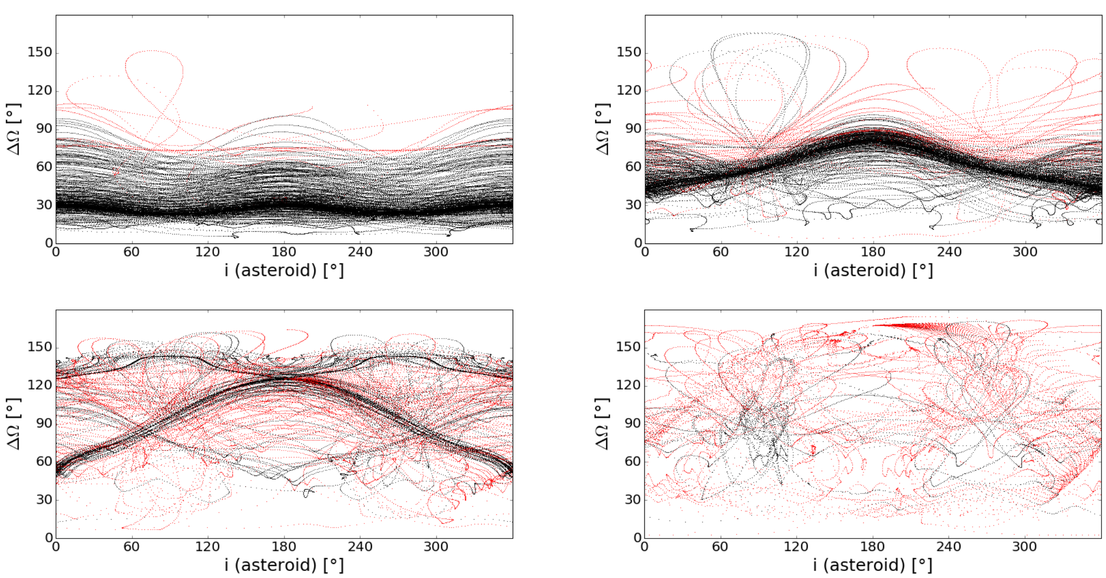

Figure 30: $i_a - \Delta\Omega$ phase space of the initial conditions of Table 5. Individual panels represent $\Delta\Omega = 180°$ $i_{a,t=0} = 30°$ (upper left), $i_{a,t=0} = 81°$ (upper right), $i_{a,t=0} = 126°$ (lower left), and $i_{a,t=0} = 168°$ (lower right)

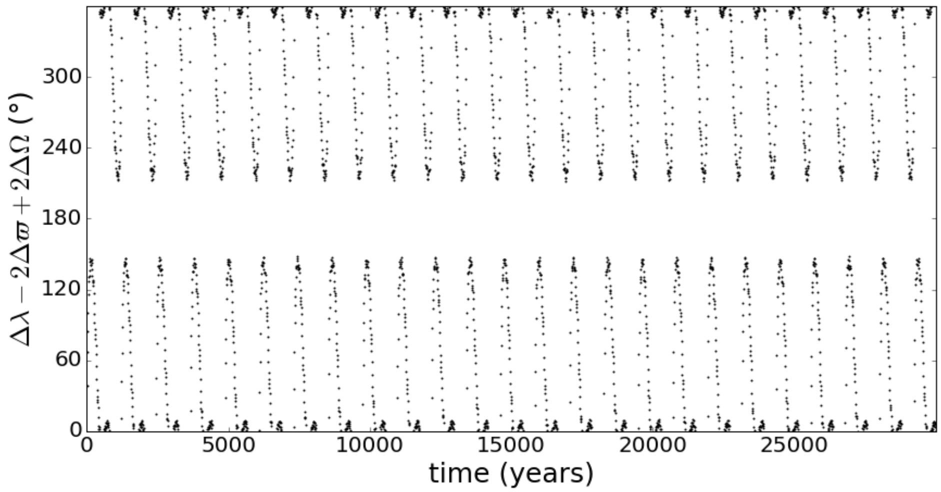

Figure 31: Retrograde resonance angle ϕ_{res} over 30000 years for the orbit with $e_{a,t=0} = 0.12$ and $i_{a,t=0} = 126°$, corresponding to the thick closed line of the lower left panels in the Figures 28-30

This angle was identified as the angle of retrograde coorbital resonance by Morais and Namouni (2013) and numerically confirmed by Morais and Namouni (2016) for circular planetary orbits. Figure 31 shows the time evolution of this angle for the orbit, with $e_{a,t=0} = 0.12$ and $i_{a,t=0} = 126°$. The resonance angle oscillates around 0°. Identifying stable orbits with this resonance angle for other values of e_p would be a worthwhile investigation, but this task goes beyond the scope of this thesis.

The classical quasi-satellites librating around $\Delta\lambda = 0°$ still exist with $i_{a,t=0} = 126°$, with characteristics similar to those described earlier:

- The heart-shaped structure in $\Delta\varpi - e_a$ is more extended, and the objects' amplitude in i_a is higher.
- Most objects have a local minimum in e_a around 0.7 close to $\Delta\varpi = 180°$ and drop below $i_a = 60°$ around $\Delta\Omega = 0°$.
- The highest initial inclination where classical quasi-satellites are recognizable in the phase space is 135°.
- The phase space does not have a discernible structure for inclinations higher than 135° (lower right panels of Figures 28-30). Some orbits can temporarily remain close to the resonance, but it is impossible to make systematic statements about them. One noticeable feature of the phase space is the appearance of clustering around $\Delta\varpi = 60, 300°$, $\Delta\lambda = 20, 340°$. Nonetheless, most objects in this region leave the resonance.

	a[AU]	e	$i[°]$	$\Omega[°]$	$\omega[°]$	$M[°]$	$m[M_\odot]$
Planet	1	0.1,0.6	0	0	0	90	0.001
Asteroid	1	0, 0.03,..., 0.99	0	180	0	270	0

Table 6: Initial conditions for the relativistic numerical simulations

2.2.4 Influence of relativistic effects

The calculations presented in the last chapters are independent of the exact semi-major axis of the planet if only the Newtonian theory of gravity is applied. However, relativistic effects can play an important role if the heliocentric distance is small. General relativity introduces an additional precession frequency to the orbit, which could potentially interfere with the other secular frequencies.

The relativistic integrator introduced by Eggl and Dvorak (2010) uses the full Einstein-Infeld-Hoffmann equations. The barycentric acceleration $\vec{a}_i$ of a body in this framework can be written as:

$$\vec{a}_i = \sum_{j\neq i} \frac{Gm_j \vec{n}_{ji}}{r_{ij}^2} + \frac{1}{c^2} \sum_{j\neq i} \frac{Gm_j \vec{n}_{ji}}{r_{ij}^2} \Bigg(v_i^2 + 2v_j^2 - 4\left(\vec{v}_i \cdot \vec{v}_j\right) - \frac{3}{2}\left(\vec{n}_{ij} \cdot \vec{v}_j\right)^2 - 4\sum_{k\neq i} \frac{Gm_k}{r_{ik}} - \sum_{k\neq j} \frac{Gm_k}{r_{jk}} + \frac{1}{2}\left(\left(\vec{x}_j - \vec{x}_i\right) \cdot \vec{a}_j\right) \Bigg) + \frac{1}{c^2} \sum_{j\neq i} \frac{Gm_j}{r_{ij}^2} \left(\vec{n}_{ij} \cdot \left(4\vec{v}_i - 3\vec{v}_j\right)\right)\left(\vec{v}_i - \vec{v}_j\right) + \frac{7}{2c^2} \sum_{i\neq j} \frac{Gm_j \vec{a}_j}{r_{ij}} + O(c^{-4}) \tag{45}$$

where $\vec{x}_i$, $\vec{v}_i$, and m_i are the barycentric position vectors, velocity vectors and masses of each body, r_{ij} is the coordinate distance between two bodies and, $\vec{n}_{ij}$ is the unit vector from body i to body j. G is the gravitational constant and c is the speed of light. The equation is an approximation of second order in $\frac{1}{c}$. All other terms are at least of fourth order.

To test the influence of relativistic effects in the numerical simulation of quasi-satellites, some of the integrations described in Section 2.2.1 were recalculated with the relativistic integration algorithm. The two planetary eccentricities 0.1 and 0.6 were chosen with coplanar anti-aligned quasi-satellites started in the same positions as in Table 3, albeit with a larger grid step size in e_a, resulting in 34 massless objects for each of the two systems. These conditions are noted in Table 6. The integration time was again set to 10000 years.

Figures 32 and 33 show the difference of the Newtonian calculations of Section 2.2.1 and the relativistic calculations for the orbital elements e_a and $\Delta\varpi$. The difference is expressed with:

$$\delta e = e_a(rel.) - e_a(newt.) \tag{46}$$

$$\delta\varpi = \Delta\varpi(rel.) - \Delta\varpi(newt.) \tag{47}$$

The phase space looks identical to the non-relativistic phase space if just the orbital elements themselves are plotted (top right panel of Figure 15 and top left panel of Figure 16, respectively). Due to relativistic effects, the longitude of perihelion of the massive planet changes by 0.09° for the $e_p = 0.1$ case and by 0.16° for the $e_p = 0.6$ case over the course of the integration time.

- In the $e_p = 0.1$ case, there is a difference between the objects where $\Delta\varpi$ librates around 180° (high initial eccentricity) and the objects where $\Delta\varpi$ precesses through all possible values of $\Delta\varpi$ (low initial eccentricity). Relativistic effects have a higher influence on the librating objects (Figure 32). They reach much higher eccentricities and thus lower perihelion distances at regions where these effects become significant.

- The value of δe of the precessing objects oscillates with periods identical to the respective secular period of the quasi-satellite. The amplitude of the oscillations increases linearly with time and reaches 0.001 at the end of the integration time for the object with the highest amplitude. The oscillation is centered around 0, which results in the mean value of e_a over a sufficient period of time remaining the same for relativistic and non-relativistic calculations.

- The oscillations in $\delta\varpi$ occur with the same period as the δe-oscillations, but there is a shift in the positive direction for the mean value of $\delta\varpi$. It totals approximately 0.5° over the integration time for the object with the highest maximal eccentricity.

- Both δe and $\delta\varpi$ are larger for the librating objects.

- δe can reach 0.006, even though the mean value over an extended period remains constant. The shape of the δe curve varies significantly across objects, with triangular and pulse-like curves showing up at the highest amplitudes. As the libration periods for objects in this region are longer than for precessing objects, only a few periods are completed during the integration time.

- The relativistic perihelion precession can exceed 5° in $\delta\varpi$, with the amplitude of its mean value again increasing linearly over time.

- The general trend of the perihelion shift to positive values of the precessing objects is not present for all objects. Some have their most extreme shifts to negative values.

All objects in the $e_p = 0.6$ case (phase space depicted in the upper left panel of Figure 16) librate around $\Delta\varpi = 180°$. These objects were divided at an arbitrary cutoff point into objects near and far from the fixed point (at around $e_a = 0.55$) in Figure 33 for visibility reasons.

- The objects far from the fixed point reach lower perihelion values, which causes the relativistic effects to play a more significant role. δe oscillates with the secular period (compare Figure 18) and its amplitude linearly increases over time.

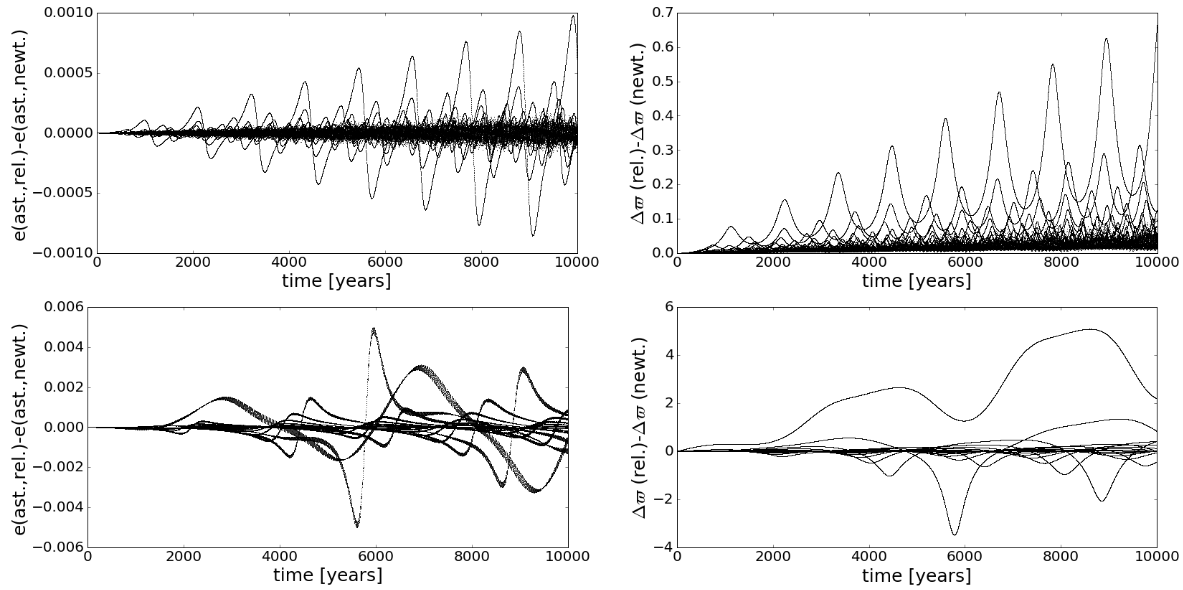

Figure 32: Deviations of e_a (left column) and $\Delta\varpi$ (right column) for $e_p = 0.1$ for stable objects and the initial conditions of Table 6. Objects with precessing $\Delta\varpi$ ($e_{a,t=0} \leq 0.54$) are in the top row, obects with $\Delta\varpi$ librating around 180° ($e_{a,t=0} \geq 0.57$) are in the bottom row.

- The mean value of δe remains at 0. The difference oscillates in an only slightly asymmetric sine curve for objects close to the fixed point. This shape develops into a pulse-like behavior for the highest e_a values. The maximal amplitude reaches 0.08 for the most extreme objects, but stays under 0.0001 for objects closest to the fixed point.
- The evolution of $\delta\varpi$ is similar. It oscillates asymmetrically, with the extreme values in the negative direction attaining much higher absolute values. The amplitude increases linearly over time.
- $\Delta\varpi$ of the most extreme objects can differ up to over 40° at a certain point in time, although it remains under 5° for most of the time.
- It is difficult to determine the general shifting of the mean value due to its asymmetric shape, but it appears to remain constant, unlike the mean value of $\delta\varpi$ of the precessing objects.

2.2.5 Lyapunov characteristic exponents

The Lyapunov Characteristic Exponent (LCE) is a rigorous measurement of chaos in celestial dynamics. It describes the rate of separation between infinitesimally close trajectories in time evolution. A system is considered chaotic if this separation grows

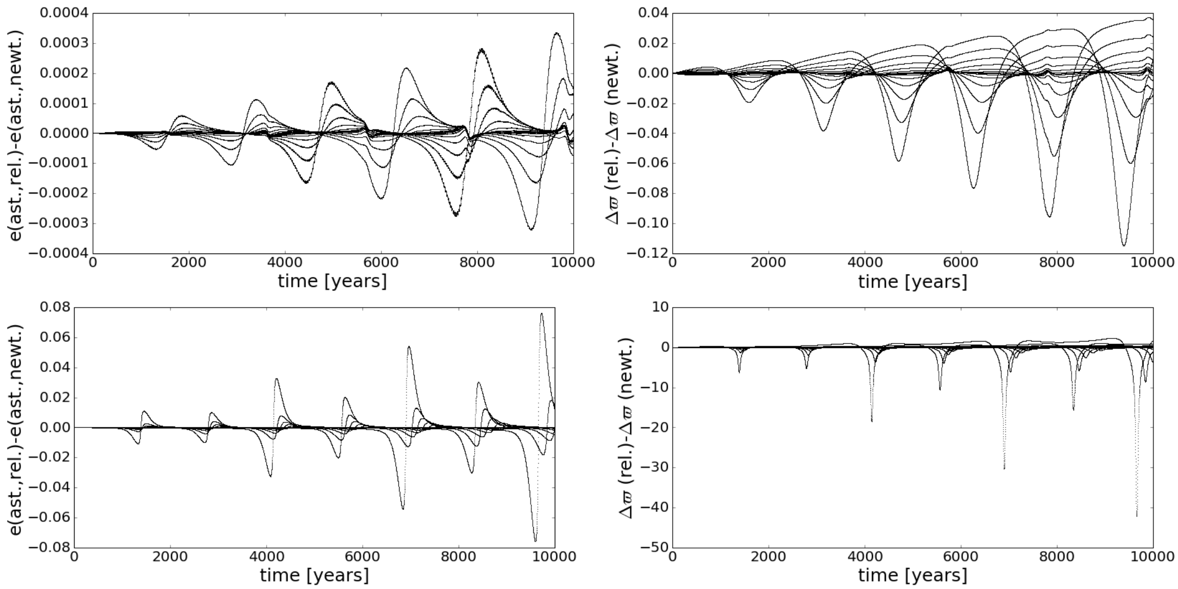

Figure 33: Deviations of e_a (left column) and $\Delta\varpi$ (right column) for $e_p = 0.6$ for stable objects and the initial conditions of Table 6. Objects close to the fixed point $\Delta\varpi$ ($0.36 \leq e_{a,t=0} \leq 0.75$) are in the top row, obects circling far from it ($e_{a,t=0} \leq 0.33$; $e_{a,t=0} \geq 0.78$) are in the bottom row.

exponentially. For autonomous Hamiltonian systems, the Lyapuonv exponents can be calculated with a procedure described by Skokos (2010). An arbitrary unit vector $\vec{w}$ is defined, that has the same number of dimensions as the Hamiltonian. This number is usually two times the number of spatial dimensions N. $\vec{w}$ is evolved with the help of the variational equations. The differential equation for the time evolution of $\vec{w}$ is:

$$\dot{\vec{w}} = \left[J_{2N} \cdot D^2 H(x(t))\right] \cdot w \tag{48}$$

$D^2H(x(t))$ (abbreviated as $\hat{\mathbf{H}}$ in later equations) is the Hessian matrix of the Hamiltonian function:

$$D^2 H(x(t))_{i,j} = \frac{\partial^2 H}{\partial x_i \partial x_j} \tag{49}$$

The matrix J_{2N} is defined as:

$$J_{2N} = \begin{bmatrix} 0_N & I_N \\ -I_N & 0_N \end{bmatrix} \tag{50}$$

The variational equations are integrated along with the equations of motion. The evolution of the length of $\vec{w}$ with these equations is measured with each time step and denoted α. $\vec{w}$ is re-normalized after every time step in most applications. The histogram of the α values (also called the Local Lyapunov Exponents) can already provide information about chaos and stability. The collection of α values for each time step can be used to calculate the LCE up to time τ with the following formula:

$$LCE = \frac{1}{\tau} \sum_{t=0}^{\tau} \ln \alpha_t \tag{51}$$

A LCE curve approaching a finite value at the end of the calculation indicates a chaotic trajectory. If the LCE approaches 0, the trajectory is regular.

This procedure was applied to the Hamiltonian of a n-body system in three dimensions (compare Equation 2). In this case, the vector $\vec{w}$ has six dimensions. The Hessian matrix $\hat{\mathbf{H}}$ of this Hamiltonian can be calculated with respect to every body in the system. The matrix has four blocks:

$$\hat{\mathbf{H}} = \begin{bmatrix} \mathbf{H}_x & \mathbf{0}_3 \\ \mathbf{0}_3 & \mathbf{H}_v \end{bmatrix} \tag{52}$$

The upper left block contains the purely spatial derivatives, and the lower right block contains the derivatives with respect to the velocities. The other blocks represent the mixed terms, which are all 0.

The diagonal arguments of the spatial component can be written as (for the body with index p):

$$\begin{aligned} \mathbf{H}_{x,k,k} = \sum_{j=1, j\neq p}^{N} G m_p m_j \Bigg(& \frac{-3(x_{j,k} - x_{p,k})^2}{((x_{j,1} - x_{p,1})^2 + (x_{j,2} - x_{p,2})^2 + (x_{j,3} - x_{p,3})^2)^{5/2}} + \\ & \frac{1}{((x_{j,1} - x_{p,1})^2 + (x_{j,2} - x_{p,2})^2 + (x_{j,3} - x_{p,3})^2)^{3/2}} \Bigg) \end{aligned} \tag{53}$$

The non-diagonal arguments of the spatial component are:

$$\mathbf{H}_{x,m,n} = \sum_{j=1, j\neq p}^{N} G m_p m_j \left(\frac{-3(x_{j,m} - x_{p,m})(x_{j,n} - x_{p,n})}{((x_{j,1} - x_{p,1})^2 + (x_{j,2} - x_{p,2})^2 + (x_{j,3} - x_{p,3})^2)^{5/2}} \right) \tag{54}$$

The velocity component of $\hat{\mathbf{H}}$ can be written as:

$$\mathbf{H}_{v,} = \mathbf{1}/m_p \tag{55}$$

This approach to LCE calculation can be implemented into every integration algorithm. In this work, the procedure was separated from the actual integration and the LCEs were calculated using only the end results. Only the cartesian coordinates at every time step were necessary for the computation of the Hessian matrix. The variational equations were integrated with the second-order Heun method with time step Δt. The time derivatives of $\vec{w}$ were computed according to Equation 48):

$$\vec{w}_1' = \vec{w}_0 + \Delta t \cdot \dot{\vec{w}}_0 \tag{56}$$

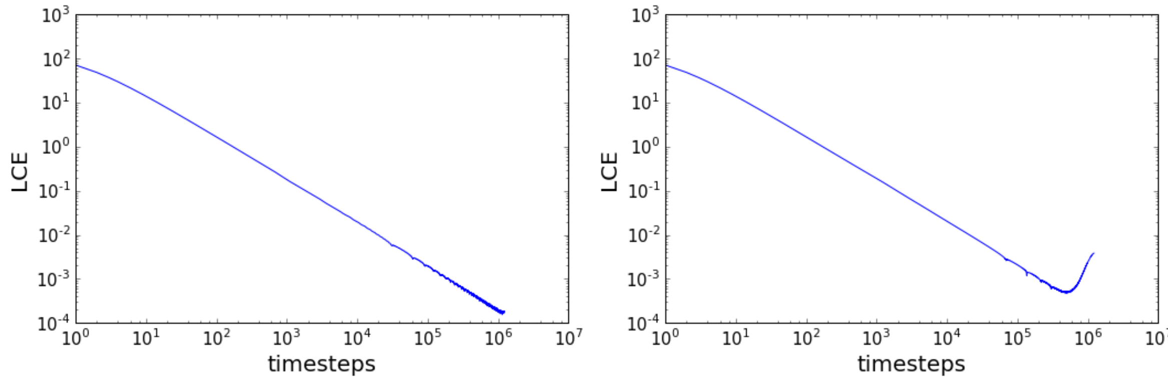

Figure 34: Evolution of the Lyapunov Characteristic Exponents of two quasi-satellite asteroids $\Delta\lambda_{t=0} = 0°$ at $e_p = 0.5$. Left panel: $e_{a,t=0} = 0.4$, $i_a = 0°$, and $\Delta\varpi_{t=0} = 180°$. Right panel: $e_{a,t=0} = 0.12$, $i_{a,t=0} = 153°$, $\Delta\Omega_{t=0} = 180°$, and $\Delta\varpi_{t=0} = 180°$.

$$\vec{w}_1 = \frac{1}{2} \cdot \vec{w}_0 + \frac{1}{2} \cdot \left(\vec{w}_1' + \Delta t \cdot \dot{\vec{w}}_1' \right) \tag{57}$$

It was not possible to use methods of higher order, since the the Hessian matrix of the Hamiltonian could only be computed at discrete time steps, determined by the output interval of the integrator. For this reason, it was necessary to choose a sufficiently small time step in the output files to obtain the correct convergent results.

The implementation of the algorithm is explained in the appendix. See Kraut (2018) for more details on the theory and an application lf the method on the Henon-Heiles-System

Two orbits in different domains of the phase space were analyzed to test the applications of LCEs on the orbital evolution of quasi-satellites. An output interval of 0.1 days was used. Only 500 years of integration could be executed with this setup for computational reasons.

The two quasi-satellite orbits studied with this technique were placed in a system with $e_p = 0.5$. One co-planar anti-aligned object ($\Delta\varpi_{t=0} = 180°$, $e_{a,t=0} = 0.4$, $i_a = 0°$) represents a closed orbit close to the fixed point. One retrograde object ($e_{a,t=0} = 0.12$, $i_{a,t=0} = 153°$, $\Delta\Omega_{t=0} = 180°$, $\Delta\varpi_{t=0} = 180°$) is an example of the chaotic retrograde population. The orbital evolution can be seen in the lower right panel of Figure 15 and the lower right panels of Figure 28-30. The latter object has a resonance lifetime of 3860 years.

Figure 34 shows the behavior of the LCE for the two cases. The object on the closed orbit has a decreasing LCE for the whole integration time. At the end of the integration, the LCE has a value of approximately 0.00016. The LCE of the chaotic object also decreases at the beginning. After 200 years, it starts to increase again and reaches a value of 0.003 at the end of the integration. This behavior of the LCEs is not typical. A more thorough analysis would be necessary to see how the quasi-satellite resonance can be described in the context of LCEs.

3 Application to existing planet systems

3.1 Quasi-satellites in the solar system

In the solar system, quasi-satellites are only a small part of the coorbital population of the terrestrial and giant planets. Quasi-satellites are not stable for extended periods of time, due to low planetary eccentricities and multi-planet interactions (Wiegert, Innanen, and Mikkola, 2000). Trojan asteroids are far more common. Temporary quasi-satellites have been observed for Earth and other planets. Quasi-satellites are believed to be one of the most common types of companion objects for the proposed Planet Nine (Batygin and Morbidelli, 2017).

Coorbital objects of any kind are uncommon for the terrestrial planets. The first object in a confirmed 1-to-1 mean motion resonance with Earth was (3753) Cruithne, previously known as 1986 TO, whose coorbital nature was discovered by Wiegert, Innanen, and Mikkola (1997) and further investigated in Wiegert, Innanen, and Mikkola (1998). The asteroid was described as being in a complex horseshoe orbit, encompassing the three Lagrange points L_3, L_4, and L_5. Cruithne's eccentricity of 0.515 causes it to cross the orbits of Venus and Mars, where it experiences close encounters with those perturbers. A compound orbit, which allows transitions between horseshoe and quasi-satellite orbits, is thought to be possible for Cruithne in the future. Similar behavior was found for the asteroids (3262) Khufu, 1989 VA, 1993 WD (since named (10563) Izhdubar), and 1994 TF2. 1989 VA is close to coorbital resonance with Venus, while the other three asteroids are close to coorbital resonance with Earth. While the objects are not quasi-satellites at present time and, with the exception of (3753) Cruithne, non-coorbital, (3753) Cruithne and (3262) Khufu have the potential to be captured in quasi-satellite orbits in the future (Namouni, Christou, and Murray, 1999).

Connors et al. (2002) found that the horseshoe-bound asteroid 2002 AA29 will transition into a quasi-satellite orbit around the year 2600. The asteroids 2000 PH5 (since named (54509) YORP) and 2001 GO2 were also found to be in a coorbital resonance (Wiegert et al., 2002). The first asteroid found to be in a quasi-satellite orbit at time of discovery was 2003 YN107. It was in a quasi-satellite resonance between 1997 and 2006, when it reverted back into a horseshoe orbit (Connors et al., 2004). Two additional quasi-satellites of Earth were described by Wajer (2010). 2004 GU9 and 2006 FV35 were predicted to stay in the quasi-satellite orbit for the next few hundred years. Three additional quasi-satellites (2013 LX28, 2014 OL339, and 2016 HO3) were recently discovered by Connors (2014), de la Fuente Marcos and de la Fuente Marcos (2014b), and de la Fuente Marcos and de la Fuente Marcos, 2016a. 2015 SO2 is another asteroid presently in a horseshoe orbit, that will transition into a quasi-satellite in the future (de la Fuente Marcos and de la Fuente Marcos, 2016b). The asteroid 2017 TZ2 left its quasi-satellite orbit in March 2017, due to a close encounter with Earth. It was hypothesized that it shared a common origin with (54509) YORP (de la Fuente Marcos and de la Fuente Marcos, 2017). The first Trojan asteroid of Earth (2010 TK7) was discovered in 2011 by the infrared telescope WISE (Connors, Wiegert, and Veillet, 2011). The dynamical behavior of 2010 TK7 and possible stability regions of Trojan asteroids of Earth were studied by Dvorak, Lhotka, and Zhou (2012).

Other planets in the solar system also have quasi-satellites. Quasi-satellites of Venus are 2002 VE68 (Mikkola et al., 2004), 2012 XE133 (de la Fuente Marcos and de la Fuente Marcos, 2013), 2013 ND15 (de la Fuente Marcos and de la Fuente Marcos, 2014a), and possibly 2015NZ12 (de la Fuente Marcos and de la Fuente Marcos, 2017). 2001 CK32 is an example of a horseshoe asteroid of Venus (Brasser et al., 2004).

The timescales for which quasi-satellites can be stable are much longer for the giant planets. A total of five quasi-satellites of Jupiter, two of which were classified as comets, were found by Kinoshita and Nakai (2007) and Wajer and Królikowska (2012). (15504) 1999 RG33 is Saturn's one temporary quasi-satellite (Gallardo, 2006). Neptune was found to have a quasi-satellite stable for several thousand years with 2007 RW10 (de la Fuente Marcos and de la Fuente Marcos, 2012).

The osculating orbital elements for all currently known quasi-satellites, horseshoe asteroids, and Trojan Asteroids of the inner three planets are displayed in Table 7 as published by the Minor Planet Center.

3.2 Capture of coorbital asteroids

The capture of coorbital asteroids has been discussed extensively in the literature. The capture of Jupiter Trojans and the outer irregular satellites of the giant planets were the main issues addressed in the context of the solar system. A Trojan capture mechanism was discussed in the framework of the Nice model (Tsiganis et al., 2005), in which Jupiter and Saturn experience an instability after a 2:1 mean-motion resonance in the early stages of the system's evolution. Morbidelli et al. (2005) found that there are two phases during the instability where, given a constant influx of minor bodies, Trojan asteroids can be captured with an efficiency between $2 \cdot 10^{-6}$ and $2 \cdot 10^{-5}$, depending on the migration rate of the planets. This leads to a Trojan population that has an orbital distribution and total mass similar to the one observed in our solar system.

Similar results were found by Marzari and Scholl (2007) and Lykawka and Horner (2010), who concluded that capture rates for the other gas giants were similar to the rate of Jupiter. Again, the parameters of the planetary migration were the deciding factors in the chaotic capture, which occurs during the crossing of mean-motion resonances.

Horner, Koch, and Sofia Lykawka (2013) proposed a smoother migration scenario with a sizable capture efficiency of Jupiter Trojans. Schwarz and Dvorak (2012) investigated Trojan capture in the inner solar system. They concluded that there is a high capture probability, but the resulting orbits are only stable for short periods.

Few studies have investigated the capture of quasi-satellites, especially for eccentric planets. Kortenkamp (2005) discussed a capture mechanism for retrograde irregular satellites of giant planets, which involves them first being trapped in a quasi-satellite orbit ($e_p = 0.1$ was used). Kortenkamp and Joseph (2011) discussed the transition from Trojan planets to quasi-satellites in a migrating gas-giant framework, showing that this phenomenon can occur under these conditions until very late in the migration.

Name	a [AU]	e	i [°]	Ω [°]	ω [°]	M [°]	Type	Ref.
Venus								
(322756) 2001 CK32	0.725	0.383	8.1	109.4	234.1	34.5	H	MPO 408323
2002 VE65	0.724	0.41	9.0	231.6	355.4	165.2	Q	MPO 357115
2012 XE133	0.723	0.433	6.7	281.1	337.1	35.7	H	MPO 252145
2013 ND15	0.724	0.611	4.8	95.8	19.7	39.6	T (L4)	MPO 268510
2015 WZ12	0.722	0.512	3.6	251.7	345.8	117.5	H	MPO 386948
Earth								
(3753) Cruithne	0.998	0.515	19.8	126.2	43.8	95.3	H	MPO 421667
(54509) YORP	1.006	0.230	1.6	278.3	278.9	274.9	H	MPO 212232
(85770) 1998 UP1	0.998	0.345	33.2	18.4	234.2	264.5	H	MPO 439616
(164207) 2004 GU9	1.001	0.136	13.7	38.6	280.1	222.1	Q	MPO 433051
(277810) 2006 FV35	1.001	0.378	4.1	179.5	170.8	202.6	Q	MPO 440345
(419624) 2010 SO16	1.003	0.075	14.5	40.4	109.0	9.6	H	MPO 392086
(469219) 2016 HO3	1.001	0.104	7.8	66.4	306.8	168.4	Q	MPO 419283
2001 GO2	1.007	0.168	4.6	193.5	265.5	6.3	H	MPO 30455
2002 AA29	0.993	0.013	10.7	106.4	101.7	27.8	H	MPO 57849
2003 YN107	0.989	0.014	4.3	264.4	87.8	258.8	H	MPO 77762
2010 TK7	0.999	0.19	20.9	96.5	45.9	63.1	T (L4)	MPO 423755
2013 BS45	0.992	0.084	0.8	83.4	150.7	335.7	H	MPO 307057
2013 LX28	1.002	0.452	50	76.7	345.8	128.1	Q	MPO 411550
2014 OL339	0.999	0.461	10.2	252.2	289.7	319.7	Q	MPO 392451
2015 SO2	0.996	0.109	9.2	182.8	291.2	81.2	H	MPO 419528
2017 DR109	1.005	0.241	3.1	341.1	73.4	98.8	H	MPO 399984
Jupiter								
(363135) 2001 QQ199	5.329	0.428	42.5	213	193.6	113.8	Q	MPO 408573
2004 AE9	5.089	0.646	1.7	188.7	285.7	84.6	Q	MPO 62469
2007 GH7	5.280	0.464	25.6	79.1	97.7	336.0	Q	MPO434920
295P/LINEAR	5.311	0.616	21.1	7.6	73.0	115.7	Q	MPC 93589
329P/LINEAR-Catalina	5.198	0.679	21.6	87.8	343.5	72.0	Q	MPC 101101
Saturn								
(15504) 1999 RG33	9.390	0.773	34.9	23.7	273.6	246.5	Q	MPO 8365
Neptune								
(309239) 2007 RW10	30.179	0.302	36.2	187.1	95.6	71.5	Q	MPO 418606

Table 7: Coorbital asteroids in the solar system (no Trojans for planets outward from Earth), orbital elements at Epoch 20180328 or 20180423 from the MPC (*Lists and Plots: Minor Planets*)

The quasi-satellites remain stable through planetary migration. Their resonance angle varies with secondary effects from other planets, but that is usually insufficient to perturb them from the resonance. Escape can occur when the eccentricity of a planet decreases, and the low-eccentricity quasi-satellites are no longer stable. Morais and Namouni (2016) found that retrograde capture is more efficient than prograde capture for asteroids migrating inwards towards a circular planet. There are still many open questions regarding capture of quasi-satellites. A study on this is reserved for a future publication.

3.3 Sample of known extrasolar planet systems

The discovery of multiple extrasolar planet systems within the last 22 years has confirmed the existence of star systems with planetary architectures very different from our own. In particular, systems with highly eccentric massive planets are common. Systems with more than one eccentric planet also were found. The existence of different asteroid families in systems such as this is a very interesting possibility. Quasi-satellite orbits are one possibility for such an asteroid family.

It should be noted that the discovery of extrasolar asteroids is not possible with current observational methods. Methods like the radial velocity method can be applied only if the mass of the asteroid is significant. The radial velocity signal of two planets of similar mass in a quasi-satellite resonance is very difficult to distinguish from that of a single planet (Giuppone, Benítez-Llambay, and Beaugé, 2012). Leleu, Robutel, and Correia (2015) showed that the signal of two coorbital tadpole or horseshoe planet orbits could be detected by observing long-term modulations. It can be expected that the same is true for quasi-satellites.

Several studies have investigated the stability of coorbital configurations in individual planetary systems, including Schwarz et al. (2009) for Trojan asteroids. No similar studies have been published for quasi-satellites. In the next section, the stability of quasi-satellite resonance in known multi-planetary systems is numerically explored.

The exploration begins by presenting the currently known sample of extrasolar planets. As of December 29th, 2017, the database `exoplanet.eu` contains 3726 extrasolar planets with well-determined orbits. Many were detected via the transit method, which does not provide reliable eccentricity values. As a result, only about 20% the planets are suitable for analysis of eccentricity distribution. Planets detected with the radial velocity method usually have estimates for the planetary eccentricity. The database contains 741 planets detected with this method, of which 713 have published values for both semi-major axis and eccentricity. Figure 35 shows a simple a-e-plot of these planets. It becomes apparent immediately that a wide range of eccentricities is represented. Massive planets are likely over-represented in the sample, because the detection bias for the radial velocity method is skewed towards high masses. Nonetheless, their distribution shows that massive planets (especially around 1 AU) with moderate eccentricities are abundant.

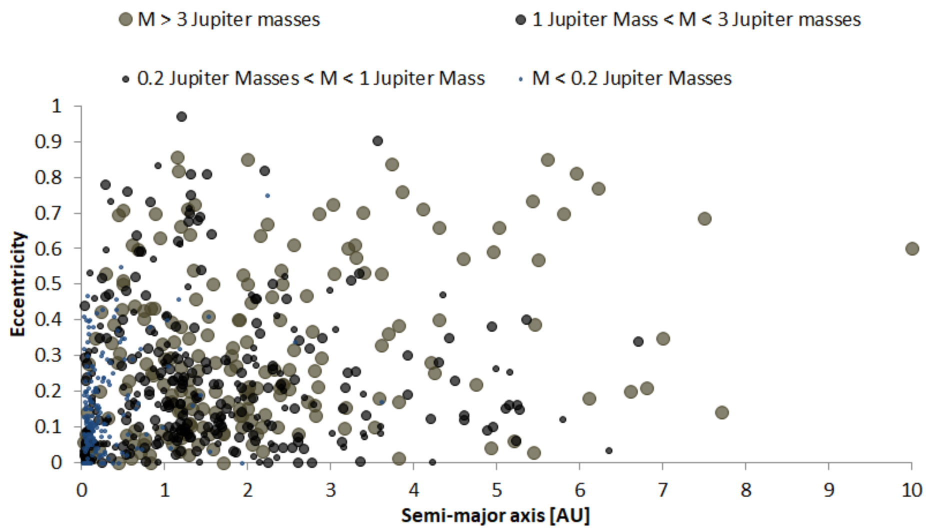

Figure 35: a-e-diagram for planets discovered with the radial velocity method in the `exoplanet.eu` database

In Section 2 it was shown that quasi-satellite resonances are possible for planets with all eccentricities in a Three-Body Problem. The coplanar stability regions were determined for systems with only one planet (compare figure 14) in chapters 2.1 and 2.2.1.

The question of stability for quasi-satellites becomes more complicated for systems with more than one planet. The selection of two systems for which numerical calculations were performed is described in this section. There are 94 two-planet systems, 24 three-planet systems, seven four-planet systems, four five planet-systems, and four six-planet systems in the database. The next section only focuses on two-planet systems. Only systems with a published value for the errors of $m \sin i$, a, and e were taken into consideration. The error for the eccentricity was constrained to be smaller than the eccentricity itself, and the error of the projected mass was constrained to less than half of its value. Systems where the ratio between the two semi-major axes is larger than 5 were discarded to focus on systems with significant two-planet interactions. Systems where at least one of the planets lay inside of 0.2 AU were excluded to avoid relativistic effects. 18 systems remained after the elimination of systems that did not fit the criteria. Table 8 shows the key orbital parameters of these systems (from `exoplanet.eu`). The parameters used later in this work are from individual publications and may differ slightly. Some of the systems lie close to a mean motion resonance (indicated in the Table 8). Figure 36 plots semi-major axes and eccentricities of the 18 systems, connecting planets which belong to the same system. The outer planet has a higher reported eccentricity in 10 of the 18 systems.

Planet	$m\,sin\,i$ $[M_{jup}]$	$a[AU]$	e	MMR	Reference
GJ 785 b	0.0532	0.32	0.13	-	Howard et al. (2011),Pepe et al. (2011)
GJ 785 c	0.076	1.18	0.32	-	Pepe et al. (2011)
HD102272 b	5.9	0.614	0.05	4:1	Niedzielski et al. (2009)
HD102272 c	2.6	1.57	0.68	4:1	Niedzielski et al. (2009)
HD 108874 b	1.36	1.051	0.07	4:1	Butler et al. (2003)
HD 108874 c	1.018	2.68	0.25	4:1	Vogt et al. (2005)
HD 110014 c	3.1	0.64	0.44	-	de Medeiros et al. (2009)
HD 110014 b	10.7	2.31	0.26	-	Soto, Jenkins, and Jones (2015)
HD 113538 b	0.36	1.24	0.14	-	Moutou et al. (2011)
HD 113538 c	0.93	2.44	0.2	-	Moutou et al. (2011)
HD 128311 b	2.18	1.099	0.25	2:1	Butler et al. (2003)
HD 128311 c	4.19	1.76	0.17	2:1	Vogt et al. (2005)
HD 133131 A b	1.43	1.44	0.32	-	Teske et al. (2016)
HD 133131 A c	0.48	4.36	0.47	-	Teske et al. (2016)
HD 147873 b	5.14	0.522	0.207	-	Jenkins et al. (2017)
HD 147873 c	2.3	1.36	0.23	-	Jenkins et al. (2017)
HD 154857 b	2.24	1.291	0.46	-	McCarthy et al. (2004)
HD 154857 c	2.58	5.36	0.06	-	Wittenmyer et al. (2014b)
HD 155358 b	0.85	0.64	0.17	2:1	Cochran, Endl, and Wittenmyer (2007)
HD 155358 c	0.82	1.02	0.16	2:1	Cochran, Endl, and Wittenmyer (2007)
HD 183263 b	3.67	1.51	0.357	5:1	Wright et al. (2009)
HD 183263 c	3.82	4.25	0.253	5:1	Wright et al. (2009)
HD 30177 b	8.07	3.58	0.18	-	Tinney et al. (2003)
HD 30177 c	3	6.99	0.35	-	Wittenmyer et al. (2017)
HD 33844 b	1.96	1.6	0.15	5:3	Wittenmyer et al. (2016)
HD 33844 c	1.75	2.24	0.13	5:3	Wittenmyer et al. (2016)
HD 4732 b	2.37	1.19	0.13	-	Sato et al. (2013)
HD 4732 c	2.37	4.6	0.23	-	Sato et al. (2013)
HD 47366 b	1.75	1.214	0.089	-	Sato et al. (2016)
HD 47366 c	1.86	1.853	0.278	-	Sato et al. (2016)
HD 73526 b	2.25	0.65	0.29	2:1	Tinney et al. (2003)
HD 73526 c	2.25	1.03	0.28	2:1	Tinney et al. (2006)
HD 7449 b	1.11	2.3	0.82	-	Dumusque et al. (2011)
HD 7449 c	2	4.96	0.53	-	Dumusque et al. (2011)
TYC+1422-614-1 b	2.51	0.6879	0.07	-	Niedzielski et al. (2015)
TYC+1422-614-1 c	10	1.3916	0.049	-	Niedzielski et al. (2015)

Table 8: Masses and orbital parameters from `exoplanet.eu` for the 18 candidate systems

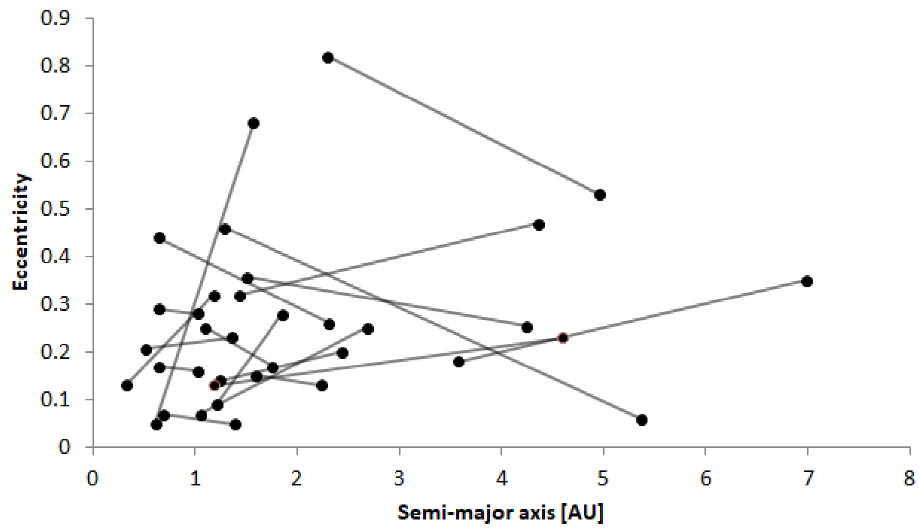

Figure 36: a-e-diagram for the 18 two-planet systems considered in this work with data taken from `exoplanet.eu`

3.4 Stability analysis of quasi-satellites in multi-planet systems

Only some of the 18 systems identified in the last chapter have published orbital stability analysis beyond what is stated in the respective discovery paper (noted in Table 8). Antoniadou and Voyatzis (2016) presented extensive stability maps for the systems HD 7449 and HD 102272. Some analysis was conducted for the systems HD 108874, HD 128311, and HD 73526 by Antoniadou (2016). Libert and Sansottera (2013) conducted simulations for the systems HD 108874 and HD 183263. The evolution of HD 155358 was discussed by André and Papaloizou (2016). HD 73526 was analyzed by Wittenmyer et al. (2014a).

HD 7449 has the highest eccentricities of the sample, but Rodigas et al. (2016) found that the second planet may be a sub-stellar companion, located at a greater distance than previous reports indicated.

One close and one wide system were analyzed to evaluate for the stability of quasi-satellite asteroids in two-planet systems. HD 73526 has moderate eccentricities, and is likely in the common 2:1 mean motion resonance. It was chosen as the system with planets which are in close proximity to one another. HD183263 was chosen to represent the systems with high semi-major axis ratio. The complete orbital elements with all published errors are summarized in Table 9. The mean anomalies in the HD 183263 system were derived using the perihelion dates given in the literature. A mean anomaly of 0° was assumed for planet b and the maximum error was computed from this. No values for the inclination are known for either system.

Planet	$m \sin i[M_\odot]$	a[AU]	e	$\omega[°]$	$M[°]$
HD183263 b	0.00350 ± 0.00029	1.510 ± 0.087	0.357 ± 0.09	233.5 ± 2.3	0
HD183263 c	0.00341 ± 0.00053	4.35 ± 0.28	0.239 ± 0.064	345 ± 12	16.5 ± 12.4
HD73526 b	0.00224 ± 0.00011	0.65 ± 0.01	0.265 ± 0.021	198.3 ± 3.6	105.5 ± 5.0
HD73526 c	0.00209 ± 0.00011	1.03 ± 0.02	0.198 ± 0.029	294.5 ± 11.3	153.4 ± 9.0

Table 9: Orbital elements with errors for the systems HD183263 and HD73526. The values for HD 183263 are taken from Wright et al. (2009). Values for HD73526 are taken from Wittenmyer et al. (2014a).

	a[AU]	e	$i[°]$	$\Omega[°]$	$\omega[°]$	$M[°]$	$m[M_\odot]$
Star	0	0	0	0	0	0	1.17
Planet b	1.51	0.357	0	233.5	0	0	0.0035
Planet c	4.35	0.239	1	345	0	16.5	0.00341
Asteroids b	1.51	$0.15, 0.6683 \pm 0.01$	0	53.5 ± 2	0	180	0
Asteroids c	4.35	$0.2, 0.7270 \pm 0.01$	0	165.0 ± 2	0	196.5	0

Table 10: Initial conditions for the simulations of the system HD 183263

3.4.1 HD 183263

The orbital elements reported by Wright et al. (2009) lead to a stable solution for at least 1 Myr for HD 183263, which made them suitable for further analysis. The system is close to the 5:1 mean motion resonance and may enter the resonance within the next 1 Myr depending on the exact initial conditions.

A statistical approach was chosen for determining the stability of quasi-satellites in this system. The two planets were numerically integrated with the orbital elements of Table 9. A small mutual inclination of 1° was used to enable non-coplanar effects. Massless quasi-satellites were placed in resonant orbits for both planets. Half were given initial conditions close to the anti-aligned fixed points. The location of the fixed point was calculated with the method described in section 2.2.2 (minimization of $\delta\varpi$, compare Equation 42). This resulted in $e_{a,t=0} = 0.6683$ for planet b's fixed point and $e_{a,t=0} = 0.7270$ for planet c's fixed point. $\Delta\varpi$ is 180° and $\Delta\lambda$ is 0° at this point. Massless objects were spread around the point using a normal distribution, which had a standard deviation of 0.01 in $e_{a,t=0}$ and 2° in $\omega_{a,t=0}$. The remaining half of the objects were placed in the precession region of the phase space at $e_{a,t=0} = 0.25$ for the inner planet and 0.2 for the outer planet (compare middle panels of Figure 15 at $\Delta\varpi = 180°$ and $\Delta\lambda = 0°$). These initial conditions are listed in Table 10. 200 librating and 200 precessing massless objects for each planet were simulated with an integration time 0f 100000 years.

The resonance lifetimes for the simulations are summarized in Table 11 and in Figure 37:

- It is readily apparent that the quasi-satellites of the inner planet b can remain stable for significantly longer periods than those of the outer planet c.
- Planet c's quasi-satellites are ejected from the resonance within 30 years in the case of the librating objects, and within 190 years in the case of the precessing objects.
- The librating quasi-satellites of planet c have an initial perihelion distance of under 1.2 AU, which is well within the orbital domain of planet b. The asteroids are closer to planet b than planet c for a significant share of their orbit, which quickly disturbs their resonance with planet c.
- The precessing objects of planet c initially have a perihelion distance of 3.5 AU, where planet c is still dominant. The evolution in phase space rapidly carries the objects to higher eccentricities (compare Figure 15), where the influence from planet b removes them from the resonance.
- The quasi-satellites of planet b are stable for longer periods of time. The aphelion distance of the librating test objects is just over 2.5 AU, which is well within of the perihelion of planet c (3.5 AU).
- 27 of the 200 test objects survived in the resonance for the whole integration time of 100000 years.
- The median lifetime of planet b's librating quasi-satellites was 56555 years, with most objects ranging 40000-70000 years. No object left the resonance within the first 22530 years.
- Precessing objects of planet b had shorter lifetimes, with a median resonance lifetime of just under 3000 years. The most stable precession object survived for 40420 years.
- The discrepancy between the two types of objects is due to the librating objects evolving in a small part of the phase space close to the fixed point, where they are not vulnerable to the influence of the other planet. The precessing objects evolve through a large part of the phase space and reach very high eccentricities, where they can be removed from the resonance.

The orbital evolution of one object in the HD183263 system, that had a resonance lifetime exceeding 100000 years, is depicted in Figure 38. The phase space evolution shows a chaotic libration around the quasi-satellite island. This island is considerably smaller than the island in the one-planet case (compare Figure 15). The resonance angle $\Delta\lambda$ undergoes short-term variation comparable to the situation of initially perturbed objects in the one-planet case (See Figure 21). The inclination of the initially coplanar object (with respect to planet b) reached 60°, even though the mutual inclination of the two planets is only 1°. The evolution of other objects was similar. They can be

	minimum RL [years]	median RL [years]	maximum RL [years]
Precessing objects			
Planet b	260	2785	40420
Planet c	80	90	190
Librating objects			
Planet b	22530	56555	100000
Planet c	20	20	30

Table 11: Resonance lifetimes (RL) for 200 quasi-satellites in the HD 183263 system with the initial conditions of Table 10

	a[AU]	e	$i[°]$	$\Omega[°]$	$\omega[°]$	$M[°]$	$m[M_\odot]$
Star	0	0	0	0	0	0	1.08
Planet b	0.65	0.265	0	198.3	0	105.0	0.00224
Planet c	1.03	0.198	1	294.5	0	154.3	0.00209
Asteroids b	0.65	$0.15, 0.7143 \pm 0.01$	0	18.3 ± 2	0	285	0
Asteroids c	1.03	$0.2, 0.7467 \pm 0.01$	0	114.5 ± 2	0	334.3	0

Table 12: Initial conditions for the simulations of the system HD 73526

removed from the resonance by the outer planet c, once they reach the outer part of the stable region .

3.4.2 HD 73526

The two planets in the HD 73526 system were first reported by Tinney et al. (2003) and Tinney et al. (2006). Their orbital parameters (see Table 8) came from a least-square Keplerian fit. Wittenmyer et al. (2014a) used a dynamical fit model whose parameters proved to be more dynamically stable than the original ones. The parameters for their $i = 90°$ model (summarized in Table 9) were used in the dynamical simulations in this work.

The same simulation setup as for HD 183263 was used for HD73526 (summarized in Table 12). The fixed points lie at $e_a = 0.7143$ for planet b and at $e_a = 0.7467$ for planet c. The objects in the precession region were placed at $e_{a,t=0} = 0.15$ for planet b and at $e_{a,t=0} = 0.2$ for planet c. The normal distribution was used to create a statistical spread in the parameters e_a and $\Delta\varpi$.

The results are summarized in Table 13 and Figure 39. The result is very similar to the HD 183263 system, although the two planets are closer together in HD 73526:

- On average, quasi-satellites of the outer planets did not survive in the resonance for more than 100 years, although there were single objects that survived longer than that. The maximum resonance lifetime was 230 years for librating objects and 2210 years for precessing objects.

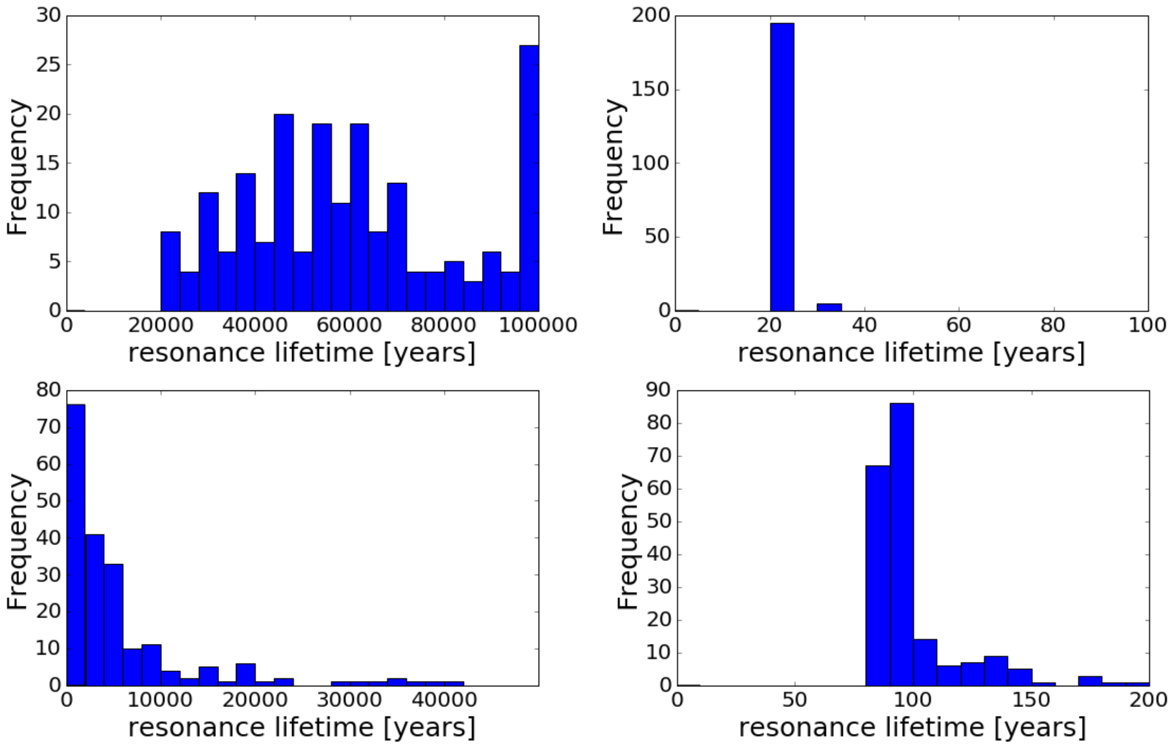

Figure 37: Histogram of the resonance lifetimes for the simulations of HD 183263 with the initial conditions of Table 10. Planet b is in the left panels with the librating objects in the top panel and the precessing objects in the bottom panel. Planet c is in the right panel with the same placements.

- The quasi-satellites of the inner planet again had longer resonance lifetimes. There were no objects surviving longer than 8000 years for HD 73526. The perihelion distance of planet c is approximately 0.82 AU, so coorbital objects of planet b only need to have an eccentricity of 0.26 to reach that distance at their aphelion. Close encounters may be avoided temporarily due to the 2:1-resonance between the planets, but eventually the objects are removed from the resonance. The median lifetime was 480 years for precessing objects and 985 years for librating objects.

4 Discussion and Conclusions

The previous chapters have shown that the dynamical configuration of quasi-satellites has a very rich and complex structure. The phase space can be investigated in detail by averaging the indirect part of the Hamiltonian function in a three-body system of a star, one planet, and one asteroid over one orbit. Different regions of the phase space characterise different types of coorbital resonance. The quasi-satellite island and its

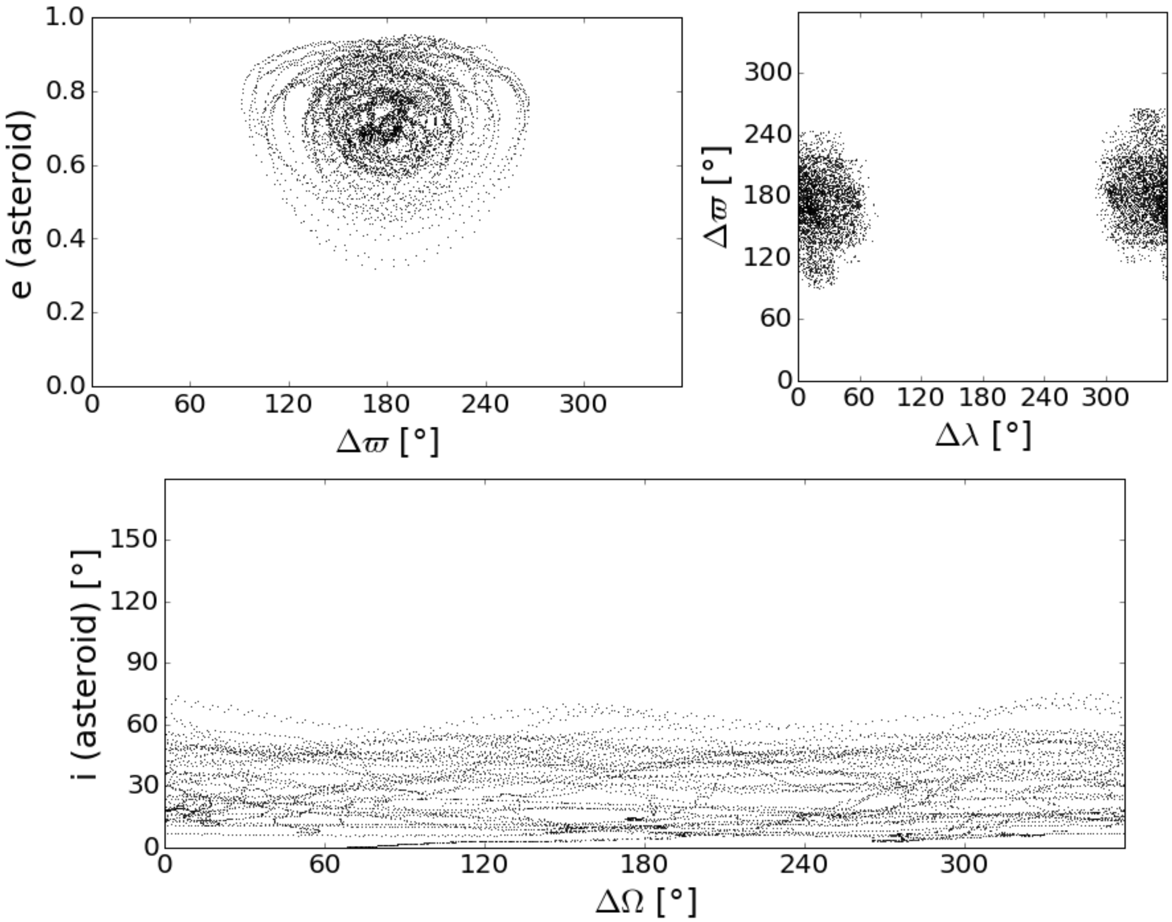

Figure 38: Example of the phase space evolution in $e_a - \Delta\varpi$ (upper left), $\Delta\varpi - \Delta\lambda$ (upper right), and $i_a - \Delta\Omega$ of one of the longest surviving quasi-satellites of HD 183263 b

	minimum RL [years]	median RL [years]	maximum RL [years]
Precessing objects			
Planet b	200	480	7240
Planet c	30	50	2210
Librating objects			
Planet b	20	985	6820
Planet c	40	60	230

Table 13: Resonance lifetimes (RL) for 200 quasi-satellites in the HD 73526 system with the initial conditions of Table 12

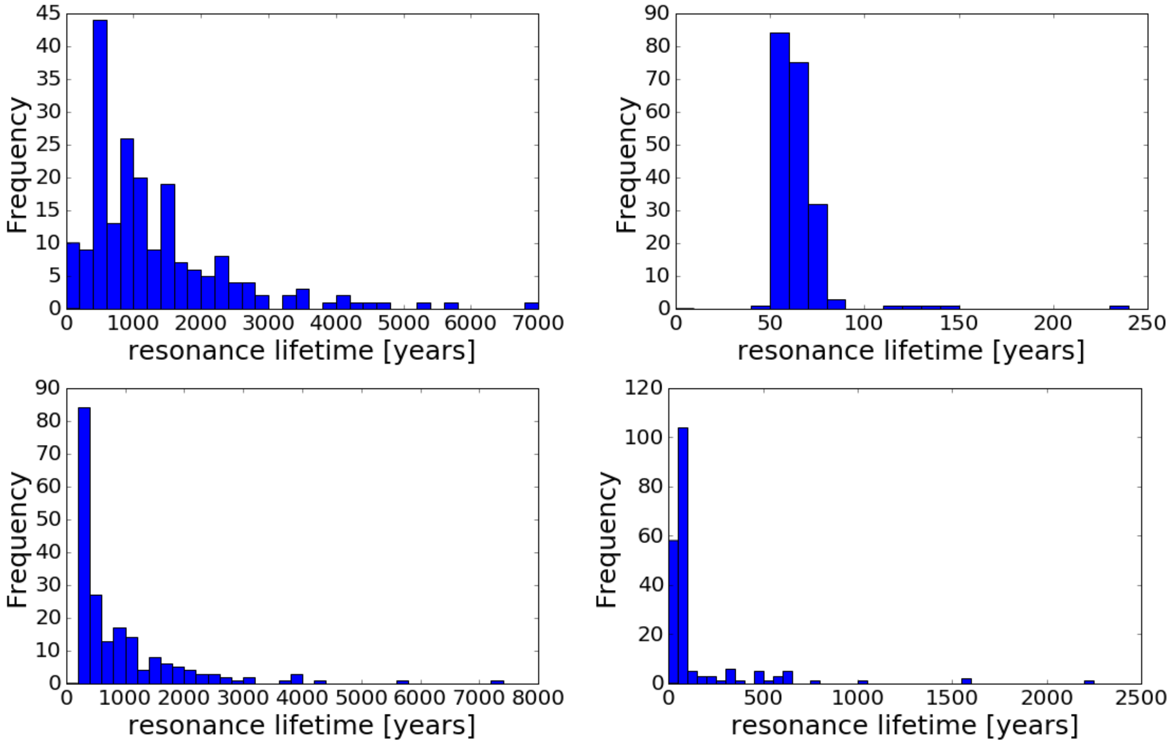

Figure 39: Histogram of the resonance lifetimes for the simulations of HD 73526 with the initial conditions of Table 12. Planet b is in the left panels with the librating objects in the top panel and the precessing objects in the bottom panel. Planet c is in the right panel with the same placements.

anti-aligned fixed point at $\Delta\varpi = 180°$ are stable phenomena occurring for all values of e_p. The island takes an increasing part of the phase space with increasing planetary eccentricity, whereas the Trojan islands shrink and near collision orbits. The anti-aligned fixed point moves from $e_a = 0.835$ at $e_p = 0$ down to $e_a = 0.48$ at $e_p = 0.83$ before increasing again for the highest eccentricities. The global maximum of the quasi-satellite island lies at $e_p = e_a = 0.565$, a value that was also found in other literature.

The semi-analytical model could potentially be expanded to three dimensions without changing the principal computation method. Two additional resonant canonical variables would need to be introduced, which would make the depiction and interpretation of the multidimensional phase space more challenging. This expansion is reserved for future work.

The numerical integrations with the Lie series integrator confirmed the existence and stability of the regions found in the semi-analytical model. Three families of stable quasi-satellite objects could be distinguished by their behavior in $\Delta\varpi$. $\Delta\varpi$ can librate around the anti-aligned fixed point, precess through all possible values, or librate around $0°$. Some objects enter a trajectory wherein their eccentricity approaches unity, which results in a collision with the star. These objects are most prevalent between $e_p = 0.2$

and $e_p = 0.5$. $\Delta\varpi$-precessing orbits are no longer possible for $e_p > 0.5$.

The oscillation times or secular times of quasi-satellites are very slow (over 10000 years) for the lowest planetary eccentricities and are within a stable range (2500-5000 years) for most other values. Interestingly, in the librating region, the minimal libration period is at the fixed point for some eccentricities and close to its border region for others. Precessing objects generally evolve faster than librating objects. There are various analytical approaches for determining secular frequencies in the 3BP, although most only work up to certain eccentricities. A comparison of these methods with the numerical results could provide more insight into the resonance structure.

A short-term $\Delta\lambda$ oscillation is added to the secular evolution, when the semi-major axis of a quasi-satellite asteroid is perturbed. The anti-aligned fixed point moves up to a higher eccentricity, and the stable region becomes smaller.

In comparison, the results of the semi-analytical model and the numerical integrations show very good agreement. The locations of the fixed points calculated with the two methods deviate from one another by less than 0.006 in terms of their eccentricity. The change of the averaged Hamiltonian function along a numerical trajectory is also very small. Some of the difference comes from high order effects neglected by the semi-analytical model, while others may be rooted in errors in the numerical integration. A more consistent use of barycentric coordinates could help to clarify this difference since the heliocentric data can add artifacts.

The dynamics become more chaotic in non-coplanar configurations, and closed trajectories can no longer be observed. The exact trajectory is dependent on the node difference $\Delta\Omega$. Depending on this variable, the quasi-satellite resonance island remains stable up to 70° or 100° at $e_p = 0.5$. The inclinations of quasi-satellites move in a wave pattern with maxima around $\Delta\Omega = 0°$ and 180°. A retrograde resonance with a different resonance angle can come into play at high inclination. The investigation of these regions at different planetary eccentricity is reserved for future work.

Relativistic effects play a role in quasi-satellite configurations if the eccentricity becomes high and the perihelion distance becomes low. They are responsible for a small precession in $\Delta\varpi$ at the semi-major axes considered in this work. The principal structure of the resonance does not change. This is expected to be different for smaller semi-major axes.

The computation of the Lyapunov Characteristic Exponents via the Hessian matrix is a useful method, with the significant advantage of being independent of the integrator used. The algorithm is still limited by its need to store large amounts of data and the long computation time required by the small time step. There is potential for optimization of the algorithm. A longer time step would be possible, if a numerical integration method more robust than the second-order Heun method were used. This work presents only a small sample of LCE computations for quasi-satellites, that show some unusual behavior. A systematic investigation is reserved for future work.

Quasi-satellites are a possibility for asteroid populations in extrasolar planet systems, especially for eccentric planets. Extensive numerical analysis needs to be performed to evaluate the stability of quasi-satellites in multi-planet systems. This work provides some results for the two-planet systems HD 183263 and HD 73526. In the HD 183262 system, the inner planet can keep quasi-satellites close to the anti-aligned fixed point stable for more than 100000 years. The outer planet rapidly ejects its quasi-satellites from the resonance. In the HD 73526 system, the quasi-satellites of both planets are at most stable for thousands of years. The resonance lifetimes in the real systems could differ significantly, since the mutual inclination and the exact planetary masses of these systems are unknown.

Generally, quasi-satellites can be expected in resonance with the inner planet of two-planet systems. Systems where the two planets are far apart from one another and systems with low planetary masses are also more likely to have a significant quasi-satellite asteroid population.

5 Acknowledgments

I want to express my gratitude to every person who made this master thesis possible and made its completion easier for me.

First of all, I thank my Professor Rudolf Dvorak for his competent and critical supervision, for his feedback and the freedom he gave me for his work. I would also like to express my gratitude to Dr. Christoph Lhotka for his help, especially with the semi-analytical models and his extensive critical comments on the manuscript. I also thank the rest of the astrodynamical group of the University of Vienna, especially Dr. Elke Pilat-Lohinger, Dr. Thomas Maindl, and Dr. Akos Bazso for spontaneous help with various problems and thought-provoking questions and discussions during talks and meetings.

Special thanks goes to Dr. Kevin Hinson for his great work on the revision of the manuscript, which especially improved its linguistic quality.

I am grateful as well to Dr. Siegfried Eggl for providing me the relativistic integrator and his helpful suggestions for its usage and to Professor Silvio Ferraz-Mello for an interesting discussion and some very helpful paper recommendations during a very early stage of this work.

I would also like to offer a special thanks to Igor Kraut for his companionship during our parallel master theses, his support especially with technical issues, and for our productive joint work on the Lyapunov exponents. I extend this gratitude to all my friends and colleagues at the Institute for Astronomy and Astrophysics at the University of Vienna, especially Andreas, Beatrice, Benedict, Bernhard, Bianca, Christopher, Cosima, Dominik, Fabian, Marianne, Maximilian, Nikolaus H., Nikolaus S., Philip, Roman, Santiago, and Victoria for being patient and listening to me whenever I needed somebody to talk.

Lastly, I would like to express my deepest appreciation to my mother and my father for enabling my education and providing financial support for my studies, and to my sisters Lisa and Vera for always being there when I needed them.

Appendices

A Computation of the Lyapunov Characteristic Exponents

The algorithm to compute the LCEs was implemented in the Python language. The packages "numpy" (abbreviated as "np" in the code) and "os" are required. The code is documented in two parts. The first part specifies the framework and the interaction with the integrator, and the second part deals with the computation of the LCEs.

The input file of the integrator (in this case named "super.in") needs to be provided by the user and is read in first. The total number of participating bodies, the mass of each body, the integration time, and the integration time step are extracted from the file and are saved by the program for later use. The total number of time steps is computed with this information. The indices pointing to these values depend on the format of the input file.

The number of iterations of the integrator n_{iter} is specified next by the user. It is recommended that a large value for n_{iter} is used for long integration times to minimize the amount of data for each individual integration. After $\vec{w}$ and the LCE vectors are initialized, the numerical integration is executed. The user needs to provide an executable file for this (named "a.exe" in the code). The output files (in this case named "coo.dat" and "ele.dat") are written into arrays after completion of the integration. The LCEs are then computed for every body in the system (explained in the next paragraph). When the computation is finished, the input and output files for the integration are archived and numbered consecutively. A new input file is written that uses the last entries of the integration as start values. The exact format is dependent on the format of the individual integrator. This procedure (beginning with the execution of the integration) is repeated, until n_{iter} is reached. The original input file would be named "super0.in" after this procedure.

```
def write_new_super(N,dt,t_total,data_ele,m):
  sup=open('super.in','x')
  sup.write(str(t_total)+'\t'+str(dt)+'\n')#integration time &time step
  sup.write('0\n')
  sup.write('12\n')
  sup.write(str(N)+'\t 0\n')
  sup.write('-11\n')
  sup.write('1E-11\n')
  sup.write('0 \t 0\n') #integrator specific constants
  sup.write('\n')
  sup.write('0 0 0 0 0 0 '+str(m[0])+'\n' ) #central body
  for i in range(1,N):
    sup.write(data_ele[-N+i][1]+' '+data_ele[-N+i][2]+
    ' '+data_ele[-N+i][3]+' '+data_ele[-N+i][4]+' '+
    data_ele[-N+i][5]+' '+data_ele[-N+i][6]+' '+str(m[i])+'\n')
     #orbital elements of every body at last time step
  sup.close()

def file_to_array(datafile):
  #reading text file into array
  if os.path.isfile(datafile):
     data = []
     with open(datafile) as file:
       for line in file:
```

```
            data.append([(f) for f in line.strip().split()])
        return data
    else:
        print ("error: file " + datafile + " was not found")

def get_mass(N,data):
    #read in masses
    m = np.zeros(N)
    for i in range(0,N):
        m[i] = data[8+i][6]
    return m

data_super = file_to_array("super.in") #file needs to be provided by user
N           = int(data_super[3][0]) + int(data_super[3][1])
m           = get_mass(N,data_super)
dt          = float(data_super[0][1].replace("d","e"))
t_total     = float(data_super[0][0].replace("d","e"))
num_data    = int(t_total/dt)
n_iter    =2                  # number of interations
w1        = np.zeros((6,N))
w1       += np.sqrt(1/6.0)    #initialization of unit vector
lce_pr    = np.zeros(N)       #initialization of LCE
for q in range(0,n_iter):
    os.system("C:/PathToProgram/a.exe")
    #execute integrator (compiled version), path needs to be specified
    data_coo    = file_to_array("coo.dat")
    data_ele    = file_to_array("ele.dat") #read in output files
    for p in range(1,N):
        #calculation of LCE for every body [code block next paragraphs]

    os.rename("C:/PathToProgram/super.in",
              "C:/PathToProgram/super"+str(q)+".in")
    os.rename("C:/PathToProgram/coo.dat",
              "C:/PathToProgram/coo"+str(q)+".dat")
    os.rename("C:/PathToProgram/ele.dat",
              "C:/PathToProgram/ele"+str(q)+".dat")
    #archiving input & output files (dependant on integrator)
    if q==n_iter-1:
        continue
    write_new_super(N,dt,t_total,data_ele,m)
    #generating input for next iteration
```

The LCE computation is executed for every body seperately. The local LCEs are computed for every time step by evolving the variational equations (Equation 48) with the Heun method (Equations 56 and 57). The J_{2N} matrix and the Hessian Matrix are calculated with the Equations 50 and 52-55. The values of α are stored in a vector, and $\vec{w}$ is renormalized after every time step. The LCE is then calculated according to equation 51. After the computation is concluded, the final LCE and the final unit vector $\vec{w}$ are stored for each body and used again in the next iteration. The LCEs are written into an individual text file for every body.

```
def get_x(N,data,t):
  #read in coordinates of every body (cartesian, heliocentric)
  # coordinates of first body equal to (0,0,0)
  x = np.zeros((N,3))
  for i in range(1,N):
    for j in range(0,3):
      x[i][j] = data[4+(N-1)*t+i-1][j+1]
  return x

def hesse_element (p,i,j,m,x,N):
  # p is index of body for which the derrivatives are formed
  # i and j are the indices for the matrix element
  # m is the vector of the masses of the bodies
  # x is the data matrix, that contains the coordinates for all bodies
  # N is the number of bodies
  G = 0.0002959122#gravitational constant (units: AU,days,solar_mass)
  if i>5 or j>5 or p>=N:
    print ("input error: i,j or p out of range!")
    value = "error"

  elif i==j and i>2:
    # diagonal element of velocity
    value = 1.0/m[p]

  elif i!=j and (i>2 or j>2):
    # nondiagonal velocity component + mixed terms
    value = 0

  elif i==j:
    # diagonal elements of spatial component
    value = 0.0
    for ii in range(0,N):
      if ii==p: continue
      denominator = ((x[ii][0]-x[p][0])**2+(x[ii][1]-x[p][1])**2 +
                     (x[ii][2]-x[p][2])**2)
```

```
        value       += G*m[p]*m[ii]*((-3*(x[ii][j]-x[p][j])**2)/
                       denominator**(5.0/2) + 1/denominator**(3.0/2))
  elif i!=j:
    # nondiagonal elements of spatial component
    value = 0.0
    for ii in range(0,N):
      if ii==p: continue
      denominator = ((x[ii][0]-x[p][0])**2+(x[ii][1]-x[p][1])**2 +
                     (x[ii][2]-x[p][2])**2)
      value       += G*m[p]*m[ii]*((-3*(x[ii][j]-x[p][j]) *
                     (x[ii][i]-x[p][i]))/denominator**(5.0/2))

  return value

def hessian_matrix(p,m,x,N):
  #generation of Hessian matrix
  hess = np.zeros((6,6))
  for i in range(0,6):
    for j in range(0,6):
      hess[i][j] = hesse_element(p,i,j,m,x,N)
  return hess

def J2D():
  #generation J2D matrix
  j2D = np.zeros((6,6))
  for i in range(0,6):
    for j in range(0,6):
      if (i-j)==3: j2D[i][j] = -1
      elif (j-i)==3: j2D[i][j] = 1
  return j2D

def heun(dt,w,M,M_next):
  #second order Heun method for integration
  w_dot = np.matmul(M,w)
  w_pred = w + dt*w_dot
  w_next = 0.5*w + 0.5*(w_pred + dt*np.matmul(M_next,w_pred))
  return w_next

def alpha(alph,w):
  #calculating local LCE and renormalizing w
  alpha = np.linalg.norm(w)
  alph.append(alpha)
  w_next = w/alpha
```

```
  return w_next

def lce_calc(lce_pr,alph,dt,t_total,q,lce):
  #Calculating LCE with alpha collection
  lna = lce_pr #value from previous iteration
  tau = q*t_total
  for i in range(0,len(alph)):
    lna += np.log(alph[i])
    tau += dt
    lce.append(lna/tau)
  return lna

def print_lce_to_file(f,lce_heun):
  #one file for each body
  for number in lce_heun:
    f.write(str(number)+'\n')
  return

for p in range(1,N):
    lce_heun      = []
    alph_heun     = []#initializing LCEs
    f=open('lce'+str(p)+'.dat','a')
    w_heun=w1[:,p]
    x = get_x(N,data_coo,0)
    H = hessian_matrix(p,m,x,N)
    J2D = J2D()
    M = np.matmul(J2D,H)

    for t in range(0,num_data-1):
      x_next = get_x(N,data_coo,t+1)       #data from output file
      H_next = hessian_matrix(p,m,x_next,N)
      M_next = np.matmul(J2D,H_next)
      w_heun  = heun(dt,w_heun,M,M_next)  #variaional equation
      w_heun  = alpha(alph_heun,w_heun)    #renormalization
     M = M_next
    w1[:,p]=w_heun
    lce_pr[p]=lce_calc(lce_pr[p],alph_heun,dt,t_total,q,lce_heun)
    #saving final LCE for use in next iteration
    print_lce_to_file(f,lce_heun)
    f.close()
```

References

André, Q. and J. C. B. Papaloizou (Oct. 2016). "On the orbital evolution of a pair of giant planets in mean motion resonance". In: *Monthly Notices of the Royal Astronomical Society* 461, pp. 4406–4418. arXiv: 1607.00628 [astro-ph.EP].

Antoniadou, K. I. (Sept. 2016). "Regular and chaotic orbits in the dynamics of exoplanets". In: *European Physical Journal Special Topics* 225. arXiv: 1604.04751 [astro-ph.EP].

Antoniadou, K. I. and G. Voyatzis (Oct. 2016). "Orbital stability of coplanar two-planet exosystems with high eccentricities". In: *Monthly Notices of the Royal Astronomical Society* 461, pp. 3822–3834. arXiv: 1606.07743 [astro-ph.EP].

Batygin, K. and A. Morbidelli (Oct. 2017). "Dynamical Evolution Induced by Planet Nine". In: *ArXiv e-prints*. arXiv: 1710.01804 [astro-ph.EP].

Brasser, R. et al. (Sept. 2004). "Transient co-orbital asteroids". In: *Icarus* 171, pp. 102–109.

Butler, R. P. et al. (Jan. 2003). "Seven New Keck Planets Orbiting G and K Dwarfs". In: *The Astrophysical Journal* 582, pp. 455–466.

Center, Minor Planet. *Lists and Plots: Minor Planets.* URL: https://www.minorplanetcenter.net/iau/lists/MPLists.html (visited on 04/16/2018).

Cochran, W. D., M. Endl, and R. A. Wittenmyer (Oct. 2007). "New Extra-Solar Planets from the Texas Planet Search". In: *AAS/Division for Planetary Sciences Meeting Abstracts #39*. Vol. 39. Bulletin of the American Astronomical Society, p. 466.

Connors, M. (Jan. 2014). "A Kozai-resonating Earth quasi-satellite". In: *Monthly Notices of the Royal Astronomical Society* 437, pp. L85–L89.

Connors, M., P. Wiegert, and C. Veillet (July 2011). "Earth's Trojan asteroid". In: *Nature* 475, pp. 481–483.

Connors, M. et al. (Oct. 2002). "Discovery of an asteroid and quasi-satellite in an Earth-like horseshoe orbit". In: *Meteoritics and Planetary Science* 37, pp. 1435–1441.

Connors, M. et al. (Aug. 2004). "Discovery of Earth's quasi-satellite". In: *Meteoritics and Planetary Science* 39, pp. 1251–1255.

de la Fuente Marcos, C. and R. de la Fuente Marcos (Sept. 2012). "(309239) 2007 RW_{10}: a large temporary quasi-satellite of Neptune". In: *Astronomy & Astrophysics* 545, L9, p. L9. arXiv: 1209.1577 [astro-ph.EP].

— (June 2013). "Asteroid 2012 XE_{133}: a transient companion to Venus". In: *Monthly Notices of the Royal Astronomical Society* 432, pp. 886–893. arXiv: 1303.3705 [astro-ph.EP].

— (Apr. 2014a). "Asteroid 2013 ND_{15}: Trojan companion to Venus, PHA to the Earth". In: *Monthly Notices of the Royal Astronomical Society* 439, pp. 2970–2977. arXiv: 1401.5013 [astro-ph.EP].

— (Dec. 2014b). "Asteroid 2014 OL_{339}: yet another Earth quasi-satellite". In: *Monthly Notices of the Royal Astronomical Society* 445, pp. 2985–2994. arXiv: 1409.5588 [astro-ph.EP].

de la Fuente Marcos, C. and R. de la Fuente Marcos (Nov. 2016a). "Asteroid (469219) 2016 HO_3, the smallest and closest Earth quasi-satellite". In: *Monthly Notices of the Royal Astronomical Society* 462, pp. 3441–3456. arXiv: `1608.01518 [astro-ph.EP]`.

— (Jan. 2016b). "From horseshoe to quasi-satellite and back again: the curious dynamics of Earth co-orbital asteroid 2015 SO_2". In: *Astrophysics and Space Science* 361, 16, p. 16. arXiv: `1511.08360 [astro-ph.EP]`.

— (Dec. 2017). "Transient Co-orbitals of Venus: An Update". In: *Research Notes of the American Astronomical Society* 1, 3, p. 3. arXiv: `1711.00453 [astro-ph.EP]`.

de Medeiros, J. R. et al. (Sept. 2009). "A planet around the evolved intermediate-mass star HD 110014". In: *Astronomy & Astrophysics* 504, pp. 617–623.

Delaunay, M. (Jan. 1861). "Théorie du Mouvement de la Lune". In: *Monthly Notices of the Royal Astronomical Society* 21, p. 80.

Dumusque, X. et al. (Nov. 2011). "The HARPS search for southern extra-solar planets. XXX. Planetary systems around stars with solar-like magnetic cycles and short-term activity variation". In: *Astronomy & Astrophysics* 535, A55, A55. arXiv: `1107.1748 [astro-ph.EP]`.

Dvorak, R. and F. Freistetter (2005). "Orbit Dynamics, Stability and Chaos in Planetary Systems". In: *Chaos and Stability in Planetary Systems*. Ed. by R. Dvorak, F. Freistetter, and J. Kurths. Vol. 683. Lecture Notes in Physics, Berlin Springer Verlag, pp. 3–140.

Dvorak, R., C. Lhotka, and L. Zhou (May 2012). "The orbit of 2010 TK7: possible regions of stability for other Earth Trojan asteroids". In: *Astronomy & Astrophysics* 541, A127, A127. arXiv: `1202.1086 [astro-ph.EP]`.

Eggl, S. and R. Dvorak (Mar. 2010). "An Introduction to Common Numerical Integration Codes Used in Dynamical Astronomy". In: *Lecture Notes in Physics, Berlin Springer Verlag*. Ed. by J. Souchay and R. Dvorak. Vol. 790. Lecture Notes in Physics, Berlin Springer Verlag, pp. 431–480.

Funk, B., R. Dvorak, and R. Schwarz (Aug. 2017). "Exchange orbits - an interesting case of co-orbital motion". In: *ArXiv e-prints*. arXiv: `1708.04205 [astro-ph.EP]`.

Funk, B. et al. (Jan. 2011). "Exchange orbits: a possible application to extrasolar planetary systems?" In: *Monthly Notices of the Royal Astronomical society* 410, pp. 455–460.

Gallardo, T. (Sept. 2006). "Atlas of the mean motion resonances in the Solar System". In: *Icarus* 184, pp. 29–38.

Giuppone, C. A., P. Benítez-Llambay, and C. Beaugé (Mar. 2012). "Origin and detectability of co-orbital planets from radial velocity data". In: *Monthly Notices of the Royal Astronomical Society* 421, pp. 356–368. arXiv: `1112.0223 [astro-ph.EP]`.

Giuppone, C. A. et al. (Sept. 2010). "Dynamics of two planets in co-orbital motion". In: *Monthly Notices of the Royal Astronomical Society* 407, pp. 390–398. arXiv: `1004.0726 [astro-ph.EP]`.

Hanslmeier, A. and R. Dvorak (Mar. 1984). "Numerical Integration with Lie Series". In: *Astronomy & Astrophysics* 132, p. 203.

Henon, M. (Feb. 1969). “Numerical exploration of the restricted problem, V”. In: *Astronomy & Astrophysics* 1, pp. 223–238.

Horner, J., F. E. Koch, and P. Sofia Lykawka (Feb. 2013). “Capturing Trojans and Irregular Satellites - the key required to unlock planetary migration”. In: *ArXiv e-prints*. arXiv: 1302.2304 [astro-ph.EP].

Howard, A. W. et al. (Mar. 2011). “The NASA-UC Eta-Earth Program. III. A Super-Earth Orbiting HD 97658 and a Neptune-mass Planet Orbiting Gl 785”. In: *The Astrophysical Journal* 730, 10, p. 10. arXiv: 1011.0414 [astro-ph.EP].

Jackson, J. (Dec. 1913). “Retrograde satellite orbits”. In: *Monthly Notices of the Royal Astronomical Society* 74, pp. 62–82.

Jenkins, J. S. et al. (Apr. 2017). “New planetary systems from the Calan-Hertfordshire Extrasolar Planet Search”. In: *Montly Notices of the Royal Astronomical Society* 466, pp. 443–473. arXiv: 1603.09391 [astro-ph.EP].

Kinoshita, H. and H. Nakai (July 2007). “Quasi-satellites of Jupiter”. In: *Celestial Mechanics and Dynamical Astronomy* 98, pp. 181–189.

Kortenkamp, S. J. (June 2005). “An efficient, low-velocity, resonant mechanism for capture of satellites by a protoplanet”. In: *Icarus* 175, pp. 409–418.

Kortenkamp, S. J. and E. C. S. Joseph (Oct. 2011). “Transformation of Trojans into quasi-satellites during planetary migration and their subsequent close-encounters with the host planet”. In: *Icarus* 215, pp. 669–681. arXiv: 1102.2211 [astro-ph.EP].

Kraut, I. (2018). “The Trojan twin Problem”. MA thesis. University of Vienna.

Laskar, J. and P. Robutel (July 1995). “Stability of the Planetary Three-Body Problem. I. Expansion of the Planetary Hamiltonian”. In: *Celestial Mechanics and Dynamical Astronomy* 62, pp. 193–217.

Leleu, A., P. Robutel, and A. C. M. Correia (Sept. 2015). “Detectability of quasi-circular co-orbital planets. Application to the radial velocity technique”. In: *Astronomy & Astrophysics* 581, A128, A128. arXiv: 1509.02276 [astro-ph.EP].

Lhotka, C. and A. Celletti (Apr. 2015). “The effect of Poynting-Robertson drag on the triangular Lagrangian points”. In: *Icarus* 250, pp. 249–261. arXiv: 1412.1630 [astro-ph.EP].

Libert, A.-S. and M. Sansottera (Oct. 2013). “On the extension of the Laplace-Lagrange secular theory to order two in the masses for extrasolar systems”. In: *Celestial Mechanics and Dynamical Astronomy* 117, pp. 149–168. arXiv: 1306.5624 [math-ph].

Lykawka, P. S. and J. Horner (June 2010). “The capture of Trojan asteroids by the giant planets during planetary migration”. In: *Monthly Notices of the Royal Astronomical Society* 405, pp. 1375–1383. arXiv: 1003.2137 [astro-ph.EP].

Marzari, F. and H. Scholl (Sept. 2007). “Dynamics of Jupiter Trojans during the 2:1 mean motion resonance crossing of Jupiter and Saturn”. In: *Monthly Notices of the Royal Astronomical Society* 380, pp. 479–488. arXiv: 0707.0617.

McCarthy, C. et al. (Dec. 2004). “Multiple Companions to HD 154857 and HD 160691”. In: *The Astrophysical Journal* 617, pp. 575–579. eprint: astro-ph/0409335.

Mikkola, S. and K. Innanen (1997). "Orbital Stability of Planetary Quasi-Satellites". In: *The Dynamical Behaviour of our Planetary System*. Ed. by R. Dvorak and J. Henrard, p. 345.

Mikkola, S. et al. (July 2004). "Asteroid 2002 VE68, a quasi-satellite of Venus". In: *Monthly Notices of the Royal Astronomical Society* 351, pp. L63–L65.

Morais, M. H. M. and F. Namouni (Dec. 2013). "Retrograde resonance in the planar three-body problem". In: *Celestial Mechanics and Dynamical Astronomy* 117, pp. 405–421. arXiv: `1305.0016 [astro-ph.EP]`.

— (May 2016). "A numerical investigation of coorbital stability and libration in three dimensions". In: *Celestial Mechanics and Dynamical Astronomy* 125, pp. 91–106. arXiv: `1602.04755 [astro-ph.EP]`.

Morbidelli, A. et al. (May 2005). "Chaotic capture of Jupiter's Trojan asteroids in the early Solar System". In: *Nature* 435, pp. 462–465.

Moutou, C. et al. (Mar. 2011). "The HARPS search for southern extra-solar planets. XXVII. Seven new planetary systems". In: *Astronomy & Astrophysics* 527, A63, A63. arXiv: `1012.3830 [astro-ph.EP]`.

Murray, C. D. and S. F. Dermott (1999). *Solar system dynamics*.

Namouni, F., A. A. Christou, and C. D. Murray (Apr. 1999). "New coorbital dynamics in the solar system". In: *ArXiv Astrophysics e-prints*. eprint: `astro-ph/9904016`.

Nesvorný, D. et al. (Apr. 2002). "A Perturbative Treatment of The Co-Orbital Motion". In: *Celestial Mechanics and Dynamical Astronomy* 82, pp. 323–361.

Niedzielski, A. et al. (Mar. 2009). "A Planet in a 0.6 AU Orbit Around the K0 Giant HD 102272". In: *The Astrophysical Journal* 693, pp. 276–280. arXiv: `0810.1710`.

Niedzielski, A. et al. (Jan. 2015). "Tracking Advanced Planetary Systems (TAPAS) with HARPS-N . I. A multiple planetary system around the red giant star TYC 1422-614-1". In: *Astronomy & Astrophysics* 573, A36, A36. arXiv: `1410.5971 [astro-ph.EP]`.

Pepe, F. et al. (Oct. 2011). "The HARPS search for Earth-like planets in the habitable zone. I. Very low-mass planets around HD 20794, HD 85512, and HD 192310". In: *Astronomy & Astrophysics* 534, A58, A58. arXiv: `1108.3447 [astro-ph.EP]`.

Poincaré, H. (1902). "Revue des publications astronomiques. Sur les planètes du type d'hécube". In: *Bulletin Astronomique, Serie I* 19, pp. 289–310.

Rodigas, T. J. et al. (Feb. 2016). "MagAO Imaging of Long-period Objects (MILO). I. A Benchmark M Dwarf Companion Exciting a Massive Planet around the Sun-like Star HD 7449". In: *The Astrophysical Journal* 818, 106, p. 106. arXiv: `1512.04540 [astro-ph.EP]`.

Sato, B. et al. (Jan. 2013). "A Double Planetary System around the Evolved Intermediate-mass Star HD 4732". In: *The Astrophysical Journal* 762, 9, p. 9. arXiv: `1210.6798 [astro-ph.EP]`.

Sato, B. et al. (Mar. 2016). "A Pair of Giant Planets around the Evolved Intermediate-mass Star HD 47366: Multiple Circular Orbits or a Mutually Retrograde Configuration". In: *The Astrophysical Journal* 819, 59, p. 59. arXiv: `1601.04417 [astro-ph.EP]`.

Schubart, J. (Apr. 1964). "Long-Period Effects in Nearly Commensurable Cases of the Restricted Three-Body Problem". In: *SAO Special Report* 149.

Schwarz, R. and R. Dvorak (May 2012). "Trojan capture by terrestrial planets". In: *Celestial Mechanics and Dynamical Astronomy* 113, pp. 23–34.

Schwarz, R. et al. (June 2009). "Stability of Trojan planets in multi-planetary systems. Stability of Trojan planets in different dynamical systems". In: *Celestial Mechanics and Dynamical Astronomy* 104, pp. 69–84.

Sidorenko, V. V. et al. (Oct. 2014). "Quasi-satellite orbits in the general context of dynamics in the 1:1 mean motion resonance: perturbative treatment". In: *Celestial Mechanics and Dynamical Astronomy* 120, pp. 131–162. arXiv: `1409.0417 [astro-ph.EP]`.

Skokos, C. (Mar. 2010). "The Lyapunov Characteristic Exponents and Their Computation". In: *Lecture Notes in Physics, Berlin Springer Verlag*. Ed. by J. Souchay and R. Dvorak. Vol. 790. Lecture Notes in Physics, Berlin Springer Verlag, pp. 63–135. DOI: `10.1007/978-3-642-04458-82`. arXiv: `0811.0882 [nlin.CD]`.

Soto, M. G., J. S. Jenkins, and M. I. Jones (Sept. 2015). "RAFT I: Discovery of New Planetary Candidates and Updated Orbits from Archival FEROS Spectra". In: *The Messenger* 161, pp. 24–27.

Teske, J. K. et al. (Dec. 2016). "The Magellan PFS Planet Search Program: Radial Velocity and Stellar Abundance Analyses of the 360 au, Metal-poor Binary Twins HD 133131A B". In: *The* 152, 167, p. 167. arXiv: `1608.06216 [astro-ph.EP]`.

Tinney, C. G. et al. (Apr. 2003). "Four New Planets Orbiting Metal-enriched Stars". In: *The Astrophysical Journal* 587, pp. 423–428. eprint: `astro-ph/0207128`.

Tinney, C. G. et al. (Aug. 2006). "The 2:1 Resonant Exoplanetary System Orbiting HD 73526". In: *The Astrophysical Journal* 647, pp. 594–599. eprint: `astro-ph/0602557`.

Tsiganis, K. et al. (May 2005). "Origin of the orbital architecture of the giant planets of the Solar System". In: *Nature* 435, pp. 459–461.

Vogt, S. S. et al. (Oct. 2005). "Five New Multicomponent Planetary Systems". In: *The Astrophysical Journal* 632, pp. 638–658.

Wajer, P. (Oct. 2010). "Dynamical evolution of Earths quasi-satellites: 2004 GU_9 and 2006 FV_{35}". In: *Icarus* 209, pp. 488–493.

Wajer, P. and M. Królikowska (Mar. 2012). "Behavior of Jupiter Non-Trojan Co-Orbitals". In: *Acta Astronomica* 62, pp. 113–131. arXiv: `1206.0557 [astro-ph.EP]`.

Wiegert, P., K. Innanen, and S. Mikkola (Apr. 2000). "The Stability of Quasi Satellites in the Outer Solar System". In: *The Astronomical Journal* 119, pp. 1978–1984.

Wiegert, P. et al. (Dec. 2002). "Earth Co-orbital Objects". In: *AGU Fall Meeting Abstracts*, P11A-0352, P11A–0352.

Wiegert, P. A., K. A. Innanen, and S. Mikkola (June 1997). "An asteroidal companion to the Earth". In: *Nature* 387, pp. 685–686.

— (June 1998). "The Orbital Evolution of Near-Earth Asteroid 3753". In: *The Astronomical Journal* 115, pp. 2604–2613.

Wittenmyer, R. A. et al. (Jan. 2014a). "A Detailed Analysis of the HD 73526 2:1 Resonant Planetary System". In: *The Astrophysical Journal* 780, 140, p. 140. arXiv: `1311.6559 [astro-ph.EP]`.

Wittenmyer, R. A. et al. (Mar. 2014b). “The Anglo-Australian Planet Search. XXIII. Two New Jupiter Analogs”. In: *The Astrophysical Journal* 783, 103, p. 103. arXiv: 1401.5525 [astro-ph.EP].

Wittenmyer, R. A. et al. (Feb. 2016). “The Pan-Pacific Planet Search. IV. Two Super-Jupiters in a 3:5 Resonance Orbiting the Giant Star HD 33844”. In: *The Astrophysical Journal* 818, 35, p. 35. arXiv: 1512.07316 [astro-ph.EP].

Wittenmyer, R. A. et al. (Apr. 2017). “The Anglo-Australian Planet Search. XXV. A Candidate Massive Saturn Analog Orbiting HD 30177”. In: *The Astronomical Journal* 153, 167, p. 167. arXiv: 1612.02072 [astro-ph.EP].

Wright, J. T. et al. (Mar. 2009). “Ten New and Updated Multiplanet Systems and a Survey of Exoplanetary Systems”. In: *The Astrophysical Journal* 693, pp. 1084–1099. arXiv: 0812.1582.

Zusammenfassung

Die 1:1-Resonanz gehört zu den bekanntesten Problemen der Himmelsmechanik. Sie tritt auf, wenn zwei Körper einen massiven Zentralkörper im selben Abstand umrunden. Jede dieser Resonanzen ist durch einen Resonanzwinkel charakterisiert, eine aus den Bahnelementen zusammengesetzte Größe, die während der Entwicklung der Umlaufbahn um einen bestimmten Wert oszilliert. Quasi-Satelliten stellen einen Spezialfall der 1:1-Resonanz im elliptischen. eingeschränkten Dreikörperproblem dar. Ihr Resonanzwinkel $\Delta\lambda$ oszilliert um den Wert 0°. Das wichtigste Ziel dieser Arbeit ist eine genaue Beschreibung des Phasenraums von Quasi-Satelliten im eingeschränkten Dreikörperproblem und eine Analyse der dynamischen Stabilität der Quasi-Satelliten in dieser Konfiguration.

Hierzu wurde ein semi-analytisches Modell aus dem Hamilton-Formalismus entwickelt, aus dem die grundlegende Struktur des Phasenraums abgeleitet werden konnte. Das Modell belegte bereits die Existenz eines Fixpunkts in einer Konfiguration mit entgegengesetzt ausgerichteten Perihellängen ($\Delta\varpi = 180°$). Im Gegensatz zu den bekannten Trojaner-Fixpunkten ($\Delta\lambda = 60, 300°$) wurde die Region um diesen Fixpunkt bei ansteigender Exzentrizität des Planeten stabiler und nahm einen großen Teil des Phasenraums ein. Dieses Ergebnis wurde auch durch numerische Integration bestätigt. Es zeigte sich, dass Quasi-Satelliten auf langen Zeitskalen auf einer resonanten Umlaufbahn verblieben. Sie besaßen sekuläre Perioden, die sich bei jupiterähnlichen Planeten meist zwischen 2500 und 5000 Jahren befanden. Es zeigte sich ebenfalls, dass die Konfiguration stabil blieb, wenn die große Halbachse des Asteroiden gestört wurde. Beim Vergleich der semianalytischen und numerischen Modelle zeigte sich eine gute Übereinstimmung. Der nicht-koplanare Fall wurde ebenfalls numerisch untersucht und es stellte sich heraus, dass chaotische Effekte eine größere Rolle spielten und die Resonanz für Inklinationen bis zu 100° stabil bleiben konnte. Mit anderen Anfangsbedingungen konnte auch eine retrograde Resonanz mit anderem Resonanzwinkel erzeugt werden. Bei Berücksichtigung von Effekten der Allgemeinen Relativitätstheorie zeigte sich nur eine geringe Abweichung der Ergebnisse. Die Beschreibung durch den

bekannten Chaos-Indikator Lyapunov-Exponent wurde mit einer Methode durchgeführt, die eine vom Integrationsverfahren unabhängige Berechnung ermöglichte.

Im Sonnensystem wurden bisher insgesamt 13 Quasi-Satelliten entdeckt, die für begrenzte Zeitskalen in ihrer Resonanz stabil sind. Unter den bisher entdeckten extrasolaren Planetensystemen gibt es ebenfalls Systeme, in denen Quasi-Satelliten stabil sein könnten. Dies ist besonders für Mehrplanetensysteme mit hohen Exzentrizitäten interessant. Um die Stabilität von Quasi-Satelliten in solchen Systemen numerisch zu überprüfen, wurden die beiden Systeme HD 183263 und HD 73526 ausgewählt. In beiden Fällen überdauerten Objekte in 1:1-Resonanz mit dem inneren Planeten länger in der Resonanz. Im Fall von HD 183263 überschritt diese Lebensdauer in einigen Fällen 100000 Jahre.